Differential Diffusion in a Turbulent Jet

by

Thomas Michael Lavertu

Thesis submitted to McGill University
in partial fulfilment of the requirements for the degree of
Doctor of Philosophy

Department of Mechanical Engineering
McGill University
Montréal, Canada.

Library and
Archives Canada

Bibliothèque et
Archives Canada

Published Heritage
Branch

Direction du
Patrimoine de l'édition

395 Wellington Street
Ottawa ON K1A 0N4
Canada

395, rue Wellington
Ottawa ON K1A 0N4
Canada

Canada

Abstract

Differential diffusion in a turbulent jet was investigated experimentally. The two primary objectives associated with this work were to systematically study: i) the Reynolds number dependence, and ii) the radial distribution of differential diffusion in the jet. These goals were simultaneously achieved, along with several secondary objectives, such as determining the scales at which differential diffusion is manifested and examining the effect of background turbulence on differential diffusion.

Experiments were performed in a momentum-driven, axisymmetric turbulent water jet, containing two passive scalars (fluorescent dyes) with differing molecular diffusivities (D). The jet issued into either a quiescent background or an approximately homogeneous, isotropic turbulent background. To determine the Reynolds number dependence, tests were conducted at five jet Reynolds numbers, ranging from Re = 900 to Re = 10600. (Re = $u_0 d/v$, where u_0 is the jet exit velocity, d is the jet exit diameter, and v is the kinematic viscosity.)

Laser-induced fluorescence (LIF) was employed to obtain instantaneous individual species concentrations at a downstream location, located in the self-similar region. At each Reynolds number, measurements were acquired at radial positions extending from the jet centreline to its edges. The normalized concentration difference, Z, was defined to elucidate differential diffusion effects. Statistics of this parameter revealed the magnitude of differential diffusion at each Reynolds number and radial location. In particular, the root-mean square of the normalized concentration difference, Z_{rms}, gave an indication of the intensity of these effects.

Centreline results showed that differential diffusion effects slowly decay with increasing Reynolds number, scaling as $Z_{rms} \propto \text{Re}^{-0.09}$. Even though the effects were decreasing, they were still non-zero at the highest Reynolds number

studied (Z_{rms} = 0.064 at the centreline at Re = 10600). Differential diffusion effects were also shown to increase i) with increased radial position from the centreline, and ii) in the presence of a turbulent background. These two instances, along with the increased differential diffusion at lower Reynolds numbers, support the hypothesis of an increase of differential diffusion effects as the occurrences of interfaces between dyed jet fluid and entrained ambient fluid increases.

Also presented are the first experimental measurements of the spectrum of the normalized concentration difference, $E_Z(\kappa_l\eta)$. These revealed the scales at which differential diffusion manifests itself. In all instances, these spectra were observed to decrease with wavenumber over all wavenumbers, consistent with a flow dominated by the decay of its scalar field. Although differential diffusion effects are molecular in origin, they persist at scales larger than the Kolmogorov scale.

Sommaire

Une étude expérimentale de la diffusion différentielle en jet turbulent est présentée dans cette thèse. Les objectifs principaux de celle-ci sont l'étude systématique de l'effet i) du nombre de Reynolds, et ii) de la position radiale dans l'écoulement sur la diffusion différentielle. Ces buts ont été réalisés simultanément avec plusieurs objectifs secondaires, y compris une analyse des échelles turbulentes atteintes par la diffusion différentielle et une étude de l'effet d'un milieu turbulent sur la diffusion différentielle.

Les mesures se sont faites en jet turbulent axisymétrique d'eau contenant deux scalaires passifs (teintures fluorescentes) de diffusivités moléculaires différentes. L'effet du nombre de Reynolds a été établi par l'étude du jet à cinq nombres de Reynolds (Re = $u_0 d/v$, où u_0 est la vitesse de l'eau à la sortie du jet, d est le diamètre du jet, et v est la viscosité cinématique de l'eau), s'étendant de Re = 900 à Re = 10 600.

Les concentrations instantanées des deux teintures ont été quantifiées (à chaque nombre de Reynolds) dans une section transversale du jet (dans la région autosemblable) par moyen de fluorescence induite au laser. La différence des concentrations normalisées (Z) a servi à établir l'ampleur de la diffusion différentielle à chaque nombre de Reynolds et à chaque position radiale. L'écart type de la différence des concentrations normalisées (Z_{rms}) servait à quantifier l'intensité de la diffusion différentielle.

L'intensité de la diffusion différentielle décroissait en augmentant le nombre de Reynolds ($Z_{rms} \propto Re^{-0.09}$ sur l'axe du jet). Cependant, la diffusion différentielle restait importante même au plus grand nombre de Reynolds (Z_{rms} = 0.064 sur l'axe du jet pour Re = 10 600). Les effets de la diffusion différentielle se sont aussi intensifiés i) en s'éloignant de l'axe du jet, et ii) quand le jet émanait en milieu turbulent. Ces deux observations, ainsi que l'intensification de la

diffusion différentielle en diminuant le nombre de Reynolds, soutiennent l'hypothèse d'une augmentation de la diffusion différentielle aux interfaces entre le fluide provenant du jet et le fluide ambiant (sans teinture).

Cette thèse présente aussi les premières mesures du spectre de la différence des concentrations normalisées, $E_Z(\kappa_1\eta)$. Celles-ci ont fait connaître les échelles sur laquelle la diffusion différentielle agissait. Tous les spectres – indépendamment du nombre de Reynolds, position radiale, ou le milieu ambiant – montraient une pente négative, en accord avec un champ scalaire décroissant. Bien que la diffusion différentielle prenne naissance aux petites échelles, ses effets ont été observés aux échelles plus grandes que l'échelle de Kolmogorov.

Acknowledgements

The completion of the research presented herein would not have been possible without the tremendous support I have received. Firstly, I would like to express gratitude towards my co-supervisors, Prof. Laurent Mydlarski and Prof. Susan Gaskin. Their expertise and enthusiasm has inspired me throughout this endeavour. They have provided outstanding guidance over the last few years that was instrumental in my development.

I would also like to acknowledge the funding provided by the Natural Sciences and Engineering Research Council of Canada and the Fonds québécois de la recherche sur la nature et les technologies.

Several members of the technical staff have graciously assisted in the design and construction of various components. I would first like to thank John Bartczak for his suggestions and assistance during the construction of the experimental apparatus. Damon Kiperchuck was helpful in machining numerous parts which were used in the construction of the experimental equipment. The advice provided by Georges Tewfik on the design and selection of electronic components was greatly appreciated.

My experience at McGill was greatly enhanced by the quality of the students I have been privileged to work alongside. Wolfram Pohl deserves much credit for his assistance in the initial development of the experimental apparatus. The many conversations I had with Etienne Costa-Patry certainly advanced my understanding of turbulence and often provided a much needed break in the day. Special thanks to Adam Wahab for constructing the random jet array and going well beyond what was expected to always lend a helping hand. I would also like to thank Katelin English and Babak Khorsandi for their aid in obtaining velocity measurements in the turbulent background. Adam Wahab, Alexandra Rhéaume and Jason Lepore also graciously took the time to help edit this thesis.

Finally, I want to thank my family, my brother and parents, for their support during the past few years. My brother was always there to offer suggestions, both during his time at McGill and since his graduation. I have received incredible support from my parents during these last few years and also beforehand. Their encouragement and direction have always led me in a positive direction and they have played a vital role in my accomplishments.

Table of Contents

List of Figures

List of Tables

Nomenclature

A, B, G, H I, J, K, L N, P	constants pertaining to the calibration curve fits
b	path length of a cell
C	species concentration
C_A	concentration of species A
C_B	concentration of species B
C_{Bl}	constant in empirical correlation of Batchelor scale
C_α	concentration of species α
C^*	non-dimensional scalar concentration
C_j	capacitance
C_0	jet nozzle scalar concentration
C_1	concentration of disodium fluorescein
C_2	concentration of sulforhodamine 101
c	concentration fluctuation
c_l	speed of light
c_{rms}	root-mean square of concentration fluctuations
$c_{rms,meas}$	measured root-mean square concentration fluctuations
$c_{1,rms}$	root-mean square concentration fluctuations of disodium fluorescein
$c_{2,rms}$	root-mean square concentration fluctuations of sulforhodamine 101
D	molecular diffusivity
$D_j(x)$	local jet diameter
D_b	beam diameter entering focusing lens
D_α	molecular diffusivity of species α
d	jet nozzle diameter
d_0	focused spot size
E	light energy absorbed by a molecule
$Ec_1(f)$	one-dimensional spectrum of disodium fluorescein concentration
$Ec_2(f)$	one-dimensional spectrum of sulforhodamine 101 concentration
$Eu_b(f)$	one-dimensional spectrum of downstream velocity in the turbulent background
$Ev_b(f)$	one-dimensional spectrum of horizontal velocity in the turbulent background
$Ew_b(f)$	one-dimensional spectrum of vertical velocity in the turbulent background
$E_Z(\kappa_1\eta)$	one-dimensional normalized concentration difference spectrum

F	fluorescence intensity
F_{cf}	species concentration calculated by curve fit
f	frequency
f_l	lens focal length
f_c	cut-off frequency
f_η	Kolmogorov frequency
f_{min}	minimum chopping frequency
$f(V_i)$	standardized normal Gaussian distribution function
g	gravitational acceleration
h	Planck's constant (6.62×10^{-27} erg-sec)
I_0	incident radiant power
K_Z	kurtosis of the normalized concentration difference
L_b	non-dimensional buoyancy lengthscale
M	centre to centre distance between PVC outlets
M_i	magnification
$N(f)$	noise spectrum
R	total resistance
Re	Reynolds number based on u_0, d, and v
Re(x)	local Reynolds number
Re_λ	Taylor scale Reynolds number
r	jet radial coordinate
$r(x)$	local jet radius
$r_{1/2}$	jet velocity half-radius
$r_{c,1/2}$	scalar half-radius
s	object distance
$S(f)$	noise-subtracted spectrum
S_Z	skewness of the normalized concentration difference
s''	image distance
s_{ij}	fluctuating rate of strain tensor
Sc	Schmidt number based on D and v
Sc_α	Schmidt number of species α
t	time
t^*	non-dimensional time
U	mean axial velocity component
U_b	mean downstream velocity in the turbulent background
U_{cl}	mean centreline axial velocity
$U_{cl}(x)$	local mean axial centreline velocity component
u	fluctuating axial velocity component
u_b	downstream velocity component in the turbulent background
u_i	fluctuating velocity in the i-direction
u_0	jet exit velocity
u^*	non-dimensional velocity
u'_{cl}	root-mean square of jet axial centreline velocity
$u'_{cl}(x)$	local root-mean square of jet axial centreline velocity

u_{rms}	root-mean square of fluctuating downstream velocity component in the turbulent background
V	mean radial velocity component
V_b	mean transverse horizontal velocity in the turbulent background
V_i	independent variable
V_{in}	input voltage to unity-gain operational amplifier
V_{out}	output voltage of unity-gain operational amplifier
V_1	voltage output corresponding to disodium fluorescein PMT
V_2	voltage output corresponding to sulforhodamine 101 PMT
v	fluctuating radial velocity component
v_b	transverse horizontal velocity component in the turbulent background
v_{rms}	root-mean square of fluctuating transverse horizontal velocity component in the turbulent background
x	jet axial coordinate
x_i	coordinate in the i-direction
x_0	virtual origin
x^*	non-dimensional local coordinate
Y_i	mass fraction of species i
$Y_{i,1}$	mass fraction of species i in stream 1
$Y_{i,2}$	mass fraction of species i in stream 2
W_b	mean vertical velocity in the turbulent background
w_b	vertical fluctuating velocity component in the turbulent background
w_{rms}	root-mean square of fluctuating vertical velocity component in the turbulent background
Z	normalized concentration difference (normalizing by local concentration)
Z_n	normalized concentration difference (normalizing by nozzle concentration)
Z_{rms}	root-mean square of the normalized concentration difference
$Z_{rms,meas}$	measured root-mean square of the normalized concentration difference
z	difference in mixture fractions
z_{rms}	root-mean square of difference in mixture fractions

Greek Symbols

ϕ_f	quantum efficiency
β	molar absorptivity
ε	turbulent kinetic energy dissipation rate
η	Kolmogorov lengthscale
η_B	Batchelor lengthscale
$\theta(f)$	optimal filter
κ	wavenumber
κ_1	longitudinal wavenumber

λ	Taylor microscale
λ_a	wavelength of absorbed/emitted light
λ_l	wavelength of laser beam
μ_{off}	average off time of random jet array pumps
μ_{on}	average on time of random jet array pumps
ν	kinematic viscosity
ξ_i	mixture fraction of species i
π	3.1415926
ρ_j	jet fluid density
ρ_w	density of water (1000 kg/m^3)
ρ_∞	background fluid density
σ_{off}	standard deviation of off time
σ_{on}	standard deviation of on time
τ	Kolmogorov time scale
υ	Kolmogorov velocity scale
υ_a	frequency of absorbed/emitted light

Superscripts and Symbols

*	pertains to non-dimensional parameter
'	pertains to root-mean square quantity
°	degree
$\langle \cdot \rangle$	denotes averaging

Subscripts

cl	pertains to centreline quantity
rms	pertains to root-mean square quantity
A,B	pertains to species A and B, respectively
i	index in tensor notation and pertains to species i
j	index in tensor notation and pertains to species j
α	pertains to species α

Acronyms

ADV	acoustic Doppler velocimeter
CMC	conditional moment closure
DNS	direct numerical simulation(s)
EDQNM	eddy-damped quasi-normal Markovian
JPDF	joint probability density function
LED	light emitting diode
LIF	laser-induced fluorescence
LSR	Lagrangian spectral relaxation
PDF	probability density function

PIV	particle-image velocimetry
PMT	photomultiplier tube
PVC	polyvinyl chloride
RDT	rapid distortion theory
RMS	root-mean square
SNR	signal-to-noise-ratio

Chapter 1

Introduction

1.1 Background

Scalar mixing within turbulent flows is a common occurrence in many engineering and environmental applications, including heat transfer, combustion, oceanic science, and pollutant dispersion. A number of studies focusing on scalar mixing have been completed; however, due to the complexity of turbulent flows, the vast majority have concentrated on a single scalar. Nonetheless, it is common for turbulent flows to transport more than one scalar. Examples include reacting flows (such as combustion processes) and the oceanic mixed layer, where both temperature and salinity are transported.

Whenever multiple scalars with differing molecular diffusivities (D) are being transported by a turbulent flow, there exists the possibility that they might evolve differently. If the scalars are initially perfectly correlated and possess identical initial and boundary conditions, then their separate evolution is due solely to differences in their molecular diffusivities. This phenomenon is called differential diffusion. Its effects are molecular in origin, since they arise from differences in molecular diffusivities. Therefore, Kolmogorov's (1941) theory implies that they should be negligible as the Reynolds number approaches infinity.

1

Currently, most turbulent mixing models neglect differential diffusion effects by making one of two assumptions. The first is to assume equal molecular diffusivities for all the scalars, thereby reducing the number of equations to be solved (since each scalar will then be governed by the same advection-diffusion equation). The second assumption is to neglect the effects of molecular diffusivity at high Reynolds numbers, assuming that the turbulent transport terms are much greater than the molecular transport terms (Yeung and Pope 2003). The former assumption is clearly incorrect, and the application of the latter assumption is questionable given the moderate Reynolds numbers of most practical flows.

In certain flows, small-scale effects can have a significant impact on the overall dynamics. One such example is combustion, which often occurs at low to moderate Reynolds numbers. Even small differences in instantaneous concentrations - due to differing molecular diffusivities between the fuel and oxidizer - can impact the overall efficiency of the process. Therefore, the consequences of differential diffusion can be significant.

1.2   Objectives

This work is an experimental investigation into the effects of differential diffusion of two passive scalars in a momentum-driven, axisymmetric, turbulent water jet issuing into both quiescent and turbulent backgrounds. Several objectives have been established in this study. These objectives include two primary goals and multiple secondary goals, which will be simultaneously achieved.

Before presenting the objectives, a brief discussion on the use of passive scalars is warranted. Passive scalars were preferred given that their presence in the flow will not affect the velocity field, thus eliminating the possibility of inertial effects. Such effects can be important in certain flows; however, they make it difficult to isolate the effects of differential diffusion. Therefore, the flow in the present study will consist of two fluorescent dyes mixed in water in dilute concentrations, so as to ensure the absence of inertial effects.

One primary objective of this work is to systematically study the Reynolds number dependence (Re $= u_0 d / \nu$, where u_0 is the jet exit velocity, d is the jet nozzle

2

diameter, and v is the kinematic viscosity) of differential diffusion in a turbulent jet. To date, there has not been a systematic study examining this dependence. Differential diffusion effects depend on the Reynolds number and are believed to become negligible at high Reynolds numbers. This hypothesis will be tested by varying the Reynolds number. Any scaling of differential diffusion effects with Reynolds number will also be sought. To accomplish this objective, the Reynolds number will be varied from a low value (Re = 900) to a high value (Re = 10600). The lowest Reynolds number (Re = 900) achievable is determined by experimental constraints (see section 4.2). The high Reynolds number value (10600) is chosen to be above the mixing transition, where turbulent jet flow becomes fully-developed (Dimotakis 2000), while still lying within the constraints imposed by the apparatus.

The second primary objective of this work is to systematically study the effect of radial position on differential diffusion in a jet. This will be accomplished by taking measurements at different radial positions from the centre of the jet out to its edges. Of particular interest are the disparities in differential diffusion effects between points near the axis of the jet and points near the jet edges. There is a difference in flow characteristics between the centre and edges of the jet, as the variances of (velocity and scalar) fluctuations increase near the edges where entrainment of ambient fluid occurs. Comparing these regions will highlight any changes in differential diffusion, caused by the differences in the nature of the flow.

The Schmidt number (Sc = v/D) is another key parameter when studying differential diffusion. Its magnitude affects the scalar fluctuations and the size of the smallest (dissipative) scales of the scalar. For Schmidt numbers of order 1 (typical of gas-phase flows), the scalar fluctuations are dissipated at scales of the same order as the Kolmogorov length scale (the smallest velocity length scale). However, for Schmidt numbers much greater than 1 (typical of dyes in water) the scalar fluctuations are dissipated at a smaller scale, the Batchelor scale (Batchelor 1959), which decreases with increasing Schmidt number. The majority of previous studies on differential diffusion have been performed using scalars with Schmidt numbers of order 1. Heretofore, differential diffusion has only been studied at low Reynolds number when the flow consisted of high Schmidt number scalars. This work is conducted using scalars with

3

Schmidt numbers of order 10^3. Therefore, the results will elucidate differential diffusion effects, over a range of Reynolds numbers (extending to moderate values) in a flow containing high Schmidt number scalars.

Another objective is to determine the scales at which differential diffusion occurs. Spectra of the normalized concentration difference will be calculated to achieve this goal. Heretofore, spectral analysis of differential diffusion has only been applied to numerical studies. This will therefore be the first investigation to measure the spectrum of the normalized concentration difference. Once spectra of concentration differences are obtained, the scales where differential diffusion manifests itself will be directly known. In particular, it is desirable to determine if differential diffusion effects persist at scales larger than the Kolmogorov scales. This will be revealed by analyzing the spectra at scales larger than the Kolmogorov scales.

The final goal of this work is to determine the effects of background turbulence on differential diffusion in the jet. Many practical flows do not evolve in a stagnant background, but rather one that is turbulent. Therefore, it is of inherent interest to carry out experiments with the jet issuing into a turbulent background. This will be accomplished by conducting experiments with the jet issuing into a background of approximately homogeneous, isotropic turbulence with zero-mean flow. Comparing these results to experiments done in a quiescent background will give an indication of the effect of the background turbulence.

1.3   Organization of the Thesis

The remainder of this thesis is structured as follows. In Chapter 2, a review of the literature on turbulent jets, laser-induced fluorescence, and differential diffusion will be presented. The section on turbulent jets will review their scaling, the impact of different initial conditions on their development, and the evolution of turbulent jets in a turbulent background. This will be followed by an overview of the use of laser-induced fluorescence as a technique to measure scalar concentrations. Finally, previous numerical and experimental studies of differential diffusion will be discussed.

Chapter 3 will briefly review some theoretical considerations. Firstly, the theory of passive scalar transport (leading to some basic equations describing differential

4

diffusion) will be developed. This will be followed by a section presenting basic fluorescence theory.

A description of the experimental setup will be provided in Chapter 4. This will include a detailed overview of the apparatus used to perform the experiments, along with the signal detection and data acquisition equipment. This chapter will also contain a section detailing how the detected fluorescence signal is related to species concentration. The final section will describe some of the procedures implemented to ensure that the fluorescence signal was not adversely affected by several potential sources of error.

Chapter 5 will serve to describe the experimental conditions and validate the flow. The necessary theoretical and empirical correlations (used to determine the various length and time scales in the jet) will be introduced in the first section. These correlations will include formulae for determining parameters, such as the mean centreline axial velocity and turbulent kinetic energy dissipation rate in a jet. In the next section, the experimental conditions will be presented along with their respective length and time scales. This will be followed by a section on the measures taken to verify the independence of individual species concentration measurements. The flow will then be validated by comparing individual species concentration statistics to those obtained in previous studies.

The results of the experiments will be presented in Chapter 6. Time series, variances, spectra, probability density functions (PDFs), and conditional expectations of the normalized concentration difference will be presented for the various experimental conditions. Each section will contain a brief discussion in which the results will be compared to previous studies. This chapter is divided into two main sections: one presenting the results for experiments performed when the jet issued into a quiescent background, and the other presenting results from experiments performed when the jet issued into a turbulent background. The quiescent background section will be divided into five subsections. These will include discussions of scalar concentration and normalized concentration difference time series, r.m.s. fluctuations of the normalized concentration difference, measured spectra of the normalized concentration difference, PDFs of the normalized concentration difference, and conditional expectations of

5

individual scalars and the normalized concentration difference. The results from the turbulent background will be presented in one continuous section.

Chapter 7 will address two main issues: i) the effect of entrainment of ambient fluid on differential diffusion, and ii) the behaviour of the spectrum of the normalized concentration difference. Three instances in which the entrainment of ambient fluid affects differential diffusion will be reviewed. This chapter will conclude with a discussion of the form of the normalized concentration difference spectrum. Firstly, spectra previously calculated in numerical studies will be reviewed. Then the normalized concentration difference spectra measured in this study will be discussed and compared with those from the numerical studies.

The final chapter of this thesis, Chapter 8, will present the conclusions of this work. The first section will review all chapters and highlight the pertinent results. This will be followed by a discussion of the novel contributions of this study. Finally, there will be a brief section outlining recommendations for future work.

Chapter 2

Literature Review

The subject of turbulence is extensive and thousands of articles and texts on the topic exist. Therefore, a full description of turbulence is beyond the scope of this work. However, some examples of texts which give a general description of turbulent flows include: Batchelor (1953), Tennekes and Lumley (1972), Hinze (1975), and Pope (2000). The goal of the remainder of this literature review is to present work directly related to this thesis; namely turbulent jets, the turbulence measurement technique employed in this work (laser-induced fluorescence), and differential diffusion in turbulent flows.

2.1 Turbulent Jets

The flow under consideration is from a momentum-driven, axisymmetric, turbulent jet. Turbulent jets are relatively simple inhomogeneous flows that frequently occur in practical applications. Therefore, an extensive number of experimental, numerical and theoretical studies focusing on various aspects of turbulent jets have been completed. These studies have led to a firm understanding of the basic characteristics of this flow. Examples of works giving an overview of turbulent jets and their dynamics

include: Monin and Yaglom (1971), Tennekes and Lumley (1972), Townsend (1976), Rajaratnam (1976), Rodi (1982) and Pope (2000).

Turbulent jets are free shear flows that can be characterized by applying the boundary layer approximations to the equations of motion (i.e., the transverse gradients are much larger than the (downstream) axial gradients (Pope 2000)). In the case of a statistically stationary and axisymmetric turbulent jet, the mean flow is two-dimensional and only dependent on the axial and radial directions. The turbulent-boundary layer equations for this flow reduce to the continuity and axial momentum equations (Pope 2000):

$$\frac{\partial \langle U \rangle}{\partial x} + \frac{1}{r}\frac{\partial (r \langle V \rangle)}{\partial r} = 0 \qquad (2.1)$$

$$\langle U \rangle \frac{\partial \langle U \rangle}{\partial x} + \langle V \rangle \frac{\partial \langle U \rangle}{\partial r} = \frac{v}{r}\frac{\partial}{\partial r}\left(r \frac{\partial \langle U \rangle}{\partial r} \right) - \frac{1}{r}\frac{\partial}{\partial r}\left(r \langle uv \rangle \right) \qquad (2.2)$$

where U is the axial velocity, x is the axial coordinate, V is the radial velocity, r is the radial coordinate, u is the fluctuating axial velocity, v is the fluctuating radial velocity, and $\langle \cdot \rangle$ denotes averaging. The axial momentum equation is often further simplified, except near walls, by assuming that the turbulent stress is much larger than the viscous stress. The relative simplicity of the above equations has led to a number of theoretical studies on turbulent jets (Hussein *et al.* 1994).

One important characteristic of the velocity field in a turbulent jet is that profiles of the mean axial velocity, mean lateral velocity, and the Reynolds stresses all become self-similar after initial flow development in the near-field region (Wygnanski and Fiedler 1969, Panchapakesan and Lumley 1993a, and Ferdman *et al.* 2000). The location of the beginning of the self-similar region depends on the initial conditions as well as the quantity being measured. Regardless of initial conditions, the mean velocity reaches a self-similar state well before the Reynolds stresses.

The two typical initial conditions for a turbulent jet are a contracting nozzle (resulting in a top hat velocity profile at the jet exit) and flow from a long pipe (resulting in a fully-developed pipe flow velocity profile at the jet exit). The mean velocity profile becomes self-similar by 15 jet diameters downstream of the jet exit and the Reynolds stresses by 40 jet diameters, for flow emanating from a long pipe (Ferdman *et al.* 2000).

8

Similarly, the mean axial velocity becomes self-similar by 15 jet diameters downstream of the jet exit for a jet with a contracting nozzle; however, in this instance the Reynolds stresses become self-similar further upstream, within 25 jet diameters of the jet exit (Xu and Antonia 2002).

The self-similar nature of turbulent jets leads to the application of a theoretical analysis to determine the scaling behaviour of the mean axial velocity and the jet spreading rate. Either proper manipulation of the continuity and momentum equations or dimensional analysis will yield the scaling behaviour of the mean axial velocity and the transverse lengthscale, often selected as the radial location at which the mean axial velocity is either one-half or e^{-1} of the mean centreline axial velocity (Fischer *et al.* 1979), in the self-similar region. The mean centreline axial velocity scales inversely with downstream distance ($U \propto x^{-1}$) while the jet half-radius, i.e., transverse lengthscale, scales with downstream distance ($r_{1/2} \propto x$), each independent of the Reynolds number (Rajaratnam 1976). These scaling relations have been verified by experimental studies (including Wygnanski and Fiedler 1969, Rodi 1975, Panchapakesan and Lumley 1993a, Hussein *et al.* 1994, Ferdman *et al.* 2000, and Xu and Antonia 2002). An important consequence of the above scaling is that the local Reynolds number ($Re(x) = \dfrac{U_{cl}(x)r(x)}{\nu}$, where $U_{cl}(x)$ is the local mean centreline axial velocity and $r(x)$ is the local half-radius) does not vary with downstream position (Landau and Lifshitz 1959).

The above scaling laws for the mean centreline axial velocity and the spreading rate are valid in axisymmetric turbulent jets, regardless of initial conditions. However, the jet initial conditions can have an influence on their decay. Xu and Antonia (2002) have experimentally shown that the mean centreline axial velocity decays slightly faster in a "contraction jet" than in a "pipe jet". They also observed a slightly faster spreading in a contraction jet than in a pipe jet. These trends were also observed in the direct numerical simulations of Boersma *et al.* (1998). On the other hand, in the far field, the different initial conditions had minimal effect on turbulent fluctuations, as differences in centreline turbulence intensities (normalized by the mean centreline axial velocity) were less than experimental uncertainty (Xu and Antonia 2002).

As mentioned above, the Reynolds stresses also become self-similar in the far-field of a turbulent jet. The root-mean-square (r.m.s.) of the axial centreline velocity, $u'_{cl} \equiv \langle u^2 \rangle_{r=0}^{1/2}$, is often a statistic of interest when characterizing a jet. When normalized by the mean axial centreline velocity, $u'_{cl}(x)/U_{cl}(x)$, this statistic asymptotes to a constant value of approximately 0.24, independent of Reynolds number, in the self-similar region (Panchapakesan and Lumley 1993a).

Passive scalars in turbulent jets exhibit a similar behaviour to that of the velocity field. For instance, certain statistical quantities of the scalar field also exhibit self-similarity, after development in the near-field region. Past experimental work indicates that both the mean ($\langle C \rangle$) and scalar variance become self-similar (Wilson and Danckwerts 1964, Becker et al. 1967, Birch et al. 1978, Lockwood and Moneib 1980, and Dowling and Dimotakis 1990). Similar to the mean axial velocity, the mean scalar concentration becomes self-similar approximately 10 jet diameters downstream of the jet exit (Wilson and Danckwerts 1964 and Lockwood and Moneib 1980). The decay of the mean scalar along the centreline is also akin to that of the mean axial centreline velocity, as it also scales inversely with downstream distance ($C \propto x^{-1}$) (Wilson and Danckwerts 1964). Wilson and Danckwerts also observed the scalar half-width to scale proportionally to downstream distance ($r_{C,1/2} \propto x$, where $r_{C,1/2}$ is the scalar half-radius). Experimental investigations have found that, similar to Reynolds stresses, scalar fluxes are self-similar in the far-field region (Wilson and Danckwerts 1964, Lockwood and Moneib 1980 and Panchapakesan and Lumley 1993b). Wilson and Danckwerts (1964) and Lockwood and Moneib (1980) both noticed the self-similar region for scalar fluxes to begin about 40 jet diameters downstream of the jet exit, at approximately the same distance as the Reynolds stresses.

Scalar r.m.s. fluctuations ($c_{rms} = \langle c^2 \rangle^{1/2}$, where c is the scalar fluctuation) display a dependence on both the Reynolds and Schmidt numbers of the flow (unlike r.m.s. velocity fluctuations). The effect of both Reynolds and Schmidt numbers can be seen when comparing the centreline r.m.s. scalar fluctuations normalized by the centreline

mean scalar concentration ($\frac{c_{rms}}{\langle C \rangle}$), in liquid-phase flows to those in gas-phase flows. In gas-phase flows, which typically have Schmidt numbers of order 1, the normalized centreline r.m.s. scalar fluctuations are constant with Reynolds number (Dowling and Dimotakis 1990). However, in liquid-phase flows, which often have Schmidt numbers of order 10^3, the normalized centreline r.m.s. scalar fluctuations steadily decrease as the Reynolds number increases up to Re $\sim 10^4$, at which point they begin to asymptote to a value similar to that in gas-phase flows (Miller 1991 and Miller and Dimotakis 1991). These variations in normalized centreline r.m.s. scalar fluctuations indicate that certain effects in turbulent jets, such as differential diffusion, can be dependent on both the Reynolds and Schmidt number.

The above studies do not account for the evolution of a turbulent jet issuing into a turbulent background, a common occurrence in practical flows. The development of turbulent jets in such conditions has received little attention and is not well understood (Anfossi *et al.* 1993). However, to improve the understanding of this topic, there have been recent studies investigating turbulent jets that issue into turbulent fields (e.g. Hunt 1994, Guo *et al.* 1999, and Gaskin *et al.* 2004).

Hunt (1994) presented a theoretical study describing the evolution of jets and plumes in turbulent conditions. In this work, he reasoned that at downstream locations where the r.m.s. velocity fluctuations in the jet are greater than those in the external turbulence, the entrainment of external fluid into the jet will increase as compared to that under quiescent conditions. However, when the intensity of the background turbulence is the same order as that in the jet, the structure of the jet will change. This change will result in a significant increase in the jet spreading angle. When this occurs, there will be entrainment reversal, i.e., extrainment of jet fluid into the surrounding ambient fluid.

Ching *et al.* (1995) studied the effect of background turbulence on turbulent plumes. In their experiments, they observed a breakdown of the plume structure, resulting in an increased spreading angle, when the turbulent intensity of the background was at least 0.625 the convective velocity of the plume. This work motivated Guo *et al.* (1999) to perform experiments to investigate the effects of background turbulence on the evolution of a turbulent jet. They conducted their experiments in a turbulent jet, with

Reynolds numbers ranging from 960 to 5500, evolving in a turbulent background created by an oscillating grid. Their results indicated that the jet structure breaks down in a similar manner to that reported for plumes by Ching *et al.* (1995), and as predicted for jets by Hunt (1994). At all jet Reynolds numbers, Guo *et al.* (1999) noticed a breakdown of the structure of the jet when the r.m.s. velocity fluctuations of the external turbulence were greater than 0.125 of the jet's mean centreline axial velocity. This breakdown was characterized by a sudden increase in the diffusion angle, i.e., an increase in the spreading of the jet. When this occurred, there was extrainment of jet fluid into the surrounding fluid, as predicted by Hunt (1994).

The effect of ambient turbulence on a co-flowing jet has also been studied (Wright 1994 and Gaskin *et al.* 2004). Wright (1994) observed a downstream breakdown of the jet structure and a more rapid decay of mean quantities due to the ambient turbulence. Gaskin *et al.* (2004) also noticed an increase in the decay of the mean jet velocity in their planar jet issuing into a turbulent co-flow. They reported that the jet structure destructed downstream, as the ratio of the turbulence intensities in the co-flowing stream to those in the jet increased. As expected, this breakdown in the jet structure occurred closer to the jet nozzle when the turbulence intensity in the co-flowing stream was amplified.

2.2 Measurement Technique

Laser-induced fluorescence (LIF) is a non-intrusive technique that is frequently employed to measure instantaneous species concentrations. The ability to couple a fast frequency response with high spatial resolution makes LIF an ideal measurement technique for turbulent flows. In this technique, the flow, which can be either a liquid or a gas, is seeded with a fluorescent tracer that emits photons when irradiated by a laser. The photons are emitted at a higher wavelength than that of the laser, and they can therefore be independently sensed by a photodetector, such as a photomultiplier tube (PMT) (i.e., Walker 1987, Miller and Dimotakis 1991, Saylor and Sreenivasan 1998, Wang and Fiedler 2000a), a photodiode (i.e., Dowling *et al.* 1989, Shan *et al.* 2004), or a CCD camera (i.e., Cetegen and Mohamad 1993, Coppeta and Rogers 1998, Crimaldi and Koseff 2001, Deusch and Dracos 2001, Tian and Roberts 2003). The output from the

photodetector can then be related to the concentration of the fluorescent tracer. Furthermore, as long as the fluorescent tracer is seeded at a low enough concentration, the relation between the detected signal and the tracer concentration is linear (see section 3.2).

Studies employing LIF have been conducted since the works of Owen (1976) and Dewey (1976) were published. Other early works contributing to the development of LIF include: Breidenthal (1981), Dyer and Crosley (1982), Kychakoff *et al.* (1982), Koochesfahani and Dimotakis (1985), and Walker (1987), among others. LIF continues to be a common tool for measuring species concentrations, with more recent studies including Miller (1991), Cetegen and Mohamad (1993), Houcine *et al.* (1996), Crimaldi (1997), Saylor and Sreenivasan (1998), Camussi *et al.* (2002), Su and Clemens (2003), Gordon *et al.* (2004), and Aguirre and Catrakis (2005), among others.

LIF can be applied to obtain results at either a point or in a plane. Punctual measurements are typically made by considering a focused spot along a laser line (i.e., Koochesfahani and Dimotakis 1985, Walker 1987, Crimaldi 1997, Saylor and Sreenivasan 1998). Two-dimensional planar measurements are often made by using a cylindrical lens to create a laser sheet (Kychakoff *et al.* 1982, Cetegen and Mohamad 1993, Coppeta and Rogers 1998, Guillard *et al.* 1998). Recently, work has been done to further extend the capabilities of LIF by rapidly sweeping a laser sheet, so as to obtain measurements in a three-dimensional volume (i.e., Deusch *et al.* 2000, Deusch and Dracos 2001, Tian and Roberts 2003, Van Vliet *et al.* 2004).

Although numerous studies have utilized LIF to obtain instantaneous species concentrations, only a few have concentrated on the details of the technique itself. When employing LIF, or any other measurement technique, it is desirable to have a high signal-to-noise-ratio (SNR) along with a fine spatial resolution. Koochesfahani and Dimotakis (1985) took into account variations in laser uniformity to improve the resolution of detected scalar concentration signals, along a line, in their LIF measurements in a liquid-phase shear layer. Guillard *et al.* (1998) also discussed resolution of detected scalar concentration signals in their work to develop a quantitative technique to obtain planar LIF measurements in an impinging jet. As experimental techniques advance and the measurement of smaller scales is sought, studies need to be conducted with increasingly

13

finer spatial resolution. However, the improved resolution can lead to a decrease in the SNR. To this end, Wang and Fiedler (2000b) focused their LIF study on the effects of a fine measurement volume, 4 $(\mu m)^3$, on the SNR. They accomplished this by obtaining measurements in a confined mixing layer, which was inside a water channel. Due to the extremely small measurement volume, their detected fluorescence signal was low. Hence, the SNR was also low, as the photon shot noise from their photon detection devices (PMTs) was more dominant than that from a strong fluorescent signal. They attempted to increase the fluorescent signal, and thus the SNR, by increasing the fluorescent tracer concentration and/or laser power. Although these actions led to an increased SNR, there were competing effects as they observed that each action could lead to an increase in photobleaching and thermal blooming effects (see below). They also showed that an increase in the fluorescent tracer concentration could result in a non-linear response of the photodetector (see section 3.2).

Whenever LIF is being employed, there is the possibility of photobleaching (the degradation of a fluorescent signal due to constant irradiation). The occurrence of photobleaching in fluorescent tracers has been known for many years (e.g. Guilbault 1973). However, photobleaching in LIF experiments has not received significant attention. Koochesfahani (1984) did take photobleaching into account in his experiments, and calculated a photobleaching time constant based on the laser photon flux, dye absorption cross section, and bleaching quantum efficiency.

Since the work of Koochesfahani (1984), a few other studies have focused on studying photobleaching effects. Saylor (1995) determined the photobleaching of a single fluorescent dye (disodium fluorescein). In this work, he proposed using a half-life (the time for the fluorescent signal to degrade by one-half of its peak) to quantify photobleaching effects. Under his experimental conditions, Saylor found photobleaching to be a rapid process. He found the half-life of disodium fluorescein to be 2.9 ms. However, this half-life is not universal, as it is dependent on the experimental conditions. Photobleaching has been shown to be a function of both the fluorescent dye concentration and laser power (Sahar and Treves 1977 and Benson et al. 1985). Crimaldi (1997) found that photobleaching effects also depend on the choice of fluorescent dye and the velocity of the flow. Wang and Fiedler (2000a) confirmed that photobleaching is

dependent on dye concentration, laser power and flow velocity. They showed that photobleaching effects can be reduced by decreasing either the laser power or dye concentration or increasing the velocity of the flow.

Another concern when using LIF to obtain concentration measurements that has received little attention is thermal blooming. Thermal blooming occurs when the energy from the laser beam heats the fluorescent dye, causing the beam to diverge. This beam divergence can result in a weaker fluorescence signal (Koochesfahani 1984). Koochesfahani's study was the first to introduce thermal blooming as a possibility for corrupted fluorescent signals. Wang and Fiedler (2000a) studied thermal blooming effects along with photobleaching. They pointed out that photobleaching and thermal blooming are related since they both depend on the velocity of the flow. This effect can be visualized by considering a parcel of fluid that is continuously irradiated by a laser. The longer the time period of continuous irradiation, the greater the chance that the parcel is heated enough to result in thermal blooming. As mentioned above with photobleaching, Wang and Fiedler found that thermal blooming is also dependent on laser power. Their results indicate that thermal blooming effects can be decreased by decreasing laser intensity and/or increasing the velocity of the flow.

2.3 Differential Diffusion

Differential diffusion can occur whenever multiple species, with differing molecular diffusivities, are mixed in a flow. Bilger (1977), when he recast the data of Tsuji and Yamaoka (1971), noted that differential diffusion was partially responsible for differences in mass fractions in a methane diffusion flame issuing from a porous cylinder. This data showed differences in normalized mass fractions of oxygen and nitrogen, which were particularly prevalent away from the cylinder. Bilger (1977) attributed these differences to differential diffusion. This work provided motivation to further investigate differential diffusion. In such studies, it is beneficial to be able to isolate and quantify the differential diffusion effects. Therefore, theoretical equations to describe differential diffusion were first presented by Bilger (1981), for turbulent diffusion flames, and by Bilger and Dibble (1982), for non-reacting flows.

Based on the mixture fractions of the species in a flow, Bilger and Dibble (1982) defined a variable, z, to quantify the effects of differential diffusion in a two-stream mixing problem, such as a jet issuing into co-flowing fluid. The mixture fraction for species i was defined as:

$$\xi_i \equiv \frac{Y_i - Y_{i,2}}{Y_{i,1} - Y_{i,2}} \qquad (2.3)$$

where Y_i is the mass fraction of species i, and $Y_{i,1}$ and $Y_{i,2}$ are the mass fractions of species i in the incoming streams 1 and 2. When two species are present (i and j), differential diffusion effects can be quantified by considering the difference in the two mass fractions:

$$z \equiv \xi_i - \xi_j. \qquad (2.4)$$

A significant number of numerical and experimental studies focusing on differential diffusion have been undertaken since the work of Bilger and Dibble (1982). The numerical studies have included direct numerical simulations (DNSs) (i.e., Yeung and Pope 1993, Nilsen and Kosály 1997, and Yeung 1998) as well as various models (i.e., Kerstein 1990, Kerstein et al. 1995, Kronenburg and Bilger 1997, Fox 1999, Pitsch 2000). Experimental studies have been conducted in both reacting and non-reacting gas-phase flows (i.e., Drake et al. 1986, Smith et al. 1995b, and Bergmann et al. 1998) and in liquid-phase flows (Saylor and Sreenivasan 1998, Jackson and Rehmann 2003).

2.3.1 Numerical Studies of Differential Diffusion

A number of DNSs have been conducted to examine differential diffusion effects. In the first such work, Yeung and Pope (1993) performed DNSs to study differential diffusion of two passive scalars in stationary homogeneous, isotropic turbulence. One key characteristic of their simulations was that the scalar fields were decaying. This study was completed at a Taylor-scale Reynolds number of 38 ($\mathrm{Re}_\lambda = \frac{u_{rms}\lambda}{v}$, where

$\lambda \equiv \left[\frac{\langle u_{rms}^2 \rangle}{(\partial u_{rms}/\partial x)} \right]^{1/2}$ is the Taylor microscale, u_{rms} is the r.m.s. velocity and x is a spatial coordinate) with Schmidt numbers ranging from 0.25 to 1.0. The correlation coefficient

of the scalars (and also that of their gradients) was ultimately seen to completely decorrelate, a strong indication of the presence of differential diffusion as it implies that the scalars have evolved separately from each other. The coherency spectrum, which is essentially a spectral representation of the correlation coefficient, was also studied. It was seen to exhibit a reverse cascade, as incoherency propagated from the small to large scales, indicating that differential diffusion effects also propagate from the small to large scales. This was also the first study to calculate the spectrum of the difference between the scalars. The results indicated that, under these conditions, at early times the spectrum will increase with wavenumber until peaking at the high wavenumber end. At later times, greater than 8 eddy turnover times, the spectrum had a different form as it peaked at the low wavenumber end and then continually decreased with increasing wavenumber.

The spectral mechanisms of differential diffusion were studied by Yeung (1996). He performed DNSs in stationary isotropic turbulence with and without mean scalar gradients. These simulations were performed at a Taylor-scale Reynolds number of 90 without mean scalar gradients and at a Taylor-scale Reynolds number of 160 in the presence of imposed mean scalar gradients. The Schmidt number range of the scalars in this work was from 1/8 to 1, with two scalars present in each simulation. There were clear differences between the results of the flows with imposed mean scalar gradients to those without. The simulations done with mean scalar gradients, which served to provide a source of production for the scalar fields, showed that the large scales remained coherent at all times and, therefore, differential diffusion effects only persisted at the small scales. Yeung attributed this large scale correlation to be from the coherent source of scalar fluctuations. However, when no mean scalar gradients were present, resulting in decaying scalar fields, the large scales eventually decorrelated, indicating that differential diffusion effects had propagated to these scales.

Nilsen and Kosály (1997) performed DNSs to study differential diffusion of two initially identically distributed scalars in isotropic turbulence. Their velocity field, with a Taylor-scale Reynolds number ranging from 19 to 87, was meant to simulate experimental studies conducted in grid turbulence. They obtained results which showed the scalars decorrelated over time; consistent with Yeung and Pope (1993). However, a key difference between their work and that of Yeung and Pope (1993) was in their

17

calculated difference spectrum. Nilsen and Kosály (1997) presented a difference spectrum that was increasing at low wavenumbers and centred with a peak at the high wavenumber end. This differed from Yeung and Pope (1993) who reported similar results at early times; however, at later times their difference spectrum was centred at low wavenumbers and decreased with increasing wavenumber. As pointed out by Nilsen and Kosály (1997), the discrepancy was most likely due to a difference in flow conditions and/or the length of the simulations. Nilsen and Kosály's (1997) simulations occurred in decaying turbulence and, thus, they were only able to span about 3.5 eddy turnover times. On the other hand, Yeung and Pope (1993) were able to span up to 65 eddy turnover times in their simulations. Nilsen and Kosály (1997) also determined the scaling of the variance of the scalar difference, and reported results which were consistent with the scaling predicted by Kerstein et al. (1995).

Two parameters of inherent interest when studying differential diffusion are the Reynolds and Schmidt numbers. Both are limiting factors in performing a DNS, since the computational requirements increase with each parameter. Simulations utilizing both larger Schmidt and Reynolds numbers can be conducted as computing capabilities improve. Yeung (1998) was able to improve upon an earlier lower Reynolds number DNS (Yeung and Pope 1993), as he executed DNSs at Taylor-scale Reynolds numbers up to 230. These simulations were performed in stationary isotropic turbulence consisting of two scalars per simulation, with Schmidt numbers from 1/8 to 1. The results indicated an increase in the correlation of the scalars as the Reynolds number increased; however, at the larger Reynolds numbers the scalars were still uncorrelated at the small scales. Yeung et al. (2000) were also able to conduct simulations with larger Schmidt numbers than previous DNSs (e.g. Yeung and Pope 1993, Nilsen and Kosály 1997). They did this by performing DNSs in stationary isotropic turbulence at a Taylor-scale Reynolds number of 38 with Schmidt numbers up to 4.0. Their results indicated a weak transfer in the scalar field from high to low wavenumbers, which was strongly dependent on Schmidt number. This strong dependence provides impetus for studies to be completed at much higher Schmidt numbers.

The study of differential diffusion in reacting flows has also been attempted through the use of DNSs (Nilsen and Kosály 1999). They performed a DNS of two

reacting scalars in isotropic, decaying turbulence with Taylor-scale Reynolds numbers ranging from 19 to 87. The fuel was chosen to have a lower Schmidt number than the oxidant (which was assigned a Schmidt number of 1), as is often the case in a reacting flow. Similar to other DNSs in non-reacting flows (Nilsen and Kosály 1997 and Yeung 1998), the effects of differential diffusion were seen to decrease with increasing Reynolds number.

Models with the ability to describe differential diffusion effects were first employed by Bilger and Dibble (1982). In this work, they applied a k-ε model to a jet consisting of a hydrogen/propane mixture. The jet Reynolds number was 2700 and it issued into a co-flowing stream of air. The results indicated that differential diffusion effects were present, as the r.m.s. of z ($z_{rms} \equiv \langle z^2 \rangle^{1/2}$) was non-negligible, with instances of off-axis values slightly greater than 0.004.

Kerstein (1990) employed a linear-eddy model to determine the effects of differential diffusion in a turbulent jet consisting of a hydrogen/propane mixture issuing into air. At Reynolds numbers of 5000 and 20000, he found that z_{rms} was finite. He obtained an off-axis peak with values greater than 0.05 at a Reynolds number of 5000 and slightly less than 0.05 at a Reynolds number of 20000. At each Reynolds number, these values were obtained at a location 5 jet diameters downstream of the exit. From these results, it is evident that z_{rms} is smaller at higher Reynolds numbers, an indication that differential diffusion effects may decrease with increasing Reynolds number. Kerstein also observed a decrease in z_{rms} with downstream position. The above values decreased to approximately 0.025 and just below 0.025 at a downstream distance of 20 jet diameters for Reynolds numbers of 5000 and 20000, respectively.

A linear-eddy model was again used, by Kerstein *et al.* (1995), to test the scaling of the variance of the normalized concentration difference. They defined their normalized concentration difference as:

$$Z \equiv c_A - c_B \qquad (2.5)$$

where c_A and c_B are $\dfrac{C_A}{\langle C_A \rangle}$ and $\dfrac{C_B}{\langle C_B \rangle}$, respectively. The linear-eddy model was employed to simulate the mixing of two scalars with Schmidt numbers ranging from 0.01 to 1 in

one spatial dimension. The turbulent field had an imposed mean scalar gradient and was stationary and homogeneous with a Reynolds number ranging from 100 to 8000. The model's results indicate that the variance of the normalized concentration difference scales as $Re^{-1/2}$ ($\langle Z^2 \rangle \propto Re^{-1/2}$). This scaling is consistent with their similarity analysis, which also predicts the variance of the normalized concentration difference to scale as $Re^{-1/2}$.

The conditional moment closure (CMC) method has also been used to model differential diffusion (Kronenburg and Bilger 1997). In this work, a comparison was made between the CMC model and DNS data of differential diffusion of two passive scalars in a non-reacting flow. The DNS was performed with two scalars of Schmidt numbers ranging from 0.125 to 1.0. The flow in this study was decaying homogeneous, isotropic turbulence with a Taylor scale Reynolds number ranging from 12.51 to 50.04. This method proved to be effective in predicting differential diffusion by modelling the terms that deviate from the conditional mean.

Kronenburg and Bilger (2001a and 2001b) extended the CMC method to model differential diffusion in turbulent reacting flows. Kronenburg and Bilger (2001a) first developed the model in decaying homogeneous, isotropic turbulence. They showed that for reacting flows, the modelling of the terms which deviate from the conditional mean needs to be modified from that used in applying the CMC method to non-reacting flows. The reacting model was then applied to turbulent hydrogen-air jet flames (Kronenburg and Bilger 2001b). A comparison of the model's predictions with DNS results illustrated that the reacting flow model can be effective in jet diffusion flames.

Stochastic mixing models have also been employed to model differential diffusion effects (Chen and Chang 1998). Such models use a PDF method to model differential diffusion and can be applied to both turbulent reacting and non-reacting jets. The results of Chen and Chang (1998) showed that the model was effective in modelling differential diffusion in non-reacting jets, as the results from the model agreed well with the experimental data of Smith *et al.* (1995a). However, this model may not be as well suited for reacting jets, as there were discrepancies in its results when compared to the experimental data of both Smith *et al.* (1995b) and Meier *et al.* (1996).

A Lagrangian spectral relaxation (LSR) model has also been applied to treat differential diffusion of two passive scalars (Fox 1999). This formulation was studied in forced homogeneous, isotropic turbulence at four turbulent Reynolds numbers varying from 38 to 230. The simulations were conducted both with and without imposed uniform mean scalar gradients. The results indicated that the model performed satisfactorily when compared to DNS data. Using this model, the variance of the scalar difference scaled as $Re^{-0.3}$, a similar result to that from the linear-eddy model of Kerstein *et al.* (1995). This scaling also showed that the LSR model (Fox 1999) predicted a decrease in differential diffusion effects with increasing Reynolds number.

Pitsch and Peters (1998) and Pitsch (2000) employed flamelet formulations to model combustion. Pitsch and Peters (1998) first presented the flamelet formulation for non-premixed combustion, in which they defined the mixture fraction as a conserved scalar. Using this formulation, they were able to predict differential diffusion effects. Pitsch (2000) then extended the previous study by using a Lagrangian flamelet model to describe a turbulent $CH_4/H_2/N_2$ diffusion flame. This study showed that an unsteady flamelet model was capable of capturing differential diffusion effects.

Eddy-damped quasi-normal Markovian (EDQNM) theory has also been applied to study differential diffusion of two passive scalars in stationary isotropic turbulence (Ulitsky *et al.* 2002). This method was shown to have good agreement with DNS results for Taylor-scale Reynolds numbers ranging from 131 to 327 and Schmidt numbers ranging from 1/16 to 1.0. The EDQNM method also showed that differential diffusion is a molecular phenomenon and the presence of a mean scalar gradient acts as a coherent source for the large scales, consistent with the DNS results of Yeung (1996).

Rapid distortion theory (RDT) has been utilized to study differential diffusion of active and passive scalars in unsheared, initially isotropic turbulence (Jackson *et al.* 2005). The results showed scalar fluxes calculated using RDT compared well to DNS data (i.e., Gargett *et al.* 2003) and that curves of the diffusivity ratio, determined by integration of the calculated scalar fluxes, compared well to experimental data (i.e., Jackson and Rehmann 2003). The RDT results demonstrated that the method may be applicable to study differential diffusion in interior parts of the ocean, where the flow is stratified with weak turbulence.

2.3.2 Experimental Studies of Differential Diffusion

A number of experimental studies of differential diffusion have been conducted. These include investigations in both gas and liquid-phase flows. In this section, the non-reacting gas-phase studies will be discussed first. These will be followed by an overview of reacting gas-phase studies in turbulent flames. Finally, liquid-phase differential diffusion experiments will be reviewed.

Experimental investigations of differential diffusion have been performed since Bilger and Dibble (1982) suggested a Rayleigh scattering experiment to verify their numerical model of a hydrogen/propane jet. This proposed experiment was not conducted until 1989, due to experimental limitations, and was only recently reported (Dibble and Long 2005). In this Rayleigh scattering experiment of a non-reacting flow, differential diffusion was observed in jets of Freon/H_2 and CH_4/H_2 mixtures with Reynolds numbers extending up to 20000.

Long et al. (1993) investigated differential diffusion in jets seeded with both biacetyl and TiO_2 particles. They compared image pairs of the seeded tracers at two Reynolds numbers, 3300 and 10000. Due to experimental constraints, differential diffusion effects could not be quantified from their results. However, the results indicated the presence of these effects, as they reported differences in structures in images of the tracers. They also observed that differences in the images were more pronounced at the lower Reynolds number, implying a decrease in differential diffusion effects with increasing Reynolds number.

Measurements to determine differential diffusion in non-reacting turbulent jets have also been performed by Smith et al. (1995a). They conducted their experiments in jets of hydrogen/carbon dioxide with Reynolds numbers ranging from 1000 to 64000. Their results indicated that when studying average species concentrations, differential diffusion effects become negligible at Reynolds numbers above 1000. However, they reported that differential diffusion effects were significant with respect to instantaneous species concentrations up to their highest Reynolds number of 64000. They found the root mean-square of normalized mole fraction differences, z_{rms}, to decrease with

increasing Reynolds number. Although they found z_{rms} decreased, they were unable to determine a direct relationship between z_{rms} and Reynolds number.

Brownell and Su (2004) performed an experimental investigation of differential diffusion in a jet, containing a mixture of propane and helium, issuing into a co-flowing stream of air. This jet was operated at a Reynolds number of 1000, which resulted in an initially laminar flow that transitioned to a turbulent one around 8 jet diameters downstream of the exit. They obtained planar images which radially spanned 3 jet diameters from the centreline, and axially from either 3.6 to 11.3 or 7.6 to 15.3 jet diameters downstream of the jet exit. To quantify differential diffusion, they studied differences in mole fractions obtained from a Rayleigh scattering signal. For averaged quantities, they found that the turbulence suppressed differential diffusion, as it was only significant in the laminar region of the jet. However, they observed differential diffusion to be present in both the laminar and turbulent region when studying differences in instantaneous mole fractions.

Experimental studies of differential diffusion have also been conducted in turbulent flames, beginning with the work of Drake et al. (1986). They presented results from experiments of laminar, transitional, and turbulent hydrogen/air jet diffusion flames. Their data on measured mixture fractions differed from those obtained by an adiabatic thermodynamic equilibrium calculation. They attributed the differences to differential diffusion effects. It should be noted that they observed the differences, and hence differential diffusion effects, to be greatest in the laminar flame cases. In their turbulent flames with Reynolds numbers greater than 8500, they found differential diffusion to be unimportant.

Masri et al. (1992) conducted a study that focused on determining differential diffusion effects in turbulent flames. They performed experiments in turbulent flames of hydrogen/carbon dioxide up to Reynolds numbers of 30000. In this study, they also performed calculations of laminar flames of hydrogen/carbon dioxide. Their results implied that differential diffusion effects are less significant in turbulent flames than in laminar flames, consistent with the results of Drake et al. (1986). However, Masri et al. (1992) also noted that they were only able to obtain results for the major species, and that some of the minor species, such as H, may show significant differential diffusion effects.

Smith *et al.* (1995b) have also performed experiments to measure differential diffusion in turbulent flames. Their tests were conducted in turbulent jet flames of hydrogen/carbon dioxide with Reynolds numbers reaching 30000. To determine differential diffusion effects, they studied differences in species mixture fractions. At all Reynolds numbers and downstream locations, they observed significant differential diffusion effects, unlike the work of Drake *et al.* (1986) and Masri *et al.* (1992) who found differential diffusion effects to be insignificant at higher Reynolds numbers. Smith *et al.* (1995b) also noted that differential diffusion was greatest on the fuel rich side of the flame, where hydrogen was present.

Meier *et al.* (1996) performed experiments in turbulent jet diffusion flames consisting of H_2/N_2 issuing into air. They executed these trials in two jets at different velocities but similar Reynolds numbers of 9800 and 10000. Their results showed that differential diffusion is most prominent in the lower part of the flow near the flame root, consistent with the findings of Smith *et al.* (1995b).

Differential diffusion effects in diffusion flames of $CH_4/H_2/N_2$ have been studied by Bergmann *et al.* (1998). They conducted experiments in a turbulent $CH_4/H_2/N_2$ jet diffusion flame at a Reynolds number of 15200. When studying mixture fractions of the species, they determined that the largest differences occurred in the starting region of the flame. Again, this result is consistent with the previous work of Smith *et al.* (1995b) and Meier *et al.* (1996), and an indication that differential diffusion effects are greatest on the fuel side of the flame.

Liquid-phase flows have also been studied to determine differential diffusion effects. Saylor and Sreenivasan (1998) examined differential diffusion in a turbulent water jet, consisting of two passive scalars, issuing into a quiescent reservoir at a Reynolds number of 430. The scalars in this work had Schmidt numbers which ranged from 1200 to 77000. To quantify differential diffusion effects, they measured the root-mean-square of normalized concentration differences, Z_{rms}. They found $Z_{rms} = 0.11$ for scalars with a Schmidt number ratio of approximately 4 ($Sc_1 = 1200$ and $Sc_2 = 4400$) and $Z_{rms} = 0.31$ for a scalar Schmidt number ratio of approximately 18 ($Sc_1 = 4400$ and $Sc_2 = 77000$). These results imply that larger Schmidt number differences (and ratios) lead to increases in differential diffusion, as expected from theoretical considerations (see

section 3.1). They also reported instances in which the normalized concentration difference was nonzero for times larger than the Kolmogorov timescale - an indication that differential diffusion effects also persist at scales larger than the Kolmogorov scale.

Differential diffusion can occur in the oceanic mixed layer, where salt and temperature are transported. Jackson and Rehmann (2003) performed experiments by steadily stirring a tank which initially had linear, diffusively stable, temperature and salinity profiles. The stirring of the tank was accomplished with vertical rods and resulted in turbulent Reynolds numbers up to 1810. They were able to qualitatively observe differential diffusion by studying temperature-salinity diagrams. They also determined differential diffusion effects to be present for their flow when studying the mixing efficiency.

Chapter 3

Theoretical Considerations

3.1 Passive Scalar Transport

The flow in this work consisted of two passive scalars (fluorescent dyes) mixed in water. The evolution of a non-reacting passive scalar, transported by a flow, is governed by the advection-diffusion equation:

$$\frac{\partial C_\alpha}{\partial t} + u_i \frac{\partial C_\alpha}{\partial x_i} = D_\alpha \frac{\partial^2 C_\alpha}{\partial x_i \partial x_i} \tag{3.1}$$

where C_α is the concentration of species α, t is time, u_i is the velocity in the i-direction, x_i is the coordinate in the i-direction, and D_α is the molecular diffusivity of species α. (The Einstein summation convention is not applied to Greek indices). For this work, two advection-diffusion equations are necessary since there are two scalars (of differing molecular diffusivity). If the two scalars are subjected to the same velocity field and have identical initial and boundary conditions, then any difference in their evolution will solely be due to the difference in their molecular diffusivities (as can be seen from the above advection-diffusion equation).

In this study, a normalized concentration difference equation, derived from the two advection-diffusion equations, is used to quantify differential diffusion. The next step in developing this equation is, therefore, to appropriately non-dimensionalize the

advection-diffusion equation. For an axisymmetric turbulent jet, the non-dimensionalization results in:

$$\frac{\partial C_\alpha^*}{\partial t^*} + u_i^* \frac{\partial C_\alpha^*}{\partial x_i^*} = \frac{1}{Re\, Sc_\alpha} \frac{\partial^2 C_\alpha^*}{\partial x_i^* \partial x_i^*} \tag{3.2}$$

where $C^* = \dfrac{C}{C_0}$, $t^* = \dfrac{tu_0}{d}$, $u^* = \dfrac{u}{u_0}$, $Re = \dfrac{u_0 d}{\nu}$, $Sc_\alpha = \dfrac{\nu}{D_\alpha}$, $x_i^* = \dfrac{x_i}{d}$, and C_0 is the jet nozzle concentration. Again, there will be an equation for each scalar ($\alpha = 1$ and $\alpha = 2$). Subtracting the equation for scalar 2 from the equation for scalar 1 yields a normalized concentration difference equation:

$$\frac{\partial Z_n}{\partial t} = \frac{1}{Re\, Sc_1}\left[\frac{\partial^2 C_1^*}{\partial x_i^* \partial x_i^*} - \left(\frac{Sc_1}{Sc_2}\right)\frac{\partial^2 C_2^*}{\partial x_i^* \partial x_i^*} \right] + u_i^*\left(\frac{\partial C_2^*}{\partial x_i^*} - \frac{\partial C_1^*}{\partial x_i^*} \right) \tag{3.3}$$

where $Z_n = C_1^* - C_2^*$. It can be seen that differential diffusion effects, in a non-reacting flow, are dependent on the Reynolds and Schmidt numbers of the scalars. In this form of the governing equation for the normalized concentration difference, differential diffusion effects are dependent on the ratio of the Schmidt numbers of the two scalars and the Péclet number (ReSc). This equation can also be cast in the following form:

$$\frac{\partial Z_n}{\partial t} = \frac{1}{Re}\left[\frac{1}{Sc_1}\frac{\partial^2 C_1^*}{\partial x_i^* \partial x_i^*} - \frac{1}{Sc_2}\frac{\partial^2 C_2^*}{\partial x_i^* \partial x_i^*} \right] + u_i^*\left(\frac{\partial C_2^*}{\partial x_i^*} - \frac{\partial C_1^*}{\partial x_i^*} \right) . \tag{3.4}$$

The normalized concentration difference that is presented herein is defined to be:

$$Z \equiv \frac{C_1}{\langle C_1 \rangle} - \frac{C_2}{\langle C_2 \rangle} \tag{3.5}$$

where C_1 is the concentration of disodium fluorescein, $Sc_1 = 2000$ (Ware et al. 1983, Deusch and Dracos 2001, and Villermaux et al. 2001), and C_2 is the concentration of sulforhodamine 101, $Sc_2 = 5000$ (Saylor 1993). In the above definition, each species concentration is normalized by its average value at that point in the flow field. This definition is a slight variation from that employed to determine the difference in mixture fraction, typically used in gas-phase studies, which normalizes the difference by the nozzle concentration. However, it is the same as the definition utilized in the liquid-phase experiments of Saylor and Sreenivasan (1998), making a more direct comparison between their results and the present ones possible. Normalizing in this manner also

27

serves to eliminate potential differences in nozzle concentrations from different experiments, as this quantity was not measured.

3.2   Fluorescence Theory

This section is intended to give an overview of fluorescence theory. A more detailed description can be found in Guilbault (1973), on which the following discussion is based.

The fluorescence process begins when a molecule absorbs energy in the form of light. This absorption can be quantified by the following equation:

$$E = h\upsilon_a = \frac{hc_l}{\lambda_a}, \tag{3.6}$$

where E is the absorbed energy in Joules, h is Planck's constant (6.62×10^{-34} J-sec), υ_a is the frequency of the absorbed light, c_l is the speed of light, and λ_a is the wavelength of the absorbed light. Absorption of energy is rapid as it takes only on the order of 10^{-15} seconds. It is also species specific, as it depends on the structure of the particular molecule. When a molecule absorbs energy, it jumps from its ground state to a higher energy level, at which it is unstable. The molecule will subsequently return back to its ground state by releasing energy in the form of photons, a rapid process which generally takes nanoseconds. While at the higher energy level, some of the excess energy will be dissipated from collisions with other molecules. Therefore, the light that is emitted by the molecule will be at a longer wavelength than that of the absorbed light, known as the Stokes shift, since less energy is emitted in returning to the ground state. This shift, in the absorbed and emitted wavelengths, provides the opportunity to isolate the emitted fluorescence signal from the excitation source.

It is necessary to relate fluorescence emission to species concentration when using fluorescence as a means to measure the concentration. This relationship is described by the following equation:

$$F = \phi_f I_0 (1 - e^{-\beta bc}) \tag{3.7}$$

where F is the fluorescence intensity, ϕ_f is the quantum efficiency, I_0 is the radiant power, β is the molar absorptivity, b is the path length of the cell, and C is the species

concentration. When the species concentration is dilute, then the term $\beta b C$ is usually much less than one and the fluorescence intensity can be estimated as:

$$F = \phi_f I_0 \beta b C ,$$
(3.8)

simplifying by means of a series expansion. Therefore, for dilute concentrations and constant laser power, the fluorescence intensity can be approximated to be a linear function of species concentration. Outside of the linear range the fluorescence intensity usually continues to increase as the concentration increases, albeit at a slower rate than in the linear range. Under certain conditions, the fluorescence intensity will decrease with increasing concentration. Because of these effects, LIF experiments, including this one, generally operate in the linear range.

Chapter 4

Experimental Setup, Relation of Output Voltage to Species Concentration and Examination of Potential Sources of Error

4.1 Experimental Facility

The experiments herein were conducted in a 6 m by 1.5 m by 1 m glass tank in the Environmental Hydraulics Laboratory of the Department of Civil Engineering and Applied Mechanics at McGill University. The sides of the tank consisted of single panes of 1.905 cm thick tempered glass while the bottom consisted of a superposition of two 1.905 cm thick tempered glass panes, resulting in a total thickness of 3.81 cm. The top of the tank was open to the ambient air. All experiments were conducted in a windowless darkroom, which ensured that the background light during every experiment was negligible. In addition, the fluorescent dyes employed herein were sensitive to all sources of light and exposure to even normal room lighting could impact their emitted fluorescence. Therefore, the background lighting was turned off just prior to handling the dyes and remained in this state until the completion of each experiment. Thus, outside sources of light did not interfere with the detected fluorescence signal.

4.2 Experimental Flow Apparatus

The experimental setup employed in this work will be presented in this section. First, the background, or ambient flow conditions, will be discussed. This will be followed by a description of the jet components, including the jet itself, along with the equipment used to control the flow through the jet.

4.2.1 Background Conditions

Punctual LIF measurements were made in a turbulent jet at several Reynolds numbers. The jet issued into a background which consisted of either quiescent water or approximately homogeneous, isotropic turbulence with zero-mean flow. When experiments were conducted in the quiescent background, sufficient time was allotted, after the tank was filled, to ensure that the background was stagnant before measurements commenced.

A random jet array, similar to that of Variano *et al.* (2004), created approximately homogeneous, isotropic background turbulence with zero-mean flow in a 1.5 m by 1.7 m by 0.9 m section of the tank. The location of the array in the tank (1.7 m from the edge) was chosen to ensure that the entire cross section of the jet was always in the isotropic region of the turbulent background. Preliminary tests conducted at various positions revealed that the above location was sufficient. The array consisted of 6 rows and 10 columns of bilge pumps (Rule 25D, 500 GPH) aligned vertically in the tank, as depicted in Figure 4.1. The pumps were fastened to a 1 m by 1.5 m sheet of high density polyethylene. Each pump had an outlet diameter of 19 mm. Several components were attached to the outlet of each pump in order to change the direction of the flow and expand the outlet diameter, as shown in Figure 4.2. A polyvinyl chloride (PVC) elbow joint (Spears 1407-010), with a 19 mm insert fitting end and a 25.4 mm female threaded end, was connected to each pump outlet. Preliminary tests were conducted to visualize the flow out of the elbow joint by operating one of the bilge pumps with dyed fluid. These tests showed that the flow out of the elbow joint was not straight, but rather came out at an angle. Therefore, the flow was straightened by the addition of a PVC extension. A male adapter (Spears 436-132) was inserted into the elbow joint in order to transition to the PVC extension. The PVC extension was 6 inches (152.4 mm) long with an inner

31

diameter of 31.75 mm. Thus, the flow exited (and issued into the background) at the outlets of the PVC extensions. The flow entered each pump through a circumferential inlet that was located at its bottom, where it was fastened to the polyethylene sheet. The spacing of the pumps was uniform in the horizontal and vertical directions with a centre to centre distance, M, of 15 cm between the outlets of the PVC extensions. Reflective boundary conditions were chosen to reduce the possibility of any secondary motions, in analogy with oscillating grid turbulence (Fernando and De Silva 1993b and Variano et al. 2004). These boundary conditions resulted in the spacing from the centre of the outlets to the tank walls and free surface to be 7.5 cm.
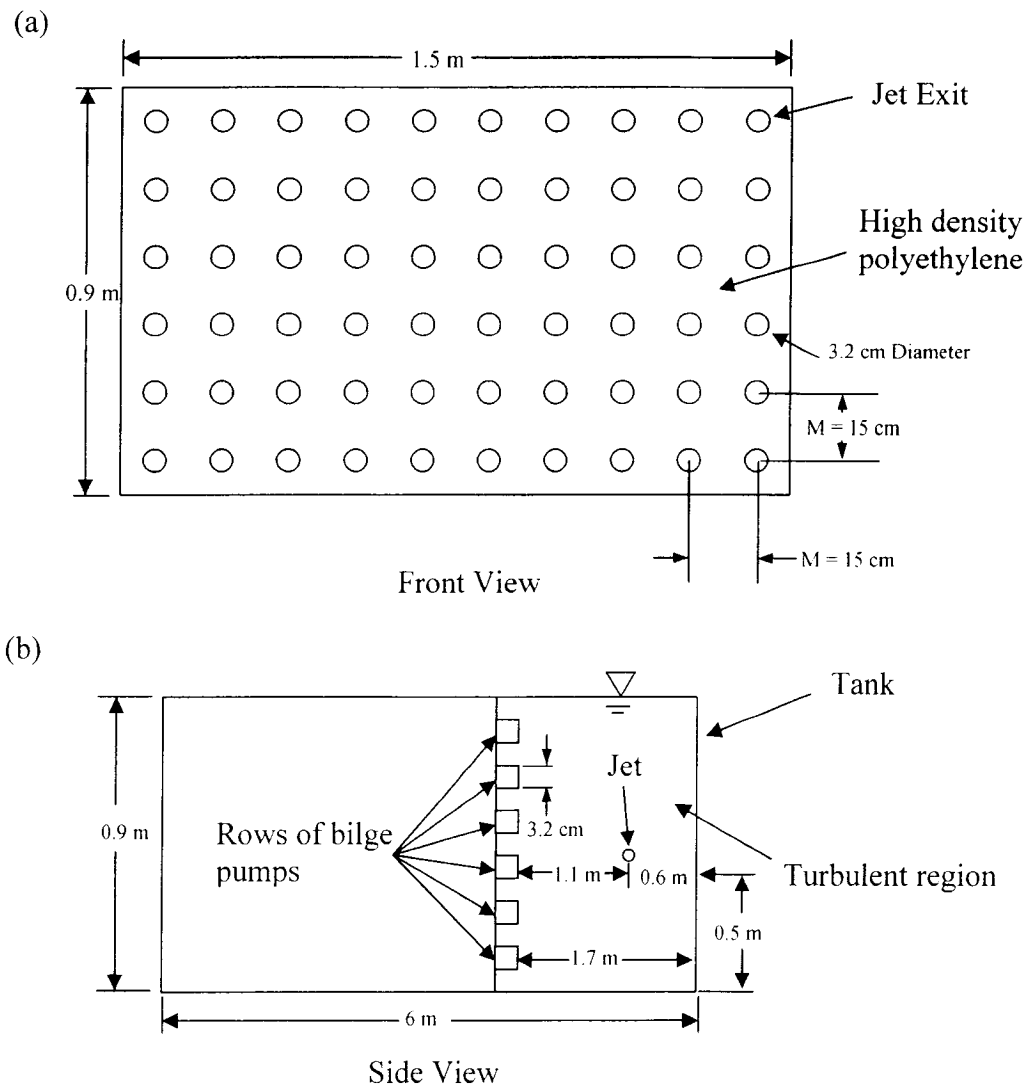
Figure 4.1: Random jet array schematic, (a) front view, (b) side view.

PVC Extension Outlet

PVC Extension

Male Adapter

Elbow Joint

Pump Outlet

Pump Inlet
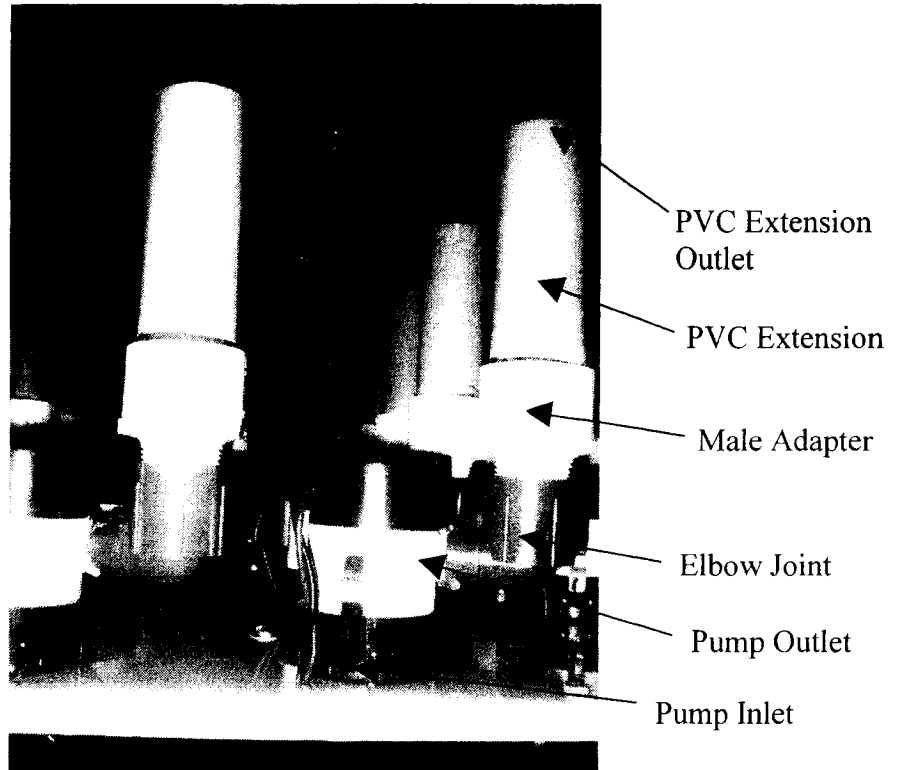
Figure 4.2: Photograph of bilge pumps and their attachments.

Each pump was independently and randomly turned on and off to create a quasi-isotropic turbulent field with zero-mean flow. This random control of the pumps diminished the possibility of developing secondary flows. A custom algorithm, programmed in LabVIEW, was used to operate each pump. The individual pumps were controlled in a manner similar to the method of Variano *et al.* (2004). Variano (private communication) has also tested various other algorithms in attempting to create the desired flow. He observed that the most ideal conditions (i.e., closest to isotropic turbulence with zero-mean flow) occurred when each pump was individually turned on at first, and then off, with the on and off time randomly selected from a prescribed normal distribution. In this scenario, an individual pump was first turned on for a random amount of time, determined from a normal distribution with an average on time, μ_{on}, and standard deviation, σ_{on}. Next, the pump was turned off for a random amount of time determined from a second normal distribution with an average off time, μ_{off}, and standard deviation, σ_{off}. Subsequently, the pump was continuously turned on and then off, with

the times assigned by the random normal distributions. Based on Variano's recommendation, several variations of this algorithm formulation were tested in the present study to obtain the best conditions for the given setup. These variations included attempting several average on times, average off times and standard deviations. The selected algorithm had an average on time of 12 seconds with a standard deviation of 4 seconds. The corresponding average off time was chosen to be 108 seconds with a standard deviation of 36 seconds. Thus, under these conditions, on average 10 % of the pumps were on at any given time. An alternate algorithm, in which each pump was again individually and randomly controlled, was also tested. In this case, the state of each pump, whether it was on or off, was determined by generating a separate random number, between 0 and 1, for each pump. If this random number was above a certain value, designated as the threshold, then the state of the pump was changed. The time between iterations, or generation of a new random number, was a user input (constant and the same for each pump throughout the execution of the algorithm). For this algorithm, the most ideal conditions occurred when the threshold was set to 0.98 with a time of 0.4 seconds between the generations of new random numbers. Hence, if a pump was initially on and the random number generated was greater than 0.98, then the pump would be turned off until another random number greater than 0.98 was generated. Of the two algorithms and various combinations of inputs tested for each, the above conditions for the random normal distribution of on and off times yielded a background flow that was closest to the desired isotropic turbulence with zero-mean flow (see section 5.2.2). Thus, all experiments with the turbulent jet issuing into a turbulent background were conducted when the pumps were controlled by this algorithm.

4.2.2 Turbulent Jet Setup

The jet setup consisted of a supply reservoir, constant head reservoir, and the jet components. A schematic is depicted in Figure 4.3. The main concern in the design of this setup was to ensure a constant flowrate throughout each experiment. Other concerns included being able to easily vary the Reynolds number, position, and diameter of the turbulent jet.
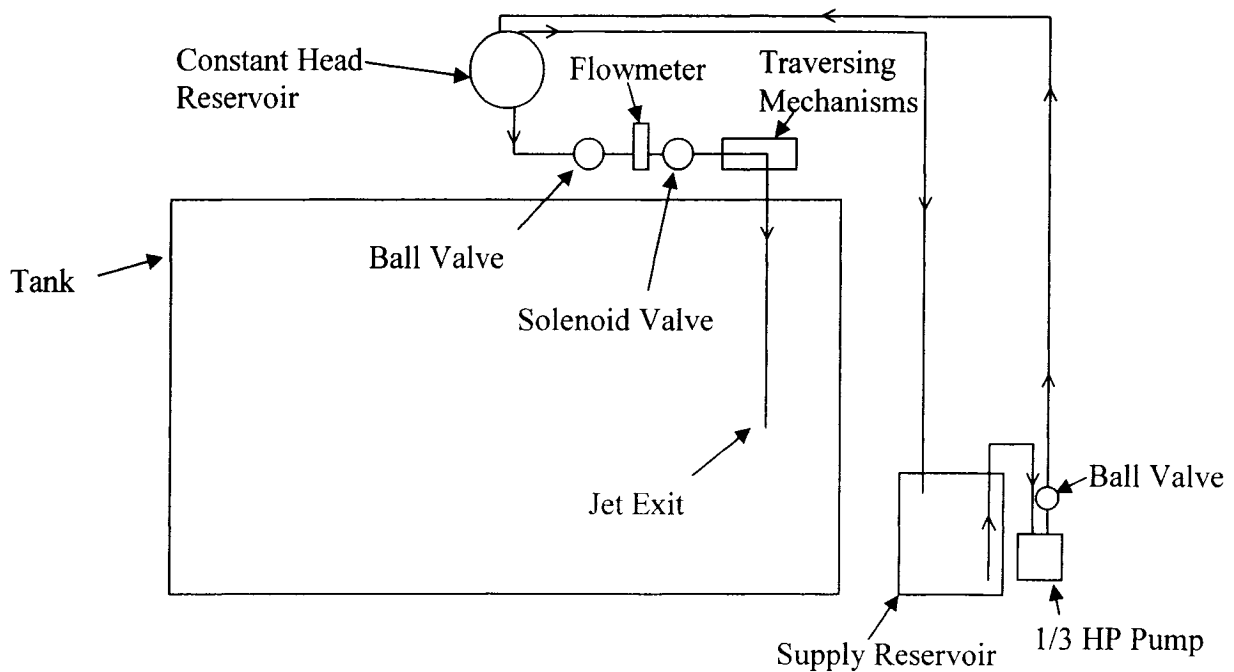
Figure 4.3: Schematic of the supply reservoir, constant head reservoir, and jet components.

The supply reservoir served three purposes. Firstly, it was used to thoroughly mix the fluorescent dyes before conducting an experiment. It then served to pump the dyed fluid up to the constant head reservoir during an experiment. Finally, it also acted as an overflow reservoir for excess dyed fluid that was pumped up to the constant head reservoir. This supply reservoir was an approximately 35 litre cylindrical glass container located at ground level next to the tank. During each experiment, jet fluid was continually pumped from the supply reservoir up to the constant head reservoir through 1.27 cm diameter PVC tubing via a 1/3 HP pump. A ball valve was connected in series with the pump, to control the flowrate up to the constant head reservoir. This ball valve was set such that the flowrate up to the constant head reservoir was slightly greater than the flowrate through the jet, thus ensuring a steady level in the constant head reservoir, as the excess dyed fluid flowed back to the supply reservoir (see below and Figure 4.3).

The constant head reservoir was used to create a pressure difference to drive the flow through the jet. This reservoir consisted of a 12 litre spherical glass container located 2 m above the jet exit. Jet fluid, pumped from the supply reservoir, entered the

constant head reservoir through an inlet at its top. An outlet leading back to the supply reservoir was located just below the inlet. This outlet served to maintain a steady level in the constant head reservoir as the excess jet fluid flowed through it and back to the supply reservoir through 1.905 cm diameter PVC tubing. A second outlet, located at the bottom of the constant head reservoir, connected the constant head reservoir to the jet components.

Upon exiting the constant head reservoir, the jet fluid flowed through 1.905 cm diameter PVC tubing towards a flowmeter (either an Omega FL50002A or a McMaster-Carr 8051K15). Two different flowmeters were utilized, due to the range of flowrates required to achieve the desired Reynolds number range. Therefore, they were mounted such that they could easily be interchanged. The flowmeter was located just above the upper surface of the tank (see Figure 4.3). Each flowmeter had a 1.27 cm inlet (and outlet) diameter. Therefore, the 1.905 cm diameter PVC tubing was contracted down to 1.27 cm diameter PVC tubing, with a reducer coupling, just prior to reaching the flowmeter. A ball valve was also located in series with and right before the flowmeter. The ball valve and flowmeter were used in tandem to set the flowrate to within 6 % of that required to achieve the desired Reynolds number. Once the ball valve was set at a particular Reynolds number, all the experiments at that Reynolds number were conducted before the valve was set to its next position. The flowrate was varied from 0.07 litres/min (corresponding to Re = 900 with a 1.6 mm diameter jet) to 4 litres/min (corresponding to Re = 10600 with an 8 mm diameter jet). A solenoid valve was also connected in series with the ball valve and flowmeter, along the tubing leading to the jet. This valve was positioned just past the flowmeter and was employed to control whether or not there was flow through the jet. When a voltage was supplied to it, the solenoid valve was open and there was flow through the jet. Conversely, when no voltage was supplied to this valve, it was closed and the flowrate through the jet was zero.

After passing through the solenoid valve, the flow was contracted again, down to 8 mm diameter copper tubing. This copper tubing was 0.62 m in length and attached to a traversing mechanism such that it extended vertically into the tank. It extended vertically downwards for 0.5 m at which point there was a 90° bend, such that the flow exited the tubing horizontally. The exact horizontal and vertical location of the exit of the jet was

controlled by the traversing mechanism (described below). After the 90° bend, the copper tubing extended horizontally for another 12 cm, at which point the flow either entered the tank or was contracted again. The copper tubing served as the jet nozzle for experiments performed with the 8 mm jet exit diameter. A 50.8 mm long stainless steel dispensing needle was connected to the end of the copper tubing for experiments conducted with either a 1.6 or 3.81 mm diameter jet. The 1.6 mm diameter needle corresponded to a 14 gauge needle (McMaster-Carr 6710A21) while the 3.81 mm diameter needle corresponded to a 7 gauge needle (McMaster-Carr 6710A13). When in place, these needles served as the jet exit.

There were slight differences in the initial jet conditions due to the various jet diameters. After the 90° bend in the copper tubing, the jet fluid passed through different pipe lengths before exiting the nozzle. However, the distinct initial conditions only affected the near-field of the jet and any asymmetries due to the bend were no longer present in the far-field, where measurements were obtained. Ferdman *et al.* (2000) showed that the statistics in the far-field were the same, to within experimental uncertainty, in their study that compared turbulent round jets that issued from a straight pipe to those issuing only a few jet diameters after a 90° bend. In each instance, they found that the mean velocities were self-similar by 15 jet diameters downstream of the nozzle and the turbulent intensities by 40 jet diameters. Ferdman *et al.* also observed the mean centreline axial velocities and normalized r.m.s. velocities to be identical in the far field. Since all measurements were taken at a downstream distance of 50 jet diameters from the exit in this work, the slight difference in initial conditions did not impact the results.

The fluid exiting the jet nozzle consisted of two fluorescent dyes, of unequal molecular diffusivities, thoroughly mixed in water at low concentrations. Dilute dye concentrations served several useful purposes; firstly, they ensured the emitted fluorescence was within the linear range. Secondly, dilute concentrations prevented any density differences, which could lead to inertial effects, between the dyed jet and ambient fluids. Utilizing dilute concentrations also limited the possibility of trapping, the absorption of fluorescence by one species that was emitted by another species (or the same species) at another location, and attenuation, the weakening of a laser beam along

its path as its energy is absorbed by a fluorescent tracer. Each of these effects could result in erroneously low fluorescent signals, negatively impacting the final results.

The two fluorescent dyes selected for these experiments were disodium fluorescein (Fisher Scientific) and sulforhodamine 101 (Biotium). These dyes were selected due to their differing Schmidt numbers and fluorescence characteristics. Recall that disodium fluorescein has a Schmidt number of 2000, while sulforhodamine 101 has a Schmidt number of 5000. The excitation and emission spectra of these dyes are depicted in Figure 4.4. The sulforhodamine 101 spectra were provided by the manufacturer while the disodium fluorescein spectra are from the measurements of Saylor and Sreenivasan (1998). The disodium fluorescein emission spectrum in this work should be slightly different than in Figure 4.4. Saylor and Sreenivasan (1998) used a 488 nm excitation source while in the present study the excitation source was 514.5 nm (see section 4.3). Therefore, the disodium fluorescein emission spectrum in this work most likely has the same form as that depicted in Figure 4.4, however, shifted to slightly higher wavelengths. Nonetheless, as shown in the calibration procedure (see section 4.6.1) this shift will not impact the results. As can be seen in Figure 4.4, there is an overlap in the excitation spectra of these species. Therefore, the same excitation source was used to simultaneously excite both dyes. While the overlap in the excitation spectra was beneficial, the corresponding overlap in the emission spectra was unwanted and potentially complicated the measurements. Due to this overlap, the fluorescent signal of the dyes needed to be properly filtered in order to distinguish one species from the other (see section 4.3).

(a) ——— Disodium fluorescein excitation
— — Sulforhodamine 101 excitation

(b) ——— Disodium fluorescein emission
— — Sulforhodamine 101 emission
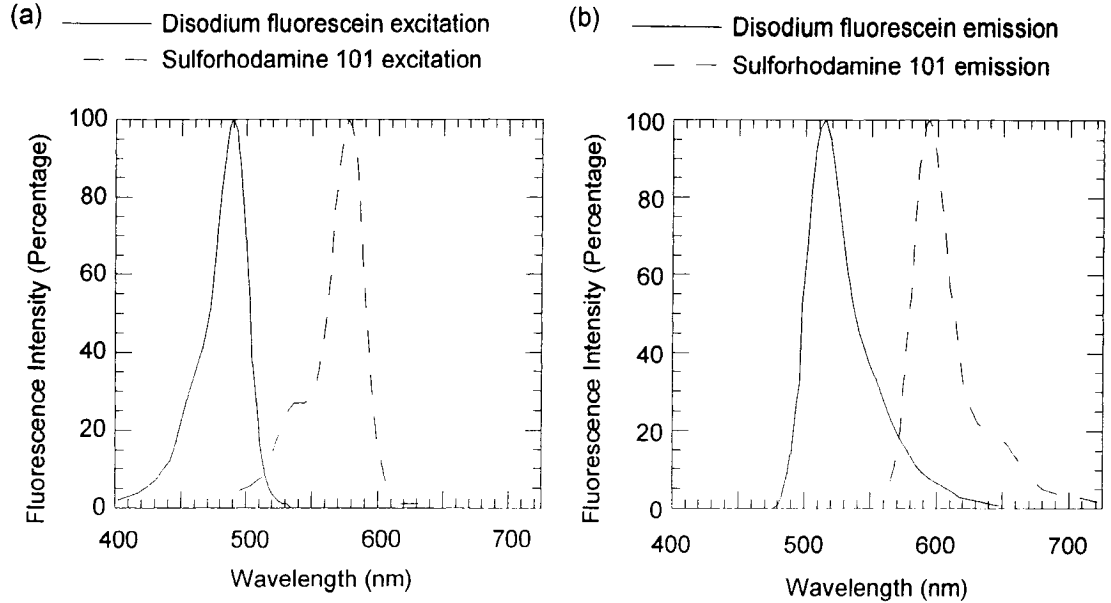
Figure 4.4: Disodium fluorescein and sulforhodamine 101 fluorescence spectra, (a) excitation spectra and (b) emission spectra.

At each Reynolds number, measurements were first made at the jet centreline and were then extended radially outwards until reaching the edge of the cross-section, providing results along a "radial slice". Since the optics were difficult to align, they were securely mounted (see section 4.3) and the jet was translated. A Velmex A25 series traversing mechanism was used to horizontally position the jet and move it in small increments from one experiment to the next. The resolution of this mechanism was 0.05 mm, more than adequate considering the smallest incremental step between experiments was 1 mm. The jet traversing mechanism allowed the jet to move a total of 24 cm in the horizontal direction, sufficient to cover the maximum jet diameter at the measurement location, 18 cm (with d = 8 mm). The maximum jet diameter was calculated using the following equation (White 2006):

$$D_j(x) = 2\left(x\tan 13°\right) \tag{4.1}$$

where x is the downstream distance from the jet exit. For every experiment, measurements were taken at a downstream distance of x/d = 50, thus x = 40 cm in the above estimate. This downstream location was chosen since it is in the self-similar region (for both mean and turbulent quantities) of the jet and meets the constraints imposed by the apparatus, see section 5.2.1.

The jet was aligned in both the horizontal and vertical to ensure that the measurements commenced at the centreline for each radial slice. A second traversing mechanism (Velmex A15 series) was used to vertically align the jet. This alignment was accomplished by first vertically traversing the cross-section of the jet in 0.5 cm increments while recording the average fluorescence signal at each location. For simplicity, the jet was operated with a single dye, disodium fluorescein, during these tests. An approximate vertical jet centreline was determined by the location of the maximum value of the average fluorescent signal (as the maximum average concentration occurs at the centreline). The jet was then positioned 1.5 cm above the approximate vertical centreline and moved vertically down a total of 3 cm, in 0.1 cm increments. These finer movements allowed for the determination of a more accurate vertical centreline position. This process was then repeated in the horizontal direction to finally yield the location of the jet centreline.

When measuring along each radial slice, the jet was moved in horizontal increments which varied from 0.1 to 1 cm. The increment depended on the Reynolds number, jet diameter and radial position in the cross-section. The non-dimensional horizontal increments (r/d) were nearly identical for each cross-section studied, allowing comparison of a given radial position at different Reynolds numbers. In each instance, the jet was moved away from the side of the tank from which the laser entered. Movement in this direction limited the amount of dyed fluid that the laser would pass through before arriving at the measurement location, thereby further minimizing laser attenuation. As previously stated, laser attenuation occurs when the dyed fluid absorbs energy from the laser beam. Thus, the intensity of the laser beam decreases as its energy is absorbed. This absorption was undesirable, since it could have resulted in a decrease in the fluorescent signal with position along the beam, even if the species concentrations were constant.

4.3 Optical Setup

The optical setup consisted of both laser focusing and signal detection equipment, which were separately mounted due to the overall size of the apparatus. A detailed

description of all the components is given below, along with the corresponding schematic diagram, which can be seen in Figure 4.5.
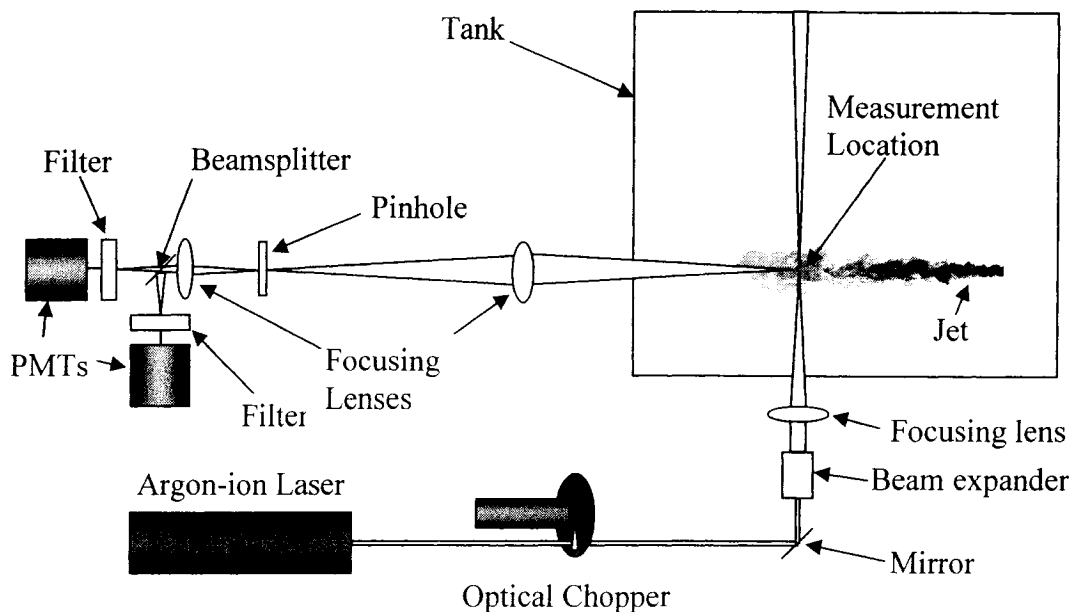
Figure 4.5: Schematic diagram of laser focusing and signal detection optics.

A focused laser beam from an argon-ion laser (Coherent Innova 90) was used to irradiate the fluorescent dyes and cause them to fluoresce at the measurement location. The laser was operated in light regulation mode, thus providing a long-term power stability of ± 0.5 % (provided by the manufacturer). It was also operated in single line mode, with a 514.5 nm beam issuing from it at an output power of 1.5 W. The output beam was Gaussian (TEM_{00}) with the aperture set to 3.97 mm. The laser output power was determined with a power meter (Coherent Lasermate 10) which gave readings with an accuracy of ± 5 %. The laser power was monitored before and after each experiment to verify that it remained constant throughout each test.

The laser beam first passed through a Scitec 310CD high speed optical chopper after exiting the laser. This chopper acted to pulse the laser, preventing any possible photobleaching or thermal blooming effects. It was operated with two five-slot discs, one on top of the other, which were offset at an angle. Therefore, the discs functioned to pulse the laser, as when they were rotated, the beam passed through an open slot for a

short period and was then blocked by the solid space between slots before passing through the next open slot. A schematic of laser pulses is depicted in Figure 4.6. In this figure, the step function indicates when the laser beam was passing through one of the open slots in the chopper discs. Both discs were 102 mm in diameter with open slots that each spanned 36°. The size of the pulse window could be varied since the two discs could be offset at different angles. The angle at which the chopper discs were offset was determined from the chopping frequency and combined photobleaching and thermal blooming time. The discs were always positioned such that the laser beam was permitted to pass through each open slot for 150 μs and then be blocked for the remainder of the pulse. Therefore, photobleaching and thermal blooming effects were negligible for these experiments, since the time for the signal from disodium fluorescein (which decays more rapidly due to photobleaching and thermal blooming than sulforhodamine 101) to decay by 2 % was 200 μs (see section 4.6.). The chopping frequency was set to ensure that, as a parcel of fluid was advected downstream, it would only reside in the measurement volume long enough to be irradiated by one laser pulse. This residence time was determined by dividing the diameter of the focused spot size (see below) by the mean centreline axial velocity at that particular measurement location (see section 5.2.1). The corresponding chopping frequency depended on both the Reynolds number and jet diameter and ranged from 650 Hz to 1600 Hz (see section 5.2.1). This chopping frequency also acted as the sampling frequency for the experiments. Therefore, it was also necessary to ensure that it was greater than the Kolmogorov frequency, in order to resolve this scale.

Chopping Frequency (650 – 1600 Hz. ie., 1540 – 625 μs)

150 μs
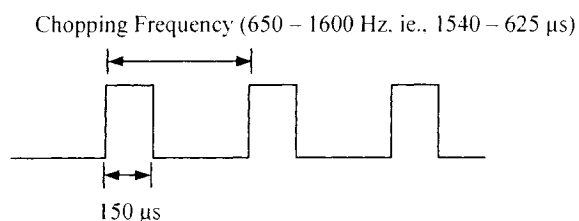
Figure 4.6: Schematic of typical laser pulses.

Upon exiting the chopper, the laser beam was directed towards a 3-times beam expander (Melles Griot 091BZ001). The output of the beam expander was a 12 mm

42

diameter collimated beam, which was then directed through a 1 m focal length plano-convex lens (Melles Griot 011PX347), placed 0.4 m from the edge of the tank. This lens focused the beam down to a waist diameter, or focused spot size, of 100 μm at the focal point. The focal point of this lens served as the measurement location and was located 0.6 m from the edge of the tank. The waist diameter was estimated by the following equation, given by Ready (1978):

$$d_0 = \frac{2.44 f_l \lambda_l}{D_b} \quad (4.2)$$

where d_0 is the focused diameter, f_l is the lens focal length, λ_l is the wavelength of the laser beam, and D_b is the diameter of the laser beam upon entering the focusing lens.

The signal collection optics were aligned perpendicular to the laser beam at the measurement location. This positioning ensured that the image at the focal point of the plano-convex laser focusing lens was focused onto the signal detection devices, see Figure 4.5. Most of the collection optics were secured along a 2 m long optical rail (Melles Griot 070RN011) to ensure they were aligned with each other. The remaining collection optics were located on a separate 0.25 m long optical rail (Melles Griot 070RN001) which was aligned perpendicular to the longer optical rail.

The first optical component, fixed onto the optical rail, was a 500 mm focal length achromat (Melles Griot 011A0346). An achromatic lens was chosen because it is a doublet lens, which exhibits fewer aberrations than a singlet, such as a plano-convex lens. Since focusing the image from the focused laser beam waist (i.e., the image at the measurement location) onto the collection optics was critical, an achromatic lens was chosen over a plano-convex lens. This achromat was positioned 1.0 m from the measurement location and 1.0 m in front of a 100 μm pinhole (Melles Griot 04PPM015), which was also secured on the optical rail. The size of the image from the measurement location that was focused onto the pinhole was given by the lens and magnification equations (i.e., Jenkins and White 1957, Rossi 1957):

$$\frac{1}{f_l} = \frac{1}{s} + \frac{1}{s''} \quad (4.3)$$

$$M_l = \frac{s''}{s} \quad (4.4)$$

43

where s is the object distance (1 m herein), s'' is the image distance (1 m herein), and M_i is the magnification. Therefore, the height of the image focused onto the pinhole was 100 μm, the same as the diameter of the image at the measurement location. The purpose of the pinhole was to ensure that the fluorescence signal reaching the collection optics (two PMTs) was only from a 100 μm length along the axis of the laser beam. This image was from a 100 μm section at the measurement location, since the size of the image reaching the pinhole had a one to one relationship with the size of the signal at the measurement volume. Therefore, since the image passing through the pinhole was from a 100 μm axial length, at the measurement location, and the diameter of the focused laser beam was also 100 μm, the resolution of the experiments was a maximum of 100 μm in all directions.

After passing through the pinhole, the image was then directed through a 60 mm focal length achromat (Melles Griot 011A0079), which was located 120 mm past the pinhole along the optical rail. Again, an achromatic lens was selected since it has fewer aberrations than a singlet. This lens was in place to refocus the image and limit its size as it reached each PMT. The next optical component after the achromat was a 50/50 plate beamsplitter (Melles Griot 03BTF023) that was placed 40 mm from the 60 mm focal length achromat, along the 2 m optical rail. The beamsplitter divided the signal such that half of it was simultaneously directed towards each PMT.

Two identical PMTs (Hamamatsu R928) were placed 80 mm from the beamsplitter to simultaneously detect the fluorescence signal. One of the PMTs was secured along the 2 m optical rail, while the other was fixed along the 0.25 m optical rail (which was secured perpendicular to the 2 m optical rail at the beamsplitter location). Each PMT was sheltered in an aluminum housing which served to prevent light from anywhere but the measurement location from reaching it. Both aluminum housings had a small circular hole, approximately 30 mm in diameter, which permitted the signal from the measurement location to pass through and be detected by the PMT.

Since the signal reaching the PMTs was from the emitted fluorescence of both fluorescent dyes as well as scattered laser light, separate filters were placed in front of each. These filters ensured that the fluorescence signal from only one scalar reached each PMT. A 645 nm color glass cut-off filter (Melles Griot 03FCG505) was placed in

front of the PMT fixed on the 0.25 m optical rail, designated as the sulforhodamine 101 PMT. Scattered laser light as well as the emitted fluorescence from disodium fluorescein was blocked by this filter, as can be seen in Figure 4.7. Therefore, only the fluorescence emitted by sulforhodamine 101 passed through this filter and reached the sulforhodamine 101 PMT. A band-pass filter with a 40 nm bandwidth centred at 550 nm (Andover Corporation 550FS40-25) was placed in front of the other PMT secured on the 2 m optical rail, designated as the disodium fluorescein PMT. This filter blocked any scattered laser light and the fluorescence emitted by sulforhodamine 101. Thus, only the fluorescence emitted by disodium fluorescein passed through this filter and reached the disodium fluorescein PMT, as shown in Figure 4.7.

The transmission characteristics of each PMT filter, provided by their respective manufacturers, along with the emission spectra of sulforhodamine 101 and disodium fluorescein are plotted in Figure 4.7. From this figure, it can be seen that a very small fraction of the fluorescence emitted by disodium fluorescein reached the sulforhodamine 101 PMT. Similarly, a small fraction of the fluorescence emitted by sulforhodamine 101 reached the disodium fluorescein PMT. However, in each instance, the emitted fluorescence of one dye that reached the designated PMT of the other dye (i.e., disodium fluorescein fluorescence detected by the sulforhodamine 101 PMT) was negligible. This will be discussed further in the overview of the calibration procedure, section 4.6.1.
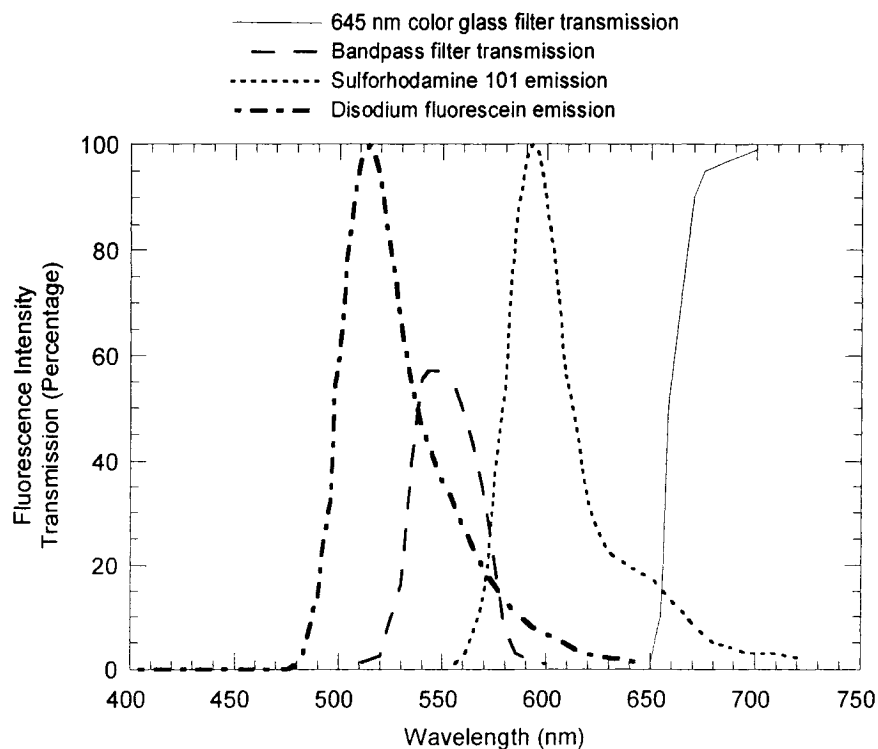
Figure 4.7: Transmission characteristics of the PMT filters, along with the emission spectra of disodium fluorescein and sulforhodamine 101.

4.4   Data Acquisition Components

The PMTs voltage supply was an Agilent triple output DC power supply (Model E3630A). The output signal of each PMT is related to its supply voltage by a power law. Therefore, it was necessary to select a power supply that could provide a constant voltage to the PMTs. The chosen power supply was able to meet this criterion as it provided the PMTs with a stable voltage with 0.01 % load regulation. The output of each PMT was a current which was sent through a cable towards a unity-gain operational amplifier. A 100 kΩ ± 5 % resistor was placed in parallel with each cable, just prior to the operational amplifier. These resistors were used to convert the signal from a current to a voltage, while also providing a gain. The frequency response of the PMTs was lowered due to the resistors, which can be calculated from the following equation (Hamamatsu 2006):

$$f_c = \frac{1}{2\pi RC_j},$$
(4.5)

where f_c is the cut-off frequency of the photodetector, R is the total resistance and C_j is the characteristic capacitance of the circuit. The total nominal capacitance of the circuit was 269 pF, as each PMT had a nominal characteristic capacitance of 20 pF while the capacitance of the cable was nominally 83 pF/m, and 3 m of cable were used. Thus, the frequency response of the PMTs was estimated to be 5900 Hz, which granted a sufficiently high frequency response while still providing enough gain to detect the fluorescence signal. After the resistors, the signal was sent through a unity-gain operational amplifier (National Semiconductor LM 747) before reaching a data acquisition board (National Instruments PCI-MIO-16E-4). The circuit for each operational amplifier is depicted in Figure 4.8. The unity-gain operational amplifiers reduced the current to the data acquisition board while maintaining the same voltage. This reduction in current was necessary to prevent crosstalk between the channels on the data acquisition board, which was present when sampling at a rate greater than 10 kHz (which was the case as data was sampled at 83333Hz).
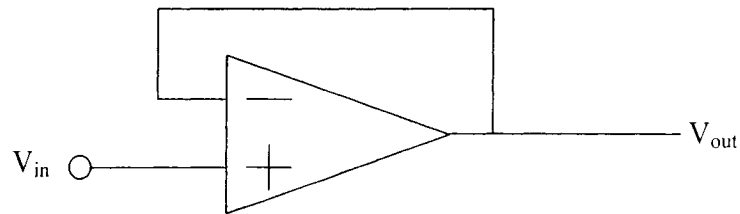
Figure 4.8: Unity-gain operational amplifier circuit.

4.5 Signal Processing

The analog signal from the PMTs was converted into digital data by the data acquisition board. This data acquisition board was a 12-bit board which divided the sampling window into 2^{12} discreet values. Therefore, each signal was truncated to its nearest value in the window. The sampling window was set to ± 5 V for each experiment, spanning the entire range of acquired voltages. Data acquisition through the board was controlled by a custom made program written in LabVIEW. Three channels of the data acquisition board were utilized; channels 1 and 2 were used to obtain the signals from the disodium fluorescein and sulforhodamine 101 PMTs, respectively, while channel 3 collected a signal from the optical chopper.

47

During each experiment, 40 separate blocks of data were collected at a frequency of 83333 Hz per channel. This frequency was chosen to maximize the 250 kHz sampling capability of the data acquisition board. The length of each block was either 262144 or 524288 samples per channel, depending on the chopping frequency of the optical chopper. Such large blocks of data were required given that the data was continually acquired both when the laser beam was passing through the optical chopper and when the beam was blocked by the chopper. The effective sampling frequency was determined by the optical chopper, with each laser pulse corresponding to one data point. Therefore, these large initial blocks of data were necessary to obtain final blocks of data that were (the desired length of) 4096 samples (per channel) per block for subsequent processing.

As mentioned above, every long block of data needed to be processed down to final block lengths of 4096 samples. The signal on channel 3 was from a photodetector, located on the optical chopper, which sent either i) a 5 V signal to the data acquisition board when the beam passed through the chopper, or ii) a 0 V signal when the beam was blocked. Each time the beam passed through a slot on the chopper discs, the corresponding signal from each channel (1 and 2) was averaged over the time of the passage. However, the corresponding signals from channels 1 and 2 were discarded when the beam was blocked. Thus, each pulse contained points when the laser was only partially blocked by the discs as it entered (or exited) the slotted region of the disc in the optical chopper. The points corresponding to fluorescence emitted when the laser was partially blocked were discarded and averaging only occurred when the laser beam fully passed through the optical chopper, see the schematic in Figure 4.9. Figure 4.10 shows a section of 15 laser pulses from a block of data from channel 1 before and after processing. (The method for processing channel 2 data was the same and therefore not shown here.) The plot in Figure 4.10(a) is of the unprocessed data and includes the portions where the laser beam was blocked by the optical chopper. The plot in Figure 4.10(b) is of the corresponding average of the peak (or completely unblocked portion) of each laser pulse. Therefore, the final processed block contained data points which represented one laser pulse. This processing also has the beneficial property of acting as a low-pass filter on the data.

48
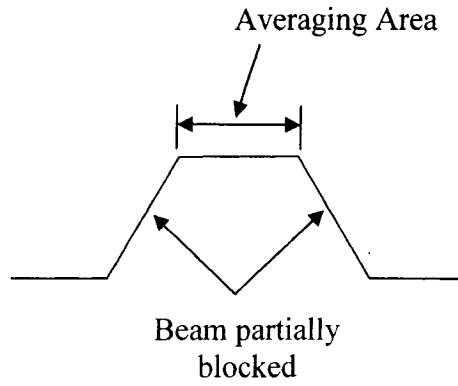
Figure 4.9: Schematic of characteristic form of pulsed fluorescence signal.
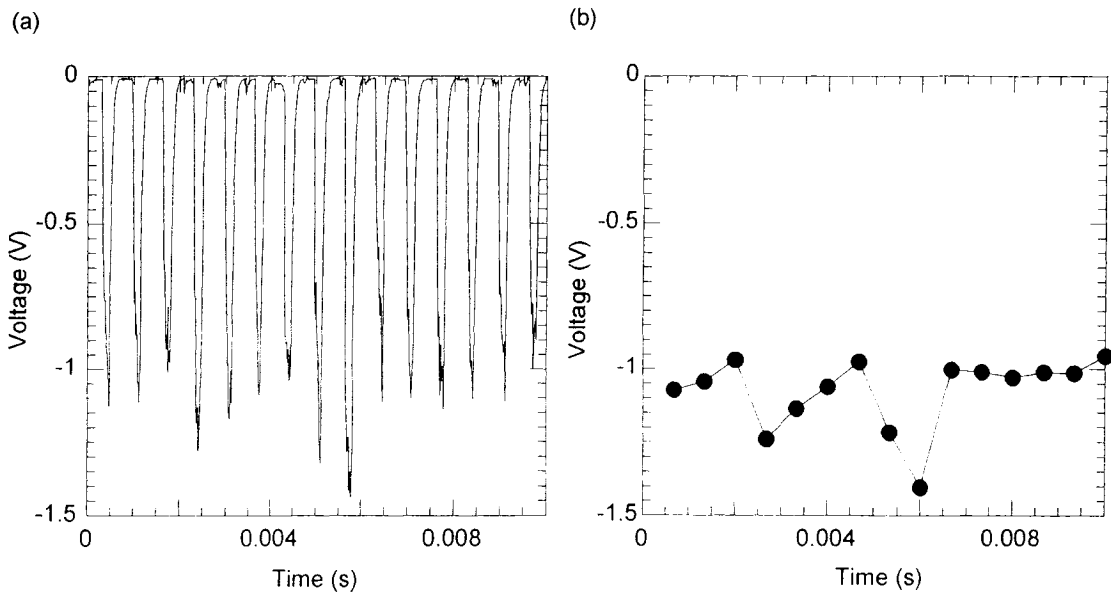
Figure 4.10: Time series of (a) unprocessed and (b) processed data.

The data was then further processed to filter out noise caused by amplification in the PMTs. An optimal Wiener filter (Wiener 1949) was applied to digitally filter the signal. This process is discussed in more detail in section 4.6.2.

4.6 Relation of Detected Fluorescence Signals to Species Concentrations

This section will describe the steps in relating the output voltage of the PMTs to individual species concentrations. Firstly, the calibration procedure, which directly

related the measured signal to the individual species concentrations, will be discussed. This will be followed by a review of the application of an optimal Wiener filter to improve the SNR.

4.6.1 Calibration Procedure

Multiple calibration procedures were extensively studied to relate the voltage output of the PMTs to the species concentrations of the individual fluorescent dyes. At low species concentrations, the fluorescence signal from a fluorescent dye can be linearly related to its concentration, as shown in section 3.2. That being said, calibrations were still necessary since two fluorescent tracers were simultaneously being measured. Ideally, each PMT would have only detected the emitted fluorescence of a single species. However, the overlap in the emission spectra of the two fluorescent dyes (see Figure 4.4) meant that a slight amount of the emitted fluorescence from each dye was detected by the PMT designated for detection of the other dye. Therefore, calibrations were performed to determine the magnitude of the overlap for a given concentration.

A calibration box was designed specifically for the calibrations. It was 30.5 cm by 76.2 cm by 51 cm, with each side consisting of a 6.35 mm thick panel of tempered glass. The bottom of the calibration box consisted of a sheet of 2.54 cm thick plexiglass, while the top was open to the ambient. The calibration box was placed inside of the large tank (see Figure 4.11) for the calibrations and, thus, served to minimize both the amount of dye necessary to complete a calibration and any possible trapping or attenuation effects. It was also placed on plexiglass supports to raise its height in the tank and further minimize the amount of necessary dye. The jet was placed inside the calibration box and the fluid (of known concentrations) in the calibration box was cycled through the jet so as to closely reproduce experimental conditions. An outlet was located at the bottom of the calibration box, with 1.27 cm diameter PVC tubing connected to it. This tubing was also connected to the 1/3 HP pump which led up to the constant head reservoir. Thus, the fluid in the calibration box could be cycled through the jet during the calibrations.

50

(a)

(b)
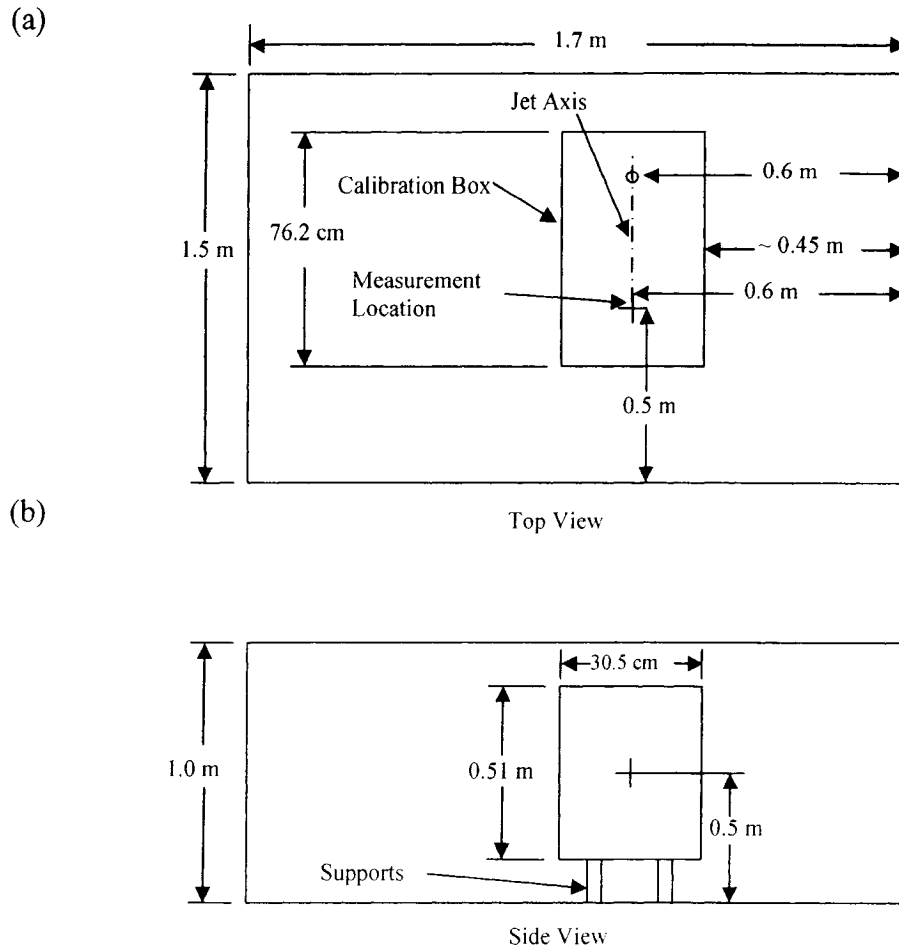
Figure 4.11: Orientation of the calibration box inside the tank,
(a) top view, (b) side view. Not to scale.

The first calibrations were performed with just one of the two selected fluorescent dyes, either disodium fluorescein or sulforhodamine 101. Each calibration consisted of detecting the fluorescence signal from progressively higher (known) concentrations of dye in the calibration box. The linear relationships between output voltage and concentration, for each fluorescent dye, can be seen in Figure 4.12. These calibrations verified that the concentrations were dilute enough such that the relationship between the detected fluorescence intensity and concentration was linear. The output voltages during these calibrations spanned the detected voltage range of the experiments. Therefore, the linear relationship obtained in these calibrations verified that the concentration of each fluorescent dye during the experiments was dilute enough to be in the desired linear range.

(a)

y = -0.0046454 - 6.4811e+07x R^2= 0.99915

(b)

y = -0.047427 - 1.4564e+07x R^2= 0.99853
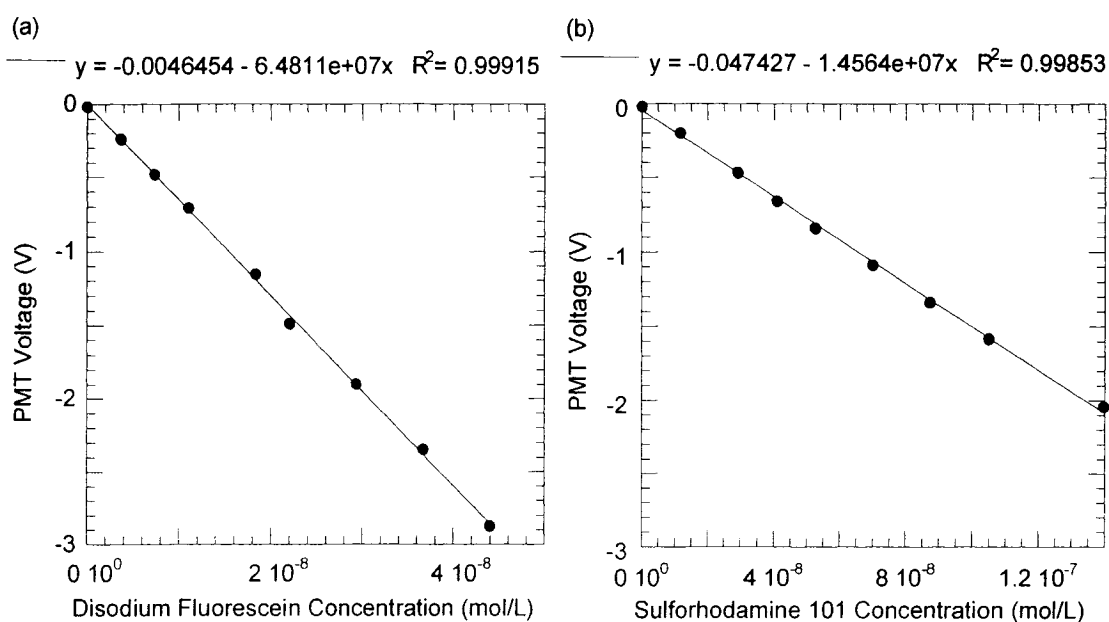
Figure 4.12: Linear calibration curves for (a) disodium fluorescein and (b) sulforhodamine 101.

After the single dye calibrations, a new set of calibrations were conducted in which combinations of the two dyes were simultaneously measured. The purpose of these calibrations was to quantify the detected signal from one dye obtained by the PMT designated to detect the other dye (or "optical crosstalk"). From these results, it was also possible to determine if a simple linear relationship relating the output voltage of one PMT to its respective species concentration would be adequate, or if a more complicated expression relating the output voltage of both PMTs to each species concentration would be necessary.

The "two-dye calibrations" were performed similarly to the single dye calibrations, except that a known concentration of one fluorescent dye was present while the concentration of the other was progressively increased. These "two-dye calibrations" commenced by measuring the signal from a known concentration of one of the fluorescent dyes. Next, a known concentration of the other dye was added and the fluorescence signal from the combination of the two dyes was detected. Known concentrations of the second dye were incrementally added and the fluorescence signal was subsequently detected. This process was repeated by varying the concentration of

the dye that was held constant while increasing the concentration of the other dye. The concentration of the dye being held constant was such that the resulting output voltage of the designated PMT was within the voltage range observed during actual experiments. The entire voltage range was spanned by performing multiple calibrations at various constant concentrations of this dye. Similarly, the concentration of the fluorescent dye that was incrementally increased was such that the output voltage of the PMT designated for detection of that respective dye spanned the range observed during actual experiments. The entire process was performed while holding sulforhodamine 101 constant and adding disodium fluorescein, and then again by holding disodium fluorescein constant and increasing the concentration of sulforhodamine 101.

Two voltages, one from each PMT, were acquired for each combination of dye concentrations. Curve fits of this data were obtained from the curve fitting software TableCurve 3D. The curve fits obtained, which related dye concentration to voltage, included a polynomial fit, a planar fit, a planar plus a constant fit, a linear fit, and a fit where species concentration was proportional to the output voltage. The formulae of these curve fits were as follows:

Polynomial:

$$F_{cf} = A + BV_1 + GV_2 + HV_1^2 + IV_2^2 + JV_1V_2 + KV_1^3 + LV_2^3 + NV_1V_2^2 + PV_1^2V_2 \qquad (4.6)$$

Planar: $F_{cf} = AV_1 + BV_2$ \qquad (4.7)

Planar constant: $F_{cf} = A + BV_1 + GV_2$ \qquad (4.8)

Linear: $F_{cf} = AV_1 + B$ \qquad (4.9)

Proportional: $F_{cf} = AV_1$ \qquad (4.10)

where F_{cf} is the species concentration (of either disodium fluorescein or sulforhodamine 101), V_1 and V_2 are the voltage outputs of the PMTs (either the disodium fluorescein PMT or sulforhodamine 101 PMT, depending on the particular species), and A, B, G, H, I, J, K, L, N, and P are all constants. These curve fits were then compared by analyzing data from different experiments, all conducted at a Reynolds number of 10600. These experiments included single-dye tests in which the jet fluid consisted of either sulforhodamine 101 or disodium fluorescein and also a two-dye test in which the jet fluid consisted of a mixture of both fluorescent dyes. Spectra, moments, and PDFs of the data

obtained from the different curve fits were compared to determine the best choice. The guiding principle was that the single-dye statistics should be the same, regardless if they are from a single-dye or two-dye experiment. The results were all very similar, regardless of the applied curve fit, since each curve fit was strongly dependent on only the PMT output voltage from the emitted fluorescence of one dye. Figure 4.13 compares disodium fluorescein spectra, $E_{c_1}(f)$, when using different curve fits, with the spectra in Figure 4.13(a) for single-dye experiments and the spectra in Figure 4.13(b) for two-dye experiments. Disodium fluorescein spectra are compared again in Figure 4.14, where the spectra are from applying the proportional curve fit to data from a single-dye and a two-dye experiment. Regardless of the chosen curve fit, all the spectra collapsed on each other. Similar results were observed (i.e., a collapse of the spectra) when comparing sulforhodamine 101 spectra (not shown). The only noticeable difference occurs in the PDFs of the polynomial curve fit. Figure 4.15 shows a comparison of PDFs of disodium fluorescein when applying the polynomial curve fit from a signal-dye test of disodium fluorescein to one with both dyes. The polynomial curve fit was discarded due to the discrepancy in the results of the PDFs, which can be seen in the figure, when there are large positive fluctuations of disodium fluorescein. This discrepancy in PDFs was not observed with the other curve fits, as can be observed for the proportional curve fit in Figure 4.16. Figure 4.16(a) displays the collapse of the PDFs of disodium fluorescein from single and two-dye tests while Figure 4.16(b) displays the collapse of the PDFs of sulforhodamine 101 from single and two-dye tests.

(a)   (b)

Ec$_1$(f) - Proportional Fit   Ec$_1$(f) - Proportional Fit
Ec$_1$(f) - Polynomial Fit   Ec$_1$(f) - Polynomial Fit
Ec$_1$(f) - Planar plus Constant Fit   Ec$_1$(f) - Planar plus Constant Fit
Ec$_1$(f) - Planar Fit   Ec$_1$(f) - Planar Fit
Ec$_1$(f) - Linear Fit   Ec$_1$(f) - Linear Fit
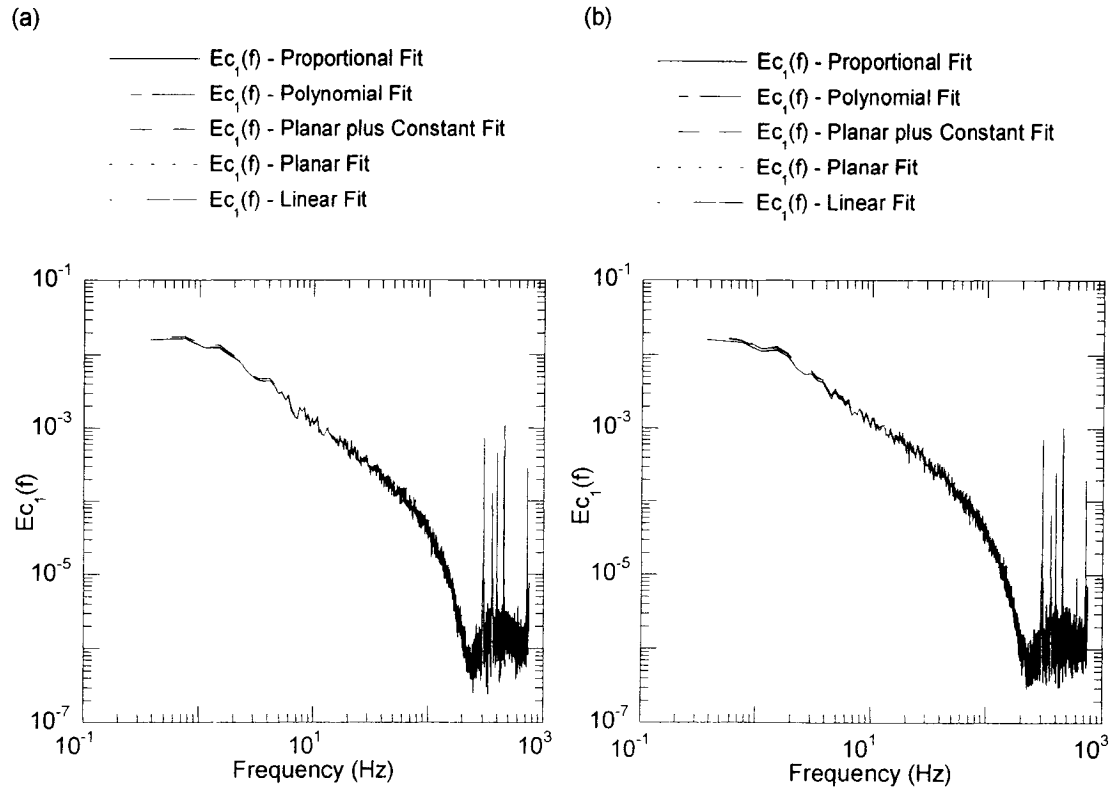
Figure 4.13: Comparison of centreline disodium fluorescein spectra, Ec$_1$(f), for all tested curve fits for a jet at Re = 10600. (a) Single-dye test (b) Two-dye test.

Ec$_1$(f) - two-dye experiment
Ec$_1$(f) - single-dye experiment
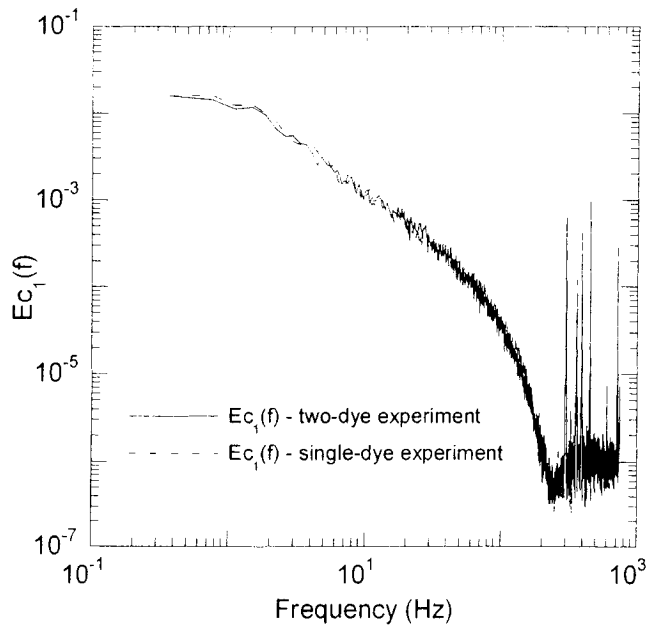
Figure 4.14: Comparison of centreline disodium fluorescein spectra, Ec$_1$(f), for single and two-dye experiments at Re = 10600 when applying a proportional curve fit.

55
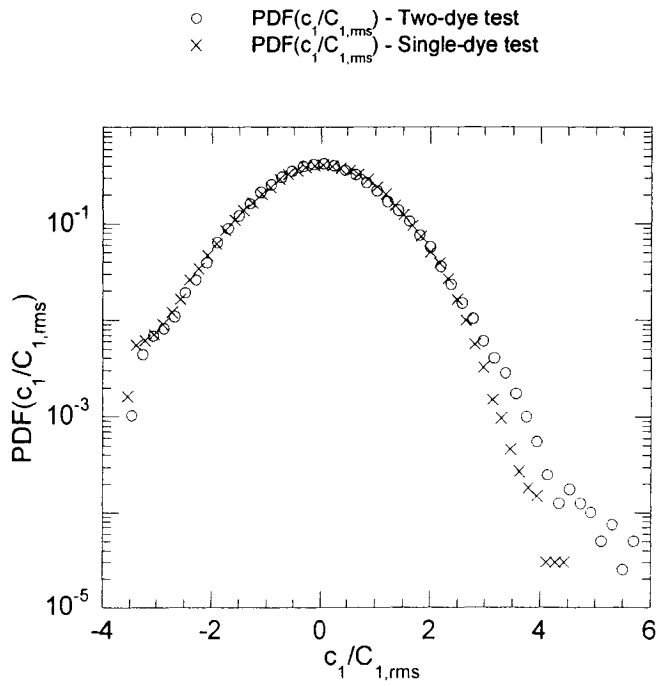
Figure 4.15: Comparison of centreline disodium fluorescein PDFs for single and two-dye experiments at Re = 10600 when applying a polynomial curve fit.
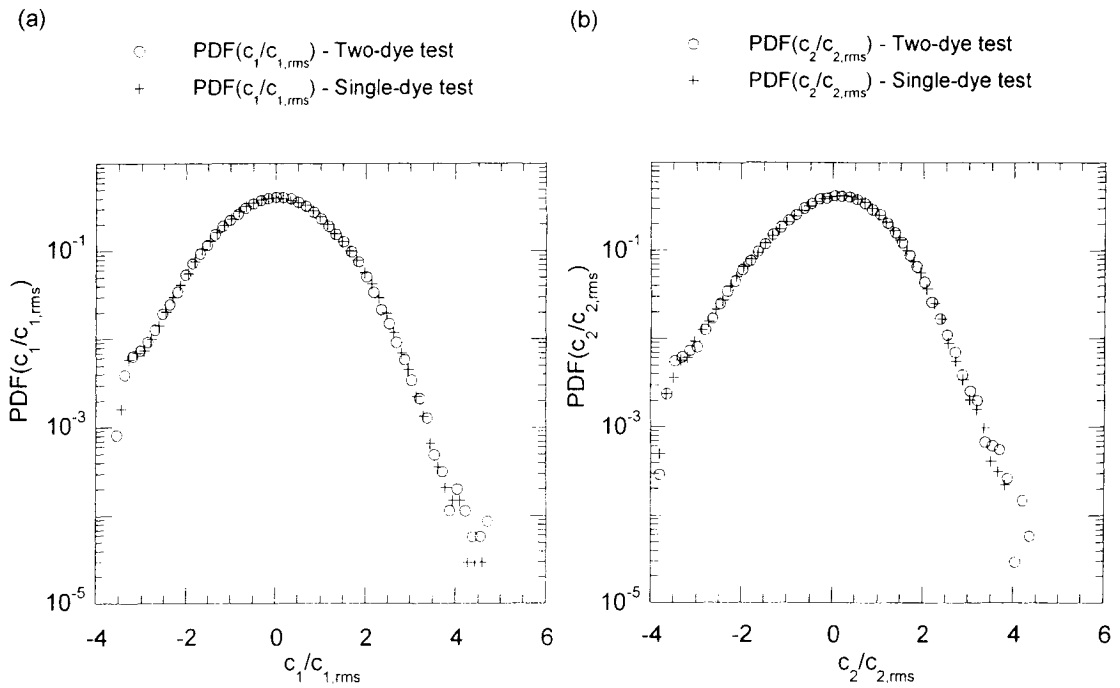
Figure 4.16: Individual scalar PDF comparison of single and two-dye experiments conducted at the centreline at Re = 10600. (a) Disodium fluorescein and (b) sulforhodamine 101.

56

Given that all other curve fits yielded similar results, the proportional curve fit was finally selected for simplicity's sake. In essence, this is a linear curve fit with zero offset (as should theoretically be the case – as zero species concentration should produce a PMT output of 0 V). However, since all concentrations were normalized during the analysis, the coefficient in front of the voltage was irrelevant and could be assumed to be 1. A planar or linear curve fit yielded the same results as the proportional curve fit; however, they were more expensive to compute and were therefore not selected. Choosing to directly relate the voltage output to dye concentration also negated the need to redo the calibrations at different times to account for effects such as differing water temperature or variances in the pH of the water. These effects could have had an impact on the fluorescence emission of the dyes.

4.6.2 Optimal Filtering

An optimal Wiener filter (Wiener 1949) was applied to the data to reduce noise caused by amplification in the PMTs. A Wiener filter is a digital filter that is applied in the Fourier domain with the goal of returning a calculated signal that is as close to the real signal, minus noise, as possible through a least squares method.

The technique used herein is similar to that of Miller (1991) and Dowling (1988) and follows the steps as laid out in Press *et al.* (1992). To apply this filter, the data was first Fourier transformed and the subsequent power spectrum was calculated. A necessary condition was that the data needed to be oversampled, so that there was a noise floor in the power spectrum. Next, a smooth curve was fit to the power spectrum curve and the noise floor was extrapolated over all frequencies, $N(f)$. This extrapolated noise floor was then subtracted from the measured spectrum to create a new, "noise-free" power spectrum, $S(f)$. Together the noise spectrum and "noise-free" spectrum yielded the optimal filter (Press *et al.* 1992), $\theta(f)$:

$$\theta(f) = \frac{|S(f)|^2}{|S(f)|^2 + |N(f)|^2}.$$
(4.11)

This optimal filter was then applied to the data in the Fourier domain before its inverse transform was taken to convert it back into the time domain. An example of the results

of the Wiener filter is depicted in Figure 4.17, where the spectra for an individual species concentration (of disodium fluorescein), $Ec_1(f)$, before and after filtering are compared. The increased SNR at high frequencies, due to the filtering, can be clearly seen in the figure.
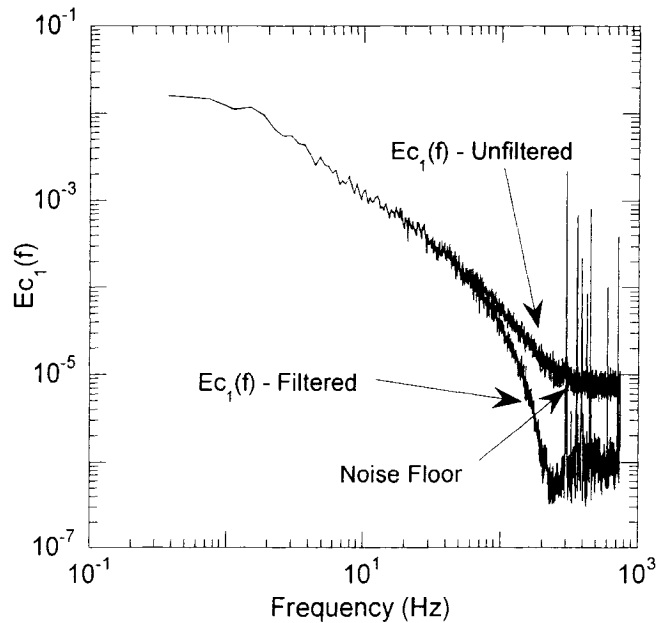
Figure 4.17: Comparison of disodium fluorescein spectra, $Ec_1(f)$, at Re = 10600 for filtered and unfiltered data.

4.7 Examination of Potential Sources of Error

This section describes the measures that were taken to ensure that the acquired signals were free of several possible error sources. A number of influences could have had an impact on the final results. These include inertial effects, photobleaching, and attenuation. If present, these factors could have led to inaccurate results pertaining to differential diffusion. Therefore, several tests were conducted to verify that these and other effects were minimal.

4.7.1 Photobleaching and Thermal Blooming

A procedure was developed to simultaneously quantify photobleaching and thermal blooming effects. Photobleaching can have an effect on the detected signal as

the fluorescence emitted by a fluorescent dye will decrease under constant laser irradiation. Thermal blooming can occur if the dyed fluid absorbs energy from the laser beam, causing an increase in its temperature. This temperature increase can lead to density differences in the fluid and also possibly cause refraction gradients which will affect the fluorescence signal (Koochesfahani 1984). Therefore, a small volume of dyed fluid was irradiated with a constant laser source to determine the time for combined photobleaching and thermal blooming effects to become significant. This technique was similar to that employed by Saylor (1993, 1995).

To perform the combined photobleaching and thermal blooming test, the calibration box (which was inside the large tank) and the large tank were both filled with water. Then, one of the fluorescent dyes (disodium fluorescein or sulforhodamine 101) was mixed into the calibration box.

Once the thoroughly mixed dyed fluid came to rest, it was irradiated with the laser. The laser was operated at a constant power of 1.5 W, the same power as that when conducting a turbulent jet experiment. Sampling of the fluorescence signal commenced before the laser shutter was opened, which ensured that the initial fluorescence signal was captured. The time series of the fluorescent signal was then analyzed to determine the time for its degradation.

Both disodium fluorescein and sulforhodamine 101 were tested to determine the combined photobleaching and thermal blooming time. Each test was conducted at species concentrations within their respective range, at the measurement location, during experiments. The fluorescent signal from disodium fluorescein was found to decrease by 2 %, from its peak value, in 200 μs. This can be seen in Figure 4.18 which shows the normalized voltage of the fluorescent signal from a photobleaching and thermal blooming test of disodium fluorescein. In this figure, a smooth fit was applied to the data (to account for noise in the detected signal) and the output voltage was normalized by its peak value. The plot in Figure 4.18(a) is for the entire time series while the plot in Figure 4.18(b) is for a selected portion, corresponding to the peak of the signal. The initial increase in voltage is from the time period when the laser shutter was being opened, and the laser beam was partially blocked. Therefore, the peak corresponds to when the shutter was (initially) fully opened and the laser beam was no longer blocked.

59
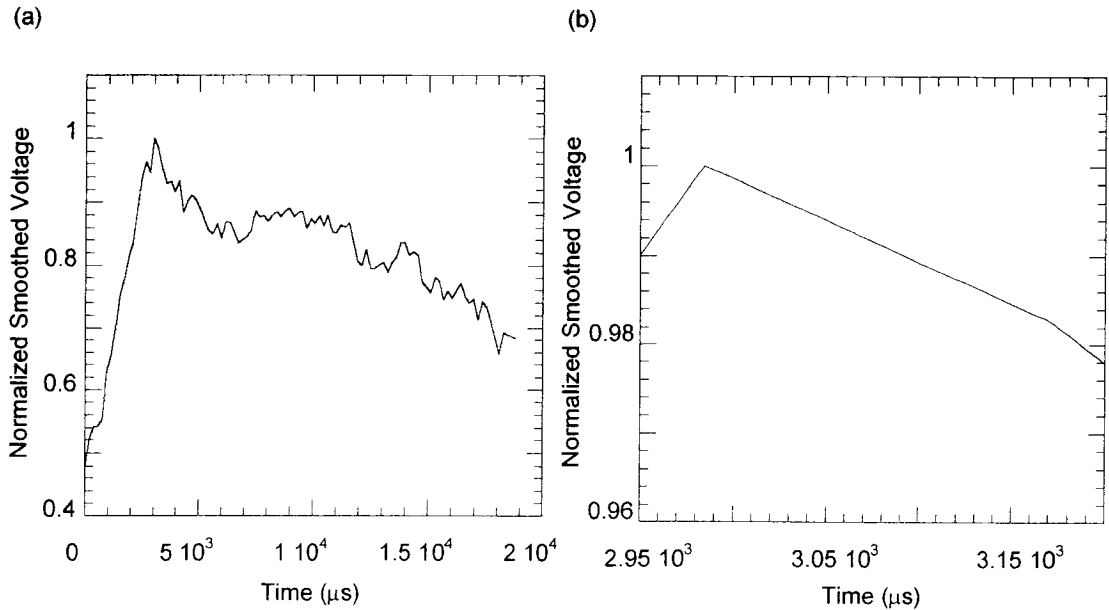
Figure 4.18: Normalized time series of disodium fluorescein voltage to determine the photobleaching and thermal blooming time. (a) Full time series. (b) Selected portion of the full time series.

Sulforhodamine 101 displayed minimal photobleaching and thermal blooming effects as the fluorescent signal decreased by 2 % from its peak in approximately 1500 μs (not shown). Therefore, the photobleaching and thermal blooming time of disodium fluorescein was of greater concern. For all experiments, the laser was pulsed with the optical chopper such that any parcel of fluid would only be subject to laser irradiation for 150 μs. This time was chosen since it is less than the 200 μs it takes for disodium fluorescein to degrade by 2%. Therefore, photobleaching and thermal blooming effects had a minimal effect on the detected fluorescence signals obtained in this work. Saylor (1993) deemed the 10 % signal degradation, in 150 μs, that he observed under his experimental conditions to be an acceptable level. The 2 % signal degradation found under these conditions was significantly less. Furthermore, the fluid in this test was stationary, whereas it is moving during the actual experiments, which served to further minimize photobleaching and thermal blooming effects.

4.7.2 Trapping

Trapping occurs when the fluorescence emitted by one species is absorbed by another species. This was possible in these experiments, as the fluorescence emitted by the scalars at the measurement location could have been absorbed by dyed fluid between the measurement location and the PMTs. Therefore, tests similar to Saylor (1993) were developed to determine any trapping effects for the experimental conditions of this work.

The trapping tests were conducted in a modified version of the calibration box. A ¼ inch (6.35 mm) thick glass dividing wall was added to the calibration box to create two independent compartments. The front compartment (i.e., closest to the PMTs) had dimensions of 21.6 cm by 30.5 cm by 51 cm, while the back compartment had dimensions of 54.5 cm by 30.5 cm by 51 cm. This modified calibration box was also placed inside the large tank to reduce the required amount of fluorescent dye and closely resemble experimental conditions.

To begin each trapping test, a known concentration of dye was mixed into the back compartment of the modified calibration box. The jet was also placed in the back compartment with dye constantly cycling through it, to as closely as possible reproduce the experimental conditions, and minimize photobleaching and thermal blooming effects. The optical chopper was also on during these tests to further minimize any photobleaching or thermal blooming effects. The dyed fluid was then irradiated with the laser, at a power of 1.5 W, and the subsequent fluorescent signal was sampled. The average of this signal was then stored as the reference value, with no trapping effects. Next, a known concentration of fluorescent dye was mixed into the water in the front compartment (located between the PMTs and the back compartment). Again, the back compartment was irradiated with the laser and the fluorescent signal was detected. This fluorescence signal was then compared to the reference signal from the tests with no dye in the front compartment. Any differences in the two signals could be attributed to trapping effects.

All possible combinations of dyes were tested to determine if trapping was significant in the present study. Tests were conducted with each fluorescent dye's concentration at its average value, at the measurement location, from the turbulent jet experiments. The dye in the front compartment of the calibration box was also at the

same concentration as its average respective concentration at the measurement location during actual experiments. This average value was chosen for these tests so as to overestimate any trapping effects, since species concentrations decrease with increased downstream position. Therefore, there was more dyed fluid present beyond the measurement location in these tests than in an actual experiment and, hence, trapping effects were greater here than in an actual experiment.

Four tests were conducted for each dye and also for a mixture of both dyes, resulting in a total of twelve tests. The disodium fluorescein tests were conducted with the back compartment containing a known concentration of disodium fluorescein. The front compartment for the four tests contained either; i) no dyed fluid, ii) just disodium fluorescein, iii) just sulforhodamine 101, or iv) a mixture of sulforhodamine 101 and disodium fluorescein. Similar tests were conducted with sulforhodamine 101 and a mixture of both dyes in the back compartment. As mentioned above, the dye concentrations in each case were the same as their respective average concentration at the measurement location from the experiments.

The results indicated that trappings effects were negligible in all cases. In each instance, there was a negligible difference ($\pm$ 0.03 V) between the detected reference fluorescence signal obtained when there was only dye in the back compartment to the detected fluorescence signal when both compartments contained dye, to within overall system repeatability ($\pm$ 0.05V). (The system repeatability was determined by calculating the standard deviation from multiple realizations of identical concentrations of the fluorescent dyes during the calibrations). These results were observed regardless of the chosen combination of fluorescent dyes.

4.7.3 Attenuation

As the laser beam passes through dyed fluid, it will attenuate as its energy is absorbed by the fluorescent tracer. If the laser beam passes through different amounts of dyed fluid before reaching the measurement location throughout the course of an experiment (as in the case of a turbulent jet) then the laser intensity may vary at this location. Therefore, a test was developed to determine if attenuation was significant for the conditions in this work.

The attenuation test was conducted with a known concentration of dye in the calibration box. Again, the dye was cycled through the jet and the optical chopper was on so as to prevent any photobleaching or thermal blooming effects, similar to the trapping tests. The average fluorescence signal was first detected with the measurement location at the centre of the calibration box. Next, the test was repeated with the calibration box shifted by 10 cm, such that the laser beam passed through 10 cm less of dyed fluid before reaching the measurement location. The average fluorescent signals from the two locations were then compared, with any differences being attributed to attenuation.

Attenuation tests were performed with disodium fluorescein, sulforhodamine 101, and a mixture of the two dyes at the same concentrations as their respective average concentrations at the measurement location during the turbulent jet experiments. There were no noticeable differences ($\pm$ 0.02 V), i.e. any changes were less than the overall system repeatability ($\pm$ 0.05 V), in the value of the fluorescence signal from any of the dyes when comparing the results from a measurement location at the centre of the calibration box to one shifted by 10 cm. Furthermore, these attenuation tests were a worst case scenario, since the dye concentrations were at their average centreline values, at the measurement location, during experiments. In an actual experiment, the laser beam would pass through less dyed fluid since the average concentration decreases with increased radial distance from the centreline of the jet. Therefore, attenuation was also negligible for all the experiments conducted in this work.

4.7.4 Buoyancy and Inertial Effects

Care was also taken to ensure that there were no buoyancy or inertial effects during this work. These effects would have been possible if the jet fluid had a different density than the ambient fluid into which it issued or if the jet fluid was heated at the measurement location, thereby resulting in a density difference. Density differences of the issuing fluid could have occurred if the jet fluid was at a different temperature than the background fluid or if the presence of the fluorescent dye caused a change (increase) in density of the jet fluid. Heating of the jet fluid at the measurement location was also

possible from laser irradiation, i.e., thermal blooming. These effects will be discussed and quantified in this section.

The fluorescent dyes were added to the jet fluid in dilute concentrations. (The jet nozzle concentration for all experiments was 2×10^{-7} mole/litre for disodium fluorescein and 6×10^{-7} mole/litre for sulforhodamine 101.) The molecular weights of disodium fluorescein and sulforhodamine 101 (as given by the manufacturers) are 376.28 g/mole and 606.71 g/mole, respectively. Therefore, when mixed in water ($\rho_w = 1000$ kg/m^3), the difference of the densities of the dyed jet fluid, at the jet nozzle (where the scalar concentrations were the greatest), and the background fluid was calculated to be 4.7×10^{-5} %, a negligible difference.

Buoyancy effects will eventually influence the jet at a location downstream of the nozzle. This distance was calculated analogously to the method of Miller and Dimotakis (1991). Dowling (1988) derived a non-dimensional buoyancy lengthscale:

$$\frac{L_b}{d} \equiv \left(\frac{\pi \rho_j}{4 \rho_\infty} \right)^{1/4} \left(\frac{\rho_j u_o^2}{(\rho_j - \rho_\infty) g d} \right)^{1/2}$$ (4.12)

where ρ_j is the jet fluid density, ρ_∞ is the background fluid density, and g is gravitational acceleration. Papanicolau and List (1987, 1988) found jets to be momentum dominated if x/L_b was less than one while Chen and Rodi (1980) defined jets to be momentum dominated for a value of x/L_b less than 0.5. The jet fluid density used for these calculations was for a combination of disodium fluorescein, at a concentration of 2×10^{-7} mole/litre, and sulforhodamine 101, at a concentration of 6×10^{-7} mole/litre. These concentrations yielded a difference in the jet fluid density and background fluid density of 4.67×10^{-4} kg/m^3. Thus, the smallest non-dimensional buoyancy lengthscale in this work was calculated to be 2643, which occurred at a Reynolds number of 4300 when the jet diameter was 8 mm (see section 5.2.1). Therefore, the jet in this work was momentum driven for at least 1321 jet diameters downstream, using the more stringent condition of Chen and Rodi (1980). Clearly, the jet did not experience any buoyancy effects in these experiments, since measurements were taken at only 50 jet nozzle diameters downstream of the exit.

A density difference between the dyed fluid and background fluid could also have occurred if the two fluids were at different temperatures. This would have been possible

if the dyed jet fluid was entering the background at a different temperature, or if the laser heated the dyed fluid in the measurement volume. The first possibility was eliminated by taking the water for the jet fluid from the large tank of background fluid, just prior to conducting an experiment. A mercury thermometer was also used to monitor the temperature of both fluids, ensuring that they were equal.

Heating of the dyed fluid in the measurement volume by the laser beam was calculated by the same method as Miller and Dimotakis (1991). It was assumed that all of the attenuation of the laser beam, as it passed through the cross-section of the jet, went into heating the dyed fluid. For the purpose of this calculation, the maximum total attenuation across the cross-section of the jet was assumed to be 3 % (for the 8 mm diameter jet), a conservative estimate since the attenuation was found to be negligible for a length slightly greater than the maximum jet radius at the measurement location (see section 4.7.3). Therefore, the attenuation across the measurement volume, a 100 µm length, was estimated to be 0.002 % by assuming that the total 3 % attenuation across the jet cross-section was linear. The calculated jet diameter, at the measurement location, of 18 cm was also used for this estimate (see section 4.2.2). Maximum heating occurred when a parcel of fluid resided in the measurement volume for the longest time period. This coincided with the 8 mm diameter jet at a Reynolds number of 4300. In this instance, the mean centreline axial velocity at the measurement location was estimated to be 0.065 m/s (see section 5.2.1). Therefore, the residence time of a parcel of dyed fluid was approximately 0.0015 s, using a measurement volume diameter of 100 µm. When estimating the measurement volume to be a 100 µm long cylinder with a diameter of 100 µm, the heating of the parcel of fluid was estimated to be 0.01°C, using the above estimate. Hence, heating of dyed fluid in the measurement volume was negligible and did not influence the results.

4.7.5 PMT Drift

Instability of the output signal, or drift, can occur when using PMTs as photon detection devices. The drift in a typical Hamamatsu PMT, the type used in this work, is generally a few percent of the acquired signal after about five minutes, and then slowly increases with time (Hamamatsu 2006). The majority of LIF experiments which employ

PMTs to detect a fluorescence signal last for a short period of time, typically a few seconds or less, and therefore drift is not a concern. However, in this study, data acquisition lasted for up to 15 minutes per experiment. This relatively long time period was due to the length of the blocks that were required, from pulsing the laser and, hence, PMT drift was a concern that needed to be addressed.

Drift in the output signal from the PMTs was observed while performing preliminary experiments. Figure 4.19 is a plot of the average output voltage from the disodium fluorescein PMT of a single-dye experiment of disodium fluorescein, at Re = 10600. In this figure, as well as in Figure 4.20, both the average output voltage of each individual block (Block Average) and the average of the output voltage up to the respective block (Moving Average) are plotted. In this test, the PMT was warmed up for 60 minutes before commencing data collection by turning it on, in the absence of a light source. The (magnitude of the) average output voltage is increasing in time, as can be seen in the figure. However, since the measurements were acquired at one location in the jet, the average concentration (and thus output voltage) should be constant in time.
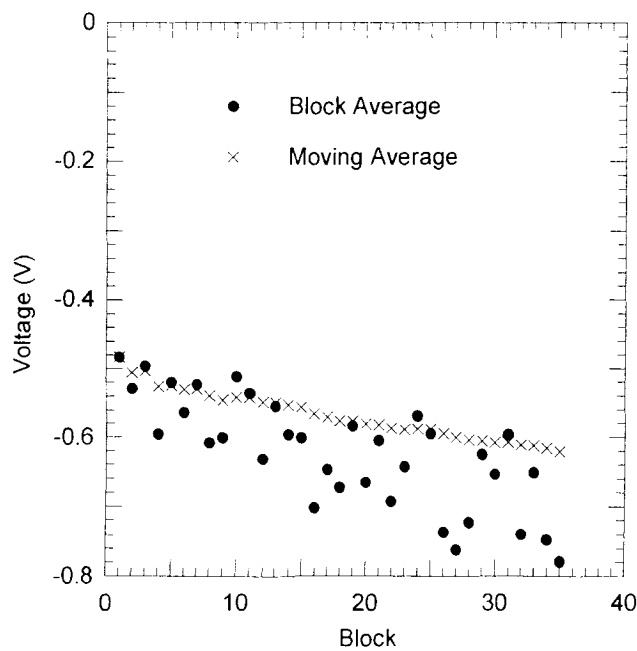
Figure 4.19: Average voltage output from a single-dye experiment of disodium fluorescein at Re = 10600 and r/d = 0. PMTs warmed up without a light source.

One solution to reduce the drift in the output signal is to warm the PMTs up in the presence of a light source, as recommended by the manufacturer. This solution was implemented and the PMTs were warmed up with a light source whose intensity resulted in output voltages similar to the averages obtained during an experiment. A light emitting diode (LED) was used as the light source during the warm up period of approximately 60 minutes. Figure 4.20 displays the average output voltage from the disodium fluorescein PMT from a two-dye experiment at a Reynolds number of 10600. The fluctuations in the Block Average in this figure (as well as in Figure 4.19) are due to the turbulent nature of the jet. Therefore, the average of any given block may be greater than or less than the steady statistical average (as can be seen by comparison with the moving average) since the turbulent signal fluctuates about its mean. Upon comparing Figures 4.19 and 4.20, it can be seen that the drift was significantly reduced by warming up the PMTs in the presence of a light source. Therefore, for every turbulent jet experiment conducted, the PMTs were warmed up with an LED for approximately 60 minutes prior to the start of data acquisition.
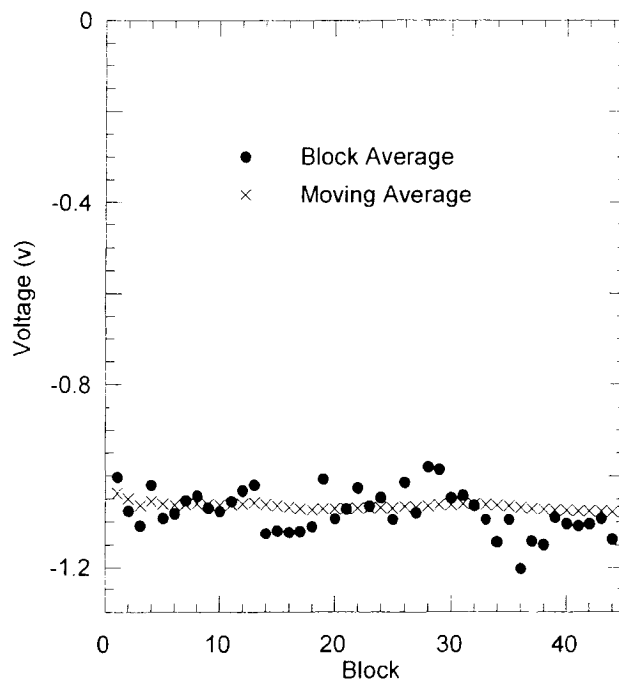
Figure 4.20: Average voltage output from the fluorescence signal of disodium fluorescein from a two-dye experiment at Re = 10600 and r/d = 0. PMTs warmed up in the presence of an LED.

To my knowledge, this is the first LIF study that mentions PMT drift and warming of the PMTs in the presence of a light source. PMT drift may not be a concern in LIF experiments which last for only seconds or less. However, from these results, drift should be monitored in LIF experiments which carry on for several minutes or longer.

Chapter 5

Experimental Conditions and Flow Validation

5.1   Calculation of Scales and Velocities

This section is intended to overview the theoretical and empirical correlations used to calculate several key parameters in a turbulent jet.   In order to establish the resolution of the experiments, it was necessary to determine the various length and time scales of the jet at the measurement location.   Establishing these scales also enabled quantification of the scales at which differential diffusion was present.   Length and time scales were calculated for all of the Reynolds numbers (Re = 900, 2100, 4300, 6700, and 10600) and jet diameters (d = 1.6, 3.81, and 8 mm) employed in these experiments. Since only concentration measurements were made, previously established empirical correlations were used to determine the velocities necessary to calculate the length and time scales.

Differential diffusion has been assumed to manifest itself at scales smaller than the Kolmogorov scales.   At these scales, the kinematic viscosity dominates and turbulent kinetic energy is converted into internal energy.   These scales can be determined from dimensional   considerations   using   Kolmogorov's   universal   equilibrium   theory (Kolmogorov 1941).   In this theory, Kolmogorov postulated that the small scales only

depend on the kinematic viscosity and the turbulent kinetic energy dissipation rate, ε

($\varepsilon \equiv 2\nu\langle s_{ij}s_{ij}\rangle$, where $s_{ij} \equiv \frac{1}{2}\left(\frac{\partial u_i}{\partial x_j}+\frac{\partial u_j}{\partial x_i}\right)$ is the fluctuating rate of strain tensor). The

Kolmogorov length (η), velocity (υ), and time (τ) scales can be formulated from these two quantities:

$$\eta \equiv \left(\nu^3/\varepsilon\right)^{1/4} \tag{5.1}$$

$$\upsilon \equiv \left(\nu\varepsilon\right)^{1/4} \tag{5.2}$$

$$\tau \equiv \left(\nu/\varepsilon\right)^{1/2}. \tag{5.3}$$

When dealing with scalar concentrations, the scalar diffusion or Batchelor scale may also be relevant. This scale is analogous to the Kolmogorov length scale for scalar mixtures with Schmidt numbers much greater than one (as is the case for many dyes in liquids). The Batchelor scale is defined as (Batchelor 1959):

$$\eta_b \equiv \left(\frac{D^2\nu}{\varepsilon}\right)^{1/4} = \eta Sc^{-1/2}. \tag{5.4}$$

Before determining the above dissipative scales, a correlation for the turbulent kinetic energy dissipation rate is needed. For a turbulent jet, this correlation was determined by Friehe et al. (1971) to be:

$$\varepsilon = 48\left(\frac{u_0^3}{d}\right)\left(\frac{x-x_0}{d}\right)^{-4}, \tag{5.5}$$

where x_0 is the virtual origin (assumed to be zero in this work).

A final experimental correlation, for the mean centreline axial velocity ($U_{cl}(x)$), was required. This parameter serves two purposes. Firstly, this velocity is employed to implement Taylor's frozen flow hypothesis, and thus to convert the Kolmogorov length scale into a frequency (see section 5.2.1). It is also utilized to determine the residence time of a parcel of fluid as it is convected through the measurement volume. This relation is given by the following experimental correlation (Chen and Rodi 1980):

$$U_{cl}(x) = 6.2u_0\left(\frac{x-x_0}{d}\right)^{-1}. \tag{5.6}$$

The above experimental correlations have been successfully employed in previous studies that have utilized LIF to measure species concentrations. For example, Miller and Dimotakis (1991) used the above correlation for the turbulent kinetic energy dissipation rate to determine the Kolmogorov scales in their work. Saylor (1993) applied the correlations for the mean centreline axial velocity and turbulent kinetic energy dissipation rate in determining the scales in his experiments.

5.2   Experimental Conditions

This section will be divided into two subsections. Firstly, the conditions for the experiments with the jet issuing into a quiescent background will be presented. This will be followed by a subsection that will detail the conditions for the experiments when the jet issued into a background of approximately homogeneous, isotropic turbulence with zero-mean flow.

5.2.1 Quiescent Background Conditions

As previously mentioned, the experimental conditions for this work included five Reynolds numbers, ranging from 900 to 10600, with three different jet diameters. Under all circumstances, measurements were obtained at a downstream distance of 50 jet diameters from the jet nozzle ($x/d = 50$). These conditions were chosen so as to have a wide range of Reynolds numbers while still meeting the constraints imposed by the apparatus.

It was desired to conduct these experiments at a range of Reynolds numbers such that, at the highest Reynolds number, the jet would exhibit fully-developed turbulence, past the mixing transition. The mixing transition for turbulent jets occurs at a Reynolds number around 10^4 (Dimotakis 2000). Therefore, a high Reynolds number of 10600 was chosen since it was above the mixing transition and met the constraints of the apparatus (see below). The low Reynolds number was chosen to be the lowest value that could meet the constraints of the apparatus while using a 1.6 mm diameter jet. Under these conditions, the Reynolds number was 900.

Three different jet diameters were chosen to transition from the low to high Reynolds number. Due to the constraints of the apparatus, it was not possible to span the

71

entire range of desired Reynolds numbers while using just one jet diameter. It was possible to span the entire range of Reynolds numbers with two different jet diameters. However, three different jet diameters were chosen in order to compare results from experiments conducted with two different jet diameters, at the same intermediate Reynolds number. Thus, it was assured that the use of different jet diameters did not influence the results.

The three different jet diameters utilized in this work were d = 1.6, 3.81, and 8 mm. The highest possible Reynolds number under the constraints of the apparatus for the 1.6 mm jet was just above 2100. Therefore, experiments were conducted at Reynolds numbers of 900 and 2100 with the 1.6 mm diameter jet. Under the limitations of the apparatus, the 3.81 mm diameter jet could be operated at Reynolds numbers from 2100 to just above 4300. The largest jet diameter (d = 8 mm) permitted Reynolds numbers ranging from 4300 to 10600. This jet was operated at these two extremes plus at an intermediate Reynolds number of 6700. Consequently, experiments were conducted with two different jet diameters at each transition Reynolds number (when transitioning from one jet diameter to another).

The two main constraints imposed by the apparatus, which led to the chosen jet diameters and Reynolds numbers, were the maximum and minimum sampling frequencies. The maximum chopping frequency was constrained by the capabilities of the optical chopper. For the Scitec 310CD optical chopper operated with two offset five-slot discs, the maximum chopping frequency was slightly less than 1700 Hz. Therefore, the maximum mean centreline axial velocity was chosen so that the corresponding chopping frequency was 1606 Hz, within the capabilities of the optical chopper.

The minimum chopping frequency was constrained by computing capabilities. The maximum block size that could be sampled on the available computer was 524288 points (per channel) in length. From this long block, the data was processed down to a block of 4096 points per channel, as described in section 4.3. Therefore, the minimum chopping (i.e., sampling) frequency to acquire the desired 4096 processed points was

651 Hz $\left(f_{min} = 83333 * \dfrac{4096}{524288} \right)$, where 83333 is the data sampling frequency.

Frequencies lower than 651 Hz would require blocks of greater than 524288 points per channel, which was not possible under the current setup.

The chopping frequency was (inversely) related to the amount of time a parcel of fluid would reside in the measurement volume. This time was calculated from the above correlation for the mean centreline axial velocity (equation 5.6) and the diameter of the measurement volume. The chopping frequencies for each Reynolds number and jet diameter employed in this work are listed in Table 5.1.

Table 5.1: Mean centreline axial velocity and chopping frequency for each Reynolds number and jet diameter employed.

Re	d (mm)	U_{cl} (cm/s)	Chop. Freq (Hz)
10600	8	16.1	1606
6700	8	10.2	1015
4300	8	6.5	651
4300	3.81	13.7	1368
2100	3.81	6.7	668
2100	1.6	15.9	1591
900	1.6	6.8	682

After deciding on the experimental conditions, it was necessary to determine the Kolmogorov and Batchelor scales for each case. These calculations then gave an indication of the spatial and temporal resolution in this work. Using the empirical correlations introduced in section 5.1, the Kolmogorov and Batchelor lengthscales for the various conditions under consideration in this study are listed in Table 5.2.

Table 5.2: Centreline Kolmogorov and Batchelor lengthscale for each
Reynolds number and jet diameter employed.

Re	d (mm)	η (μm)	η_b (μm)
10600	8	145.5	2.1
6700	8	205.2	2.9
4300	8	286.2	4.1
4300	3.81	136.3	1.9
2100	3.81	233.3	3.3
2100	1.6	98.0	1.4
900	1.6	185.0	2.6

The Batchelor scales in the above table were calculated for the less diffusive scalar (sulforhodamine 101, Sc_2 = 5000), and are therefore the smallest possible scales in each instance. Recall that the spatial resolution in this work was 100 μm. Therefore, as can be seen in the table, the Batchelor scale was not resolved for any of the experiments. However, one of the goals of this work was to determine if differential diffusion effects are present at scales of the same order and greater than the Kolmogorov scale. It was possible to achieve this goal, since the Kolmogorov scale was resolved for all Reynolds numbers (except for Re = 2100 with the 1.6 mm diameter jet). Even though the Kolmogorov scale was not resolved for this case, it was still resolved at Re = 2100 for the 3.81 mm diameter jet.

Another condition of interest, when analyzing the results, was the Kolmogorov frequency at the measurement location. Knowledge of this frequency also aided in determining the scale dependence of differential diffusion effects. It was used herein as the cut-off frequency when calculating Z_{rms} (see section 6.1.2) and in analyzing the normalized concentration difference spectrum (see section 6.1.3). Comparing the calculated Kolmogorov frequency with the sampling frequency also gives an indication of the temporal resolution in this study. For the flow under consideration, the Kolmogorov frequency was determined from the following equation:

$$ f_\eta = \frac{U_{cl}}{2\pi\eta}, \tag{5.7} $$

implementing Taylor's frozen flow hypothesis. Table 5.3 lists the Kolmogorov and chopping frequencies for all of the experimental conditions. As can clearly be seen from the table, in each instance, the Kolmogorov frequency was resolved.

Table 5.3: Kolmogorov and chopping frequency for each Reynolds number and jet diameter.

Re	d (mm)	Kol. Freq. (Hz)	Chop. Freq. (Hz)
10600	8	176	1606
6700	8	79	1015
4300	8	36	651
4300	3.81	160	1368
2100	3.81	46	668
2100	1.6	258	1591
900	1.6	59	682

To quantify the intensity of differential diffusion effects at scales greater than the Kolmogorov scale, the r.m.s. of the normalized concentration difference, Z_{rms}, was studied. The true value of Z_{rms}, obtained by integration of the normalized concentration difference spectrum, would provide contributions over the entire range of scales. However, due to the resolution constraints, Z_{rms} was calculated by integrating the normalized concentration difference spectrum up to the Kolmogorov scale (see section 6.1.2). Hence, all the contributions to the calculated Z_{rms} presented herein were at scales larger than the Kolmogorov scale, thus providing an indication of the presence of differential diffusion effects at these and larger scales. This method of calculating Z_{rms} also provided a rational and consistent method for its computation and subsequent comparison at different Reynolds numbers and radial locations.

5.2.2 Turbulent Background Conditions

When performing experiments with the jet issuing into a quasi-isotropic turbulent background, it was necessary to calculate the velocities in the turbulent jet and in the

surrounding ambient fluid. The desired condition was for the r.m.s. axial centreline jet velocity to be greater than the r.m.s. velocity of the background turbulence, at the measurement location. The results from these experiments would then serve to provide differential diffusion statistics in an additional flow regime.

To accomplish the stated objective, velocity measurements in the background turbulence were acquired when the random jet array was operated with the previously described algorithm (see section 4.2.1). Recapitulating, once a pump was turned on, it remained on for a random time selected from a normal distribution with an average of 12 seconds and with a standard deviation of 4 seconds. Conversely, once a pump was turned off, it remained in this state for a random time selected from a normal distribution with an average of 108 seconds and with a standard deviation of 36 seconds. Other algorithms were studied, but their results are not presented here.

The approximately isotropic turbulent background field was characterized by obtaining velocity measurements with a SonTek 10-MHz field Acoustic Doppler Velocimeter (ADV). This ADV had a 0.25 cm^3 sampling volume and the accuracy of the velocity signal was 1 % of the sampling range. The sampling range was selected to be ± 30 cm/s, which spanned the entire range of measured velocities. The sampling rate was maintained at 25 Hz, the maximum for this device, for all but a few tests. To obtain the low frequency range of the velocity spectrum, the sampling rate was reduced to 2 Hz. Since the ADV operated by reflecting an acoustic signal off of particles in the flow, the SNR in initial tests was extremely low. This phenomenon was due to the nature of the "clean filtered water" (i.e., free of sufficient particles to acquire an adequate signal) in the tank. Therefore, it was necessary to seed the flow with tracer particles (Potters Industries Sphericel hollow glass spheres) to increase the SNR in these measurements. These glass spheres had diameters ranging from 11 to 18 μm and were neutrally buoyant. Note that the tracer particles were only present during these velocity measurements, and not when the turbulent jet issued into the flow.

Velocity measurements were acquired at several locations in the turbulent background. The first such position was at the measurement location in the turbulent jet (110 cm downstream of the outlets of the PVC extensions on the random jet array and 50 jet diameters downstream of the jet exit). The velocities at this location were then

76

compared to those calculated in the turbulent jet. Next, velocities were obtained at varying downstream locations from the random jet array (at the same vertical height and horizontal position as the measurement location in the turbulent jet). These velocity measurements provided information on the downstream decay of the turbulent background. Finally, to test the homogeneity of the background flow, measurements were conducted at several positions in a vertical plane located 110 cm downstream of the random jet array.

The random jet array produced a background field that was approximately isotropic turbulence with zero-mean flow at the measurement location. The r.m.s. velocities, along with the r.m.s. velocity ratios and mean velocities normalized by their respective r.m.s. velocity, at this location, are displayed in Table 5.4:

Table 5.4: Measurement location background turbulence conditions. All velocities have units of cm/s.

u_{rms}	2.16
v_{rms}	1.48
w_{rms}	1.43
$<U_b>/u_{rms}$	-0.07
$<V_b>/v_{rms}$	-0.01
$<W_b>/w_{rms}$	0.06
v_{rms}/u_{rms}	0.69
w_{rms}/u_{rms}	0.66
v_{rms}/w_{rms}	1.04

where u_{rms}, v_{rms}, and w_{rms} are the respective r.m.s. velocities in the downstream, horizontal transverse, and vertical directions, with respect to the random jet array and $<U_b>$, $<V_b>$, and $<W_b>$ are the mean velocities in the same respective directions as the r.m.s. velocities.

From the table, it is clear that the zero-mean flow assumption was valid for this flow, as the mean velocities normalized by their respective r.m.s. velocities are effectively zero. These values compare favourably to those obtained in the flow from a random jet array by Variano *et al.* (2004). The normalized mean flow created by the random jet array in this work is also significantly lower than that generally found in

quasi-isotropic turbulence created by oscillating grids (Fernando and De Silva 1993a, Thompson and Turner 1975). A background with zero-mean flow was important since the presence of a mean flow could act to convect the turbulent jet downstream, which could have had a significant impact on the scalar measurements in the jet. Therefore, on average, the turbulent jet was only subject to velocity fluctuations and was not convected downstream.

In an isotropic flow, the ratios of the r.m.s. velocities should be 1. Therefore, the results in Table 5.4 indicate that the flow is not perfectly isotropic at the measurement location. Variano et al. (2004) reported a flow that was closer to being truly isotropic, as the median of their ratios varied from 0.95 to 1.23. The flow generated by oscillating grids is typically characterized by anisotropy ratios between 1.1 and 1.2 (Hopfinger and Toly 1976).

Velocity spectra of all three velocity components, at the measurement location, are displayed in Figures 5.1. These spectra are a combination of spectra from measurements taken at two different sampling frequencies. One set of data was sampled at 2 Hz (yielding the low frequency end of the spectrum) and the other set was sampled at 25 Hz (yielding the high frequency end). All three spectra are similar, each of them having a significant inertial subrange. However, there is clearly a better SNR in the vertical velocity spectrum in Figure 5.1(c), $Ew_b(f)$, than the spectra in Figure 5.1(a) and 5.1(b), $Eu_b(f)$ and $Ev_b(f)$, respectively. This can be attributed to a finer spatial resolution of the ADV in the vertical direction.

(a)   (b)

$Eu_b(f)$

Frequency (Hz)

$Ev_b(f)$

Frequency (Hz)

(c)

$Ew_b(f)$

Frequency (Hz)
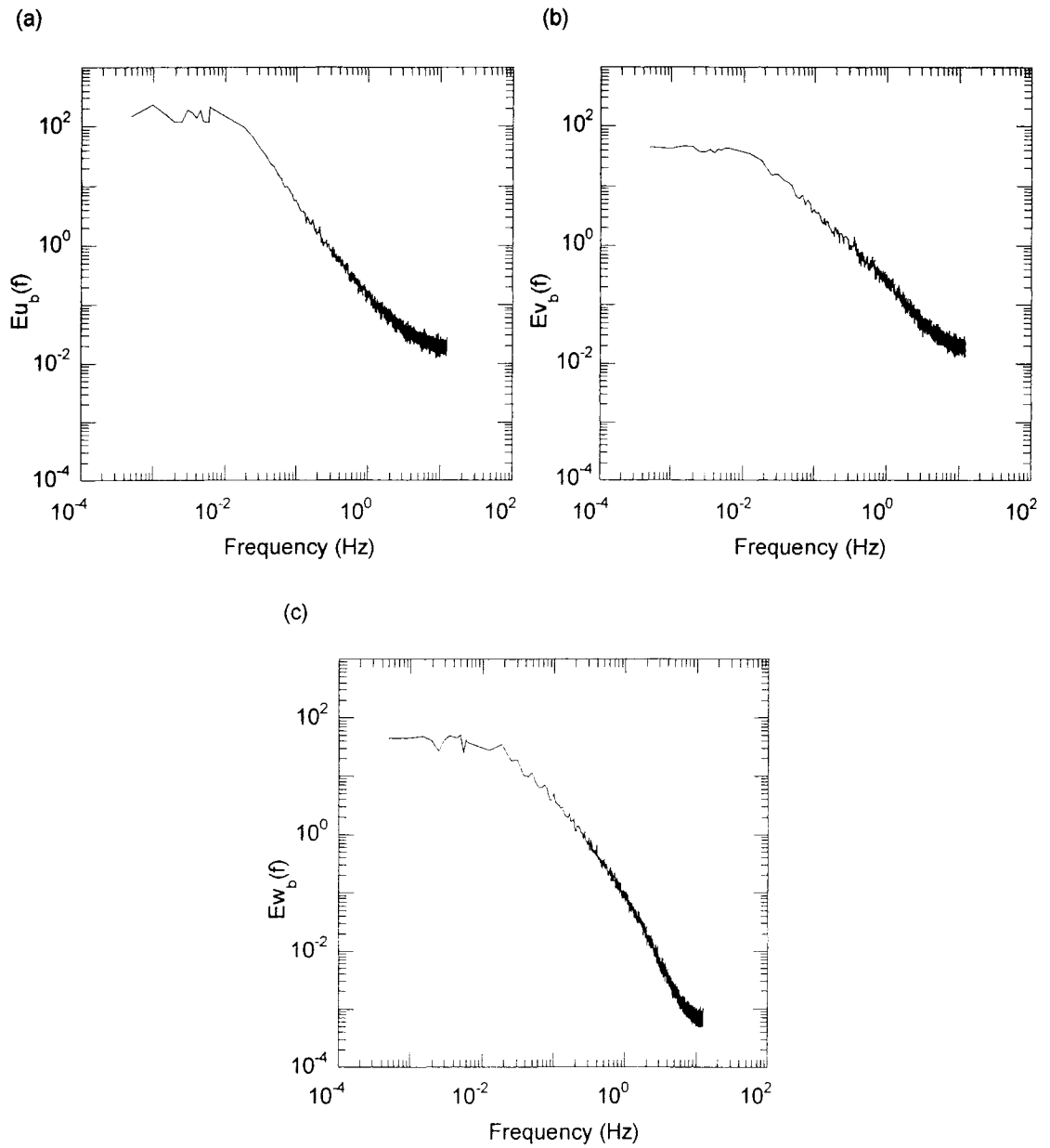
Figure 5.1: Velocity spectra at the measurement location in the turbulent background. (a) Spectrum of the downstream velocity component, $Eu_b(f)$. (b) Spectrum of the transverse horizontal velocity component, $Ev_b(f)$. (c) Spectrum of the vertical velocity component, $Ew_b(f)$.

Figure 5.2 displays PDFs of the fluctuations of each velocity component, at the measurement location. The PDF of the fluctuating downstream velocity component, Figure 5.2(a), is asymmetric, indicating a greater chance of positive downstream velocity fluctuations. On the other hand, the PDFs of the vertical and transverse horizontal

79

velocity fluctuations, Figure 5.2(b) and 5.2(c), respectively, appear to be approximately symmetric.
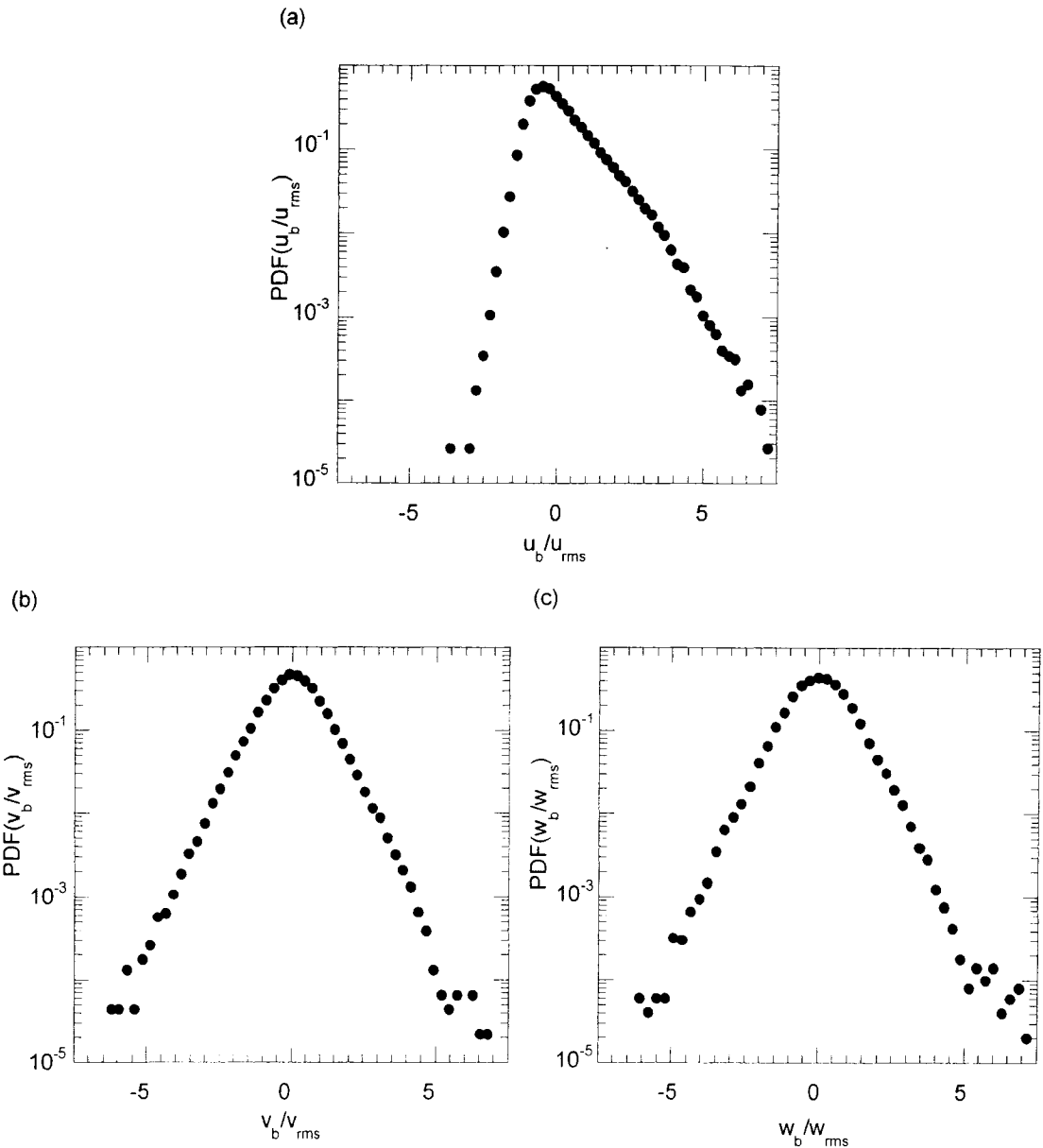
Figure 5.2: PDFs of the fluctuating velocity components at the measurement location in the turbulent background. (a) PDF of the downstream velocity fluctuation $PDF(u_b/u_{rms})$. (b) PDF of the transverse horizontal velocity fluctuation, $PDF(v_b/v_{rms})$. (c) PDF of the vertical velocity fluctuation, $PDF(w_b/w_{rms})$.

Measurements were also taken at several downstream locations, from 80 to 130 cm downstream of the outlets of the PVC extensions, to determine the decay of the background turbulence. Results are displayed in Figure 5.3 which depicts the downstream decay of all three r.m.s. velocity components. A power law is fit to each

velocity component. The decay exponents of the power laws average -1.3, consistent with the results of Mohamed and Larue (1990) for grid-generated wind tunnel turbulence. From these results, it should be noted that the downstream r.m.s. velocity will decay by 0.65 cm/s across the width of the jet (estimated to be 18 cm) at the measurement location. Since this decay is non-negligible, the turbulent background cannot be considered to be homogeneous in the downstream direction like grid-generated wind tunnel turbulence. However, given that the measurement location and random jet array do not move with respect to one another, the intensity of the background turbulence at the measurement location remains constant, allowing an appropriate comparison of the results.

$y = 2293.4 * x^{\wedge}(-1.4773)$ R= 0.98128

$y = 354.96 * x^{\wedge}(-1.1471)$ R= 0.98689

$y = 573.63 * x^{\wedge}(-1.2746)$ R= 0.97532
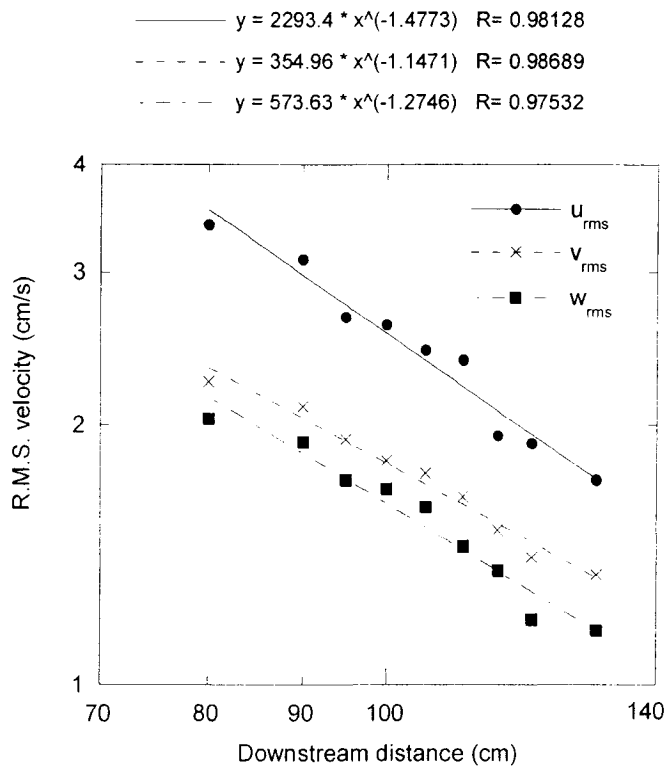
Figure 5.3: Downstream decay of r.m.s. velocity components in the approximately isotropic background turbulence.

Although the flow decayed downstream, the symmetric configuration of the random jet array should result in a two-dimensionally homogeneous flow away from the boundaries. To confirm this, turbulent background velocities were also measured in a vertical plane (at the downstream measurement location). These tests were conducted

along two lines (one vertical and the other horizontal) which passed through the centre of the plane. The results of these measurements are shown in Figure 5.4. Note that the x-axes in these plots are normalized by the centre to centre distance between the outlets of the PVC extensions (M = 15 cm). Figure 5.4(a) shows that the r.m.s. velocities were approximately homogeneous along the vertical line and Figure 5.4(b) shows that the r.m.s. velocities were approximately homogeneous along the horizontal line.

(a)   (b)
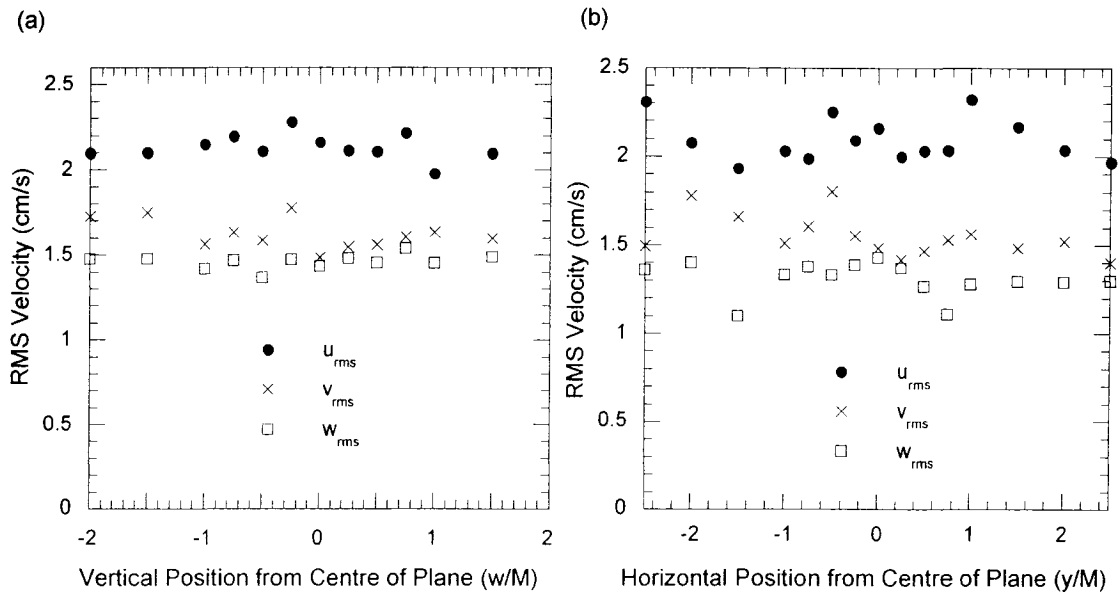
Figure 5.4: Homogeneity in a vertical plane at the measurement location. (a) R.M.S. velocities along a vertical line passing through the centre of the plane. (b) R.M.S. velocities along a horizontal line passing through the centre of the plane.

Due to the nature of the flow and measurement technique, it was not possible to determine a Reynolds number for the background turbulence. Spatial velocity gradients could not be obtained, since measurements were only acquired at one location at a given time. (A mean flow would have been necessary to invoke Taylor's frozen flow hypothesis to estimate spatial velocity gradients from measured temporal gradients). Thus, it was not possible to determine lengthscales in this flow. In the future, it may be possible to determine spatial velocity gradients through the use of flying hot-film anemometry or particle-image velocimetry (PIV). This would provide the information needed to calculate the turbulent kinetic energy dissipation rate, ε, the integral and the Taylor lengthscales.

82

For all but a few experiments, the turbulent jet was operated at one Reynolds numbers (Re = 10600) in the presence of the turbulent background. This value was chosen to obtain the desired ratio of the centreline r.m.s. axial velocity in the jet, u'_{cl}, to the downstream r.m.s. velocity of the background turbulence. The latter was chosen to be greater than one at the measurement location. The structure of a turbulent jet breaks down (characterized by an increased spreading angle) when the intensity of the background turbulence is similar to that in the jet (e.g. Hunt 1994 and Guo *et al.* 1999). Therefore, experiments for which this ratio is approximately (or less than) one should not yield useful results.

The centreline axial r.m.s. velocity was determined from empirical correlations. Recall from section 2.1 that, in the self-similar region, the centreline axial r.m.s. velocity asymptotes to a value of 0.24, when normalized by the mean centreline axial velocity, regardless of downstream position (Panchapakesan and Lumley 1993a). Therefore, using the mean centreline axial velocity calculated in section 5.2.1, the centreline axial r.m.s. velocity at the measurement location was 4 cm/s, at a Reynolds number of 10600. At the measurement location, the background turbulence had a downstream r.m.s. velocity of 2.16 cm/s (see Table 5.4). Hence, as desired, this value was significantly less than that of the turbulent jet at a Reynolds number of 10600.

5.3 Verification of the Independence of Individual Species Concentration Measurements

Since LIF was employed to simultaneously measure two species concentrations, it was important to ensure that the statistics of each dye were the same regardless of whether the jet contained one or two dyes. The following sections benchmark key statistics from this work to show that the measurement technique was accurate. To accomplish this, individual scalar concentration statistics were obtained for each scalar from three sets of experiments. The first two sets of experiments were conducted with the jet fluid containing a single fluorescent dye (disodium fluorescein or sulforhodamine 101) while the third set was performed with the jet containing both dyes. The statistics

of the individual scalars from the two-dye tests were then compared to those from the single-dye tests.

5.3.1 Scalar Concentration PDF Comparison

PDFs of the concentration fluctuations, PDF(c/c_{rms}), of one scalar in jets containing one or both dyes were compared. Figure 4.16 shows PDFs of concentration fluctuations of each fluorescent dye. The PDF of the concentration fluctuation of disodium fluorescein is depicted in Figure 4.16(a) and that of sulforhodamine 101 in Figure 4.16(b). These experiments were conducted along the centreline at a Reynolds number of 10600. Figure 4.16 shows that the PDF from a single-dye experiment collapses well when compared to the PDF from a two-dye experiment, for both disodium fluorescein and sulforhodamine 101.

5.3.2 Spectrum and R.M.S. Scalar Fluctuation Comparison

Spectra of the individual scalars were also computed to compare single-dye and two-dye experiments. Plots of the spectrum of each dye are depicted in Figure 5.5 for tests conducted along the centreline at a Reynolds number of 10600. The spectra of the concentration of each dye collapse well on each other, as there is no discernible difference in the spectra between single-dye and two-dye experiments. This collapse is consistent with the PDFs of the individual scalar concentration fluctuations and strong evidence supporting the validity of the measurement technique.
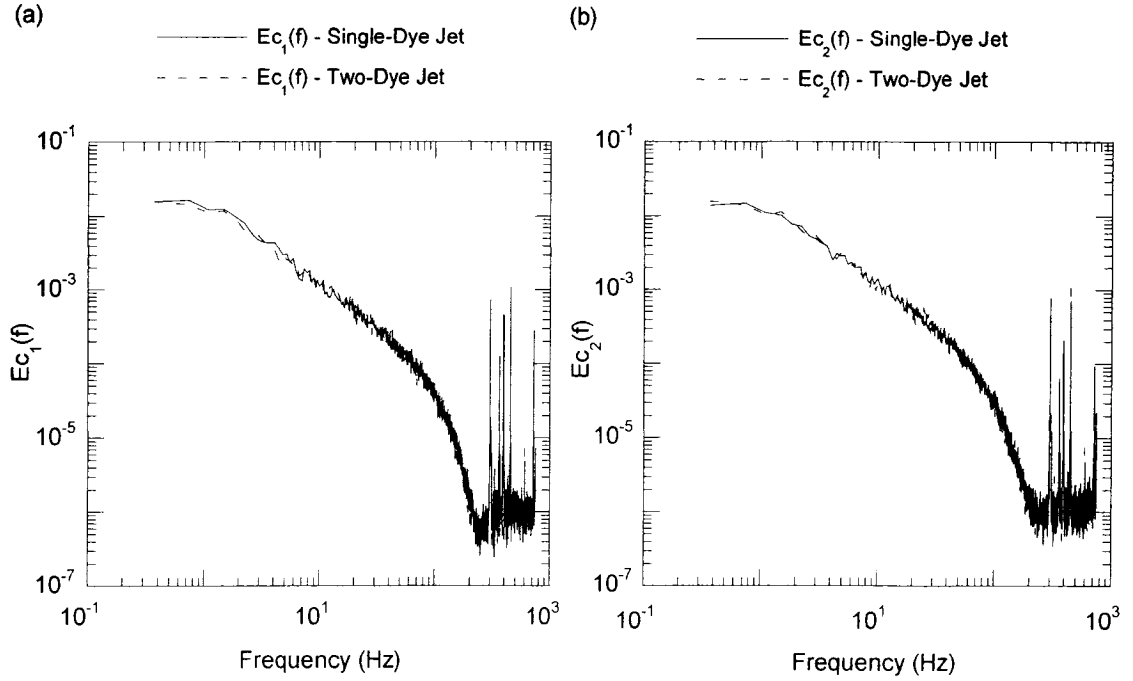
Figure 5.5: Individual scalar spectra comparison between single and two-dye experiments conducted at the centreline at Re = 10600. (a) Disodium fluorescein, $Ec_1(f)$ and (b) sulforhodamine 101, $Ec_2(f)$.

The scalar spectra can be used to calculate normalized r.m.s. concentration fluctuations for each scalar. This is accomplished by integrating the spectrum over all frequencies:

$$\frac{c_{rms}}{\langle C \rangle} = \left[\frac{\langle c^2 \rangle}{\langle C \rangle^2} \right]^{1/2} = \left[\frac{1}{\langle C \rangle^2} \int_0^\infty E_c(f)df \right]^{1/2} , \qquad (5.8)$$

where c_{rms} is the r.m.s. of the concentration fluctuation, c is the concentration fluctuation, and $E_c(f)$ is the power spectrum of the scalar concentration.

However, only a surrogate of the above was measured, due to the constraints of the apparatus. Since the scalars in this study had Schmidt numbers of the order 10^3, it would have been necessary to resolve down to the Batchelor scale to obtain the true r.m.s of the scalar fluctuations. Therefore, the scalar spectrum was integrated to a scale that was resolved for all the experimental conditions, the Kolmogorov scale:

$$\frac{c_{rms,meas}}{\langle C \rangle} = \left[\frac{\langle c^2 \rangle}{\langle C \rangle^2} \right]^{\frac{1}{2}}_{meas} = \left[\frac{1}{\langle C \rangle^2} \int_0^{f_\eta} E_c(f) df \right]^{\frac{1}{2}}. \qquad (5.9)$$

Thus, each r.m.s. scalar fluctuation was calculated to the same physical scale. Upon integration of the spectra depicted in Figure 5.5 (Re = 10600), the resulting normalized r.m.s. (centreline) concentration fluctuations are all about 0.25. This result is consistent with the work of Miller (1991) who found the normalized r.m.s. concentration fluctuations, *resolved down to the Batchelor scale*, of disodium fluorescein to be in the range 0.28-0.33 for a Reynolds number of 10^4.

5.4 Flow Validation

Individual scalar concentration statistics from two-dye experiments were compared with previous studies to validate the flow and measurement technique. These statistics will be presented in this section and include mean scalar concentrations and r.m.s. scalar concentration fluctuations.

The radial distribution of the average species concentration normalized by the average centreline concentration for two-dye experiments, at a Reynolds number of 10600, is plotted in Figure 5.6. There is good agreement between the average scalar concentrations (normalized by their respective average centreline concentration), for both scalars utilized herein. The decreasing trend observed in the figure is expected, and consistent with other studies, such as the helium jet results of Panchapakesan and Lumley (1993b), which are also displayed in Figure 5.6.

1.2

$\langle C \rangle / \langle C_{cl} \rangle$

0.8

0.4

○ $\langle C_1 \rangle / \langle C_{1,cl} \rangle$ - Present study
✕ $\langle C_2 \rangle / \langle C_{2,cl} \rangle$ - Present study
■ $\langle C \rangle / \langle C_{cl} \rangle$ - Panchapakesan and Lumley (1993b)

0

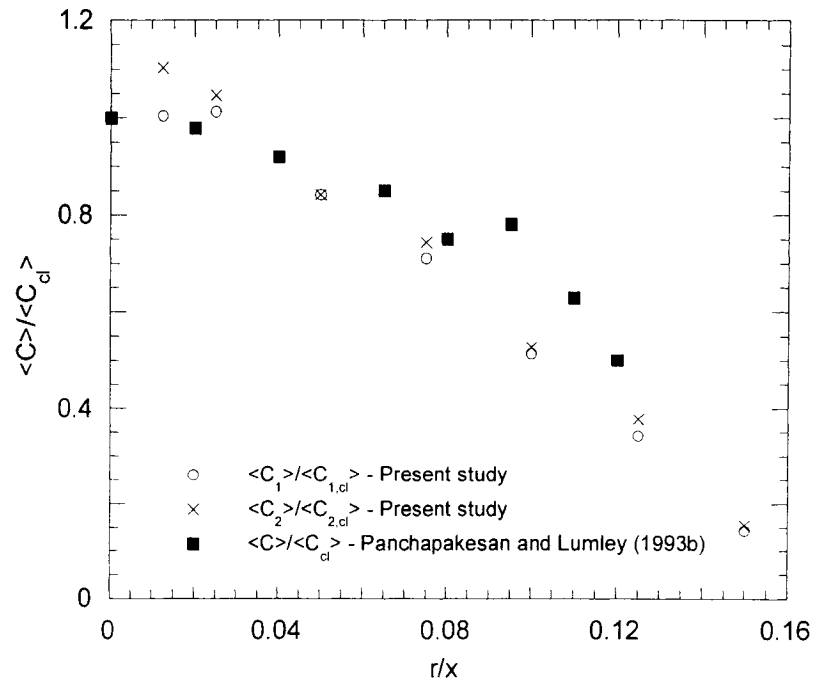0   0.04   0.08   0.12   0.16

r/x

Figure 5.6: Radial variation of normalized average scalar concentration of disodium fluorescein and sulforhodamine 101 from the present study and of helium from Panchapakesan and Lumley (1993b).

The r.m.s. scalar fluctuations of both fluorescent dyes were also calculated at the centreline for all of the Reynolds numbers employed in this work. Figure 5.7 depicts the Reynolds number variation of the centreline r.m.s. scalar fluctuations (normalized by their respective average concentration). All the points in this figure are from experiments in which the jet fluid consisted of both disodium fluorescein and sulforhodamine 101. These results are consistent with Figure 5.8 (which is Figure 6 of Dimotakis (2000) and also shows the Reynolds number dependence of the variance of the (centreline) scalar fluctuations normalized by the average scalar concentration). This figure plots the (high Schmidt number) liquid-phase data of Miller (1991) and the (low Schmidt number) gas-phase data of Dowling and Dimotakis (1990). Since this study was conducted in a (high Schmidt number) liquid-phase flow, it is only appropriate to compare the data with that of Miller (1991). The agreement supports the validity of the experimental technique to be used at the range of Reynolds numbers employed in this work
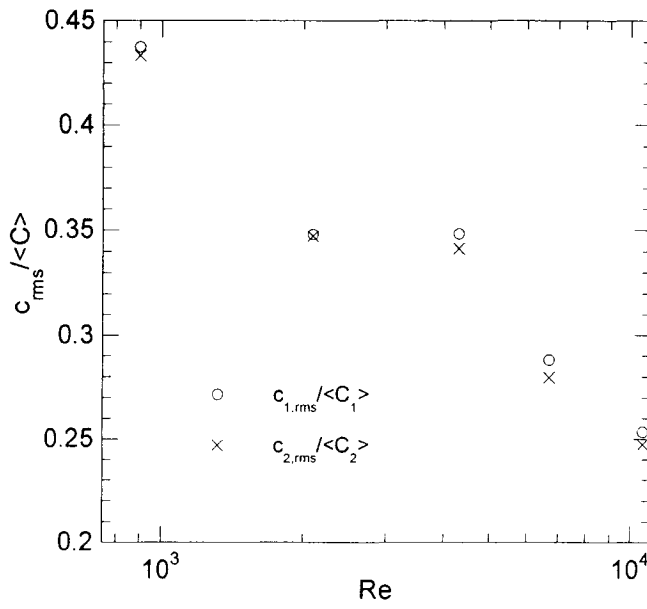
Figure 5.7: Reynolds number dependence of normalized r.m.s. scalar fluctuations along the jet centreline.
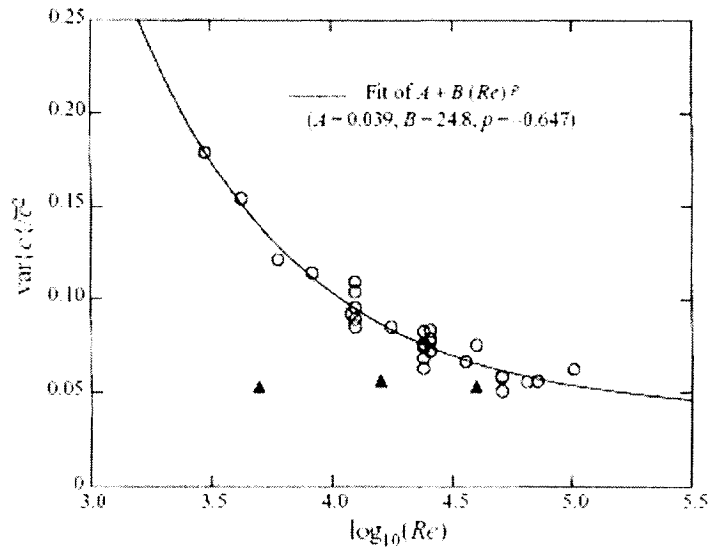
FIGURE 6. Normalized jet-fluid-concentration variance on the axis of a turbulent jet, as a function of jet Reynolds number (Miller 1991, figure 7.2). Circles: liquid-phase jets (Miller 1991); triangles: gas-phase jets (Dowling & Dimotakis 1990).

Figure 5.8: Reynolds number dependence of normalized concentration variance from Miller (1991) and Dowling and Dimotakis (1990). Plot from Dimotakis (2000).

88

Normalized r.m.s. scalar concentration fluctuations, of each scalar, were also calculated along a radial slice for experiments where the jet fluid consisted of both dyes, at a Reynolds number of 10600. The results of these calculations are displayed in Figure 5.9. When normalized by their respective mean centreline concentrations, the r.m.s. scalar concentration fluctuations first increase with increased radial position from the jet centreline then decrease in magnitude further away from the centreline. This trend is consistent with the observations of others, such as the results of Panchapakesan and Lumley (1993b) which are also shown in Figure 5.9. There is a difference in the magnitude of the normalized r.m.s. scalar concentration fluctuations between the results of this work and Panchapakesan and Lumley, which can be attributed to the different phases (and therefore Schmidt numbers) of the flows (see Figure 5.8). The present study was completed in a (high Schmidt number) liquid-phase flow while Panchapakesan and Lumley conducted their experiments in a (low Schmidt number) gas-phase flow. Therefore, the higher normalized r.m.s. concentration fluctuations obtained in this work were expected, as discussed in section 2.1. Relatively few high Schmidt number turbulent jet experiments have been completed (as compared to low Schmidt number jets); hence, the comparison between this study and Panchapakesan and Lumley shown in Figure 5.9.
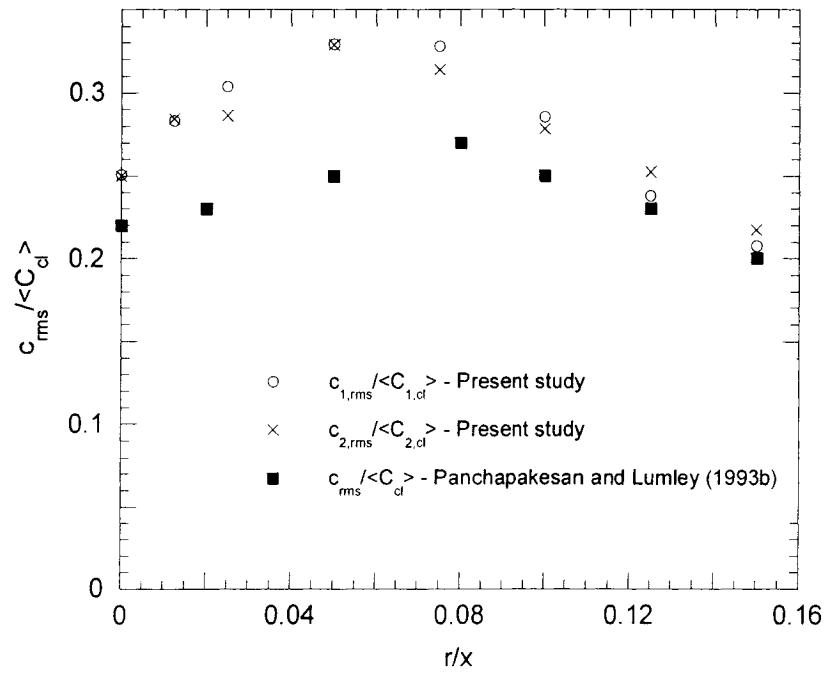
Figure 5.9: Radial variation of normalized r.m.s. scalar fluctuations of disodium fluorescein and sulforhodamine 101 from the present study at Re = 10600 and of helium from Panchapakesan and Lumley (1993b).

Chapter 6

Results

This chapter presents results pertaining to differential diffusion in a turbulent jet. The findings are centred on the statistics of the normalized concentration difference, Z, a parameter (developed from the advection-diffusion equation) that quantifies differential diffusion. The results presented herein include spectra, PDFs, r.m.s. fluctuations, and conditional expectations of the normalized concentration difference.

6.1 Quiescent Background

Experiments were first conducted with the turbulent jet issuing into quiescent fluid. These tests were performed with the three different jet diameters, and with the jet at all five of the Reynolds numbers presented in section 5.2. The results will both i) elucidate the nature of differential diffusion, and ii) provide the basis for later comparisons with experiments with the jet issuing into a background of quasi-isotropic turbulence.

6.1.1 Time Series

Time series of the individual scalar concentrations, along with their respective normalized concentration differences, (directly) exhibit differential diffusion effects. Any differences in the instantaneous normalized concentrations of the two species can be attributed to differential diffusion, since the two species enter the same flow with identical initial and boundary conditions. The normalized concentration difference time series quantifies these variations. Differential diffusion occurs whenever Z is non-zero.

Individual normalized species concentration time series, measured at the jet centreline, are presented for Reynolds numbers of 900 and 10600 in Figure 6.1. For a given Reynolds number, it is observed that the large-scale structures of both time series are similar. However, there are clear differences in the small-scale structure of the normalized concentration time series. These differences are an indication of the presence of differential diffusion at the small scales.
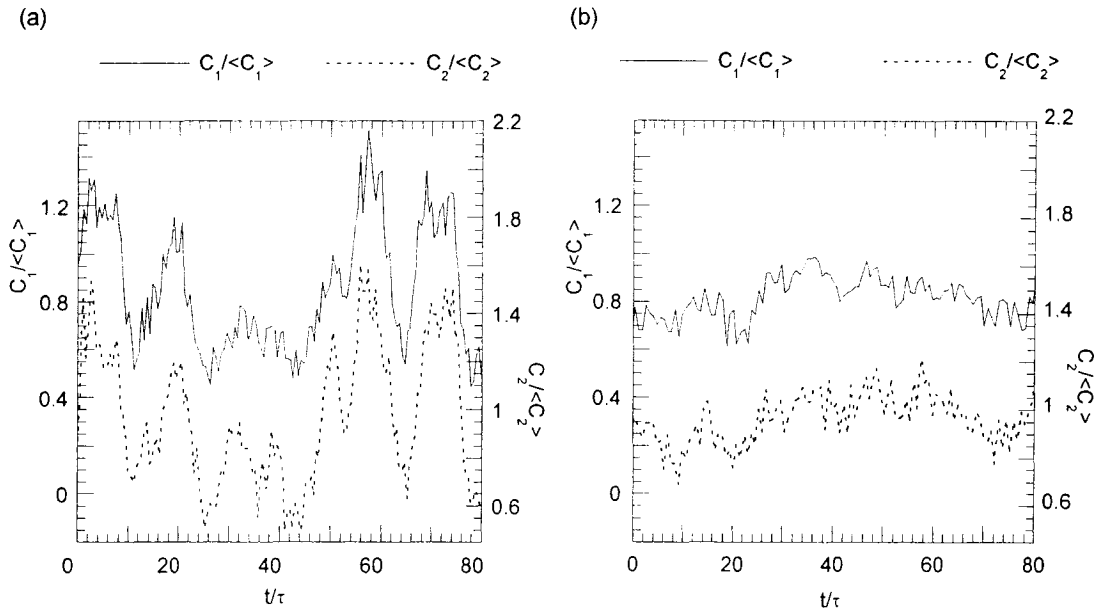
Figure 6.1: Normalized centreline scalar concentration time series. (a) Re = 900 and (b) Re = 10600. Note, y-axes are shifted with respect to each other.

A more pronounced indication of differential diffusion effects can be seen in the time series of Z. The Z time series depicted in Figure 6.2 correspond to the individual normalized scalar concentration time series in Figure 6.1. It is clear that differential diffusion effects are present at each Reynolds number as Z is non-zero more often than

not. However, note that the magnitudes of the fluctuations in Z are greater at the lower Reynolds number. This observation supports the notion that differential diffusion effects decrease with increasing Reynolds number.

(a)   (b)
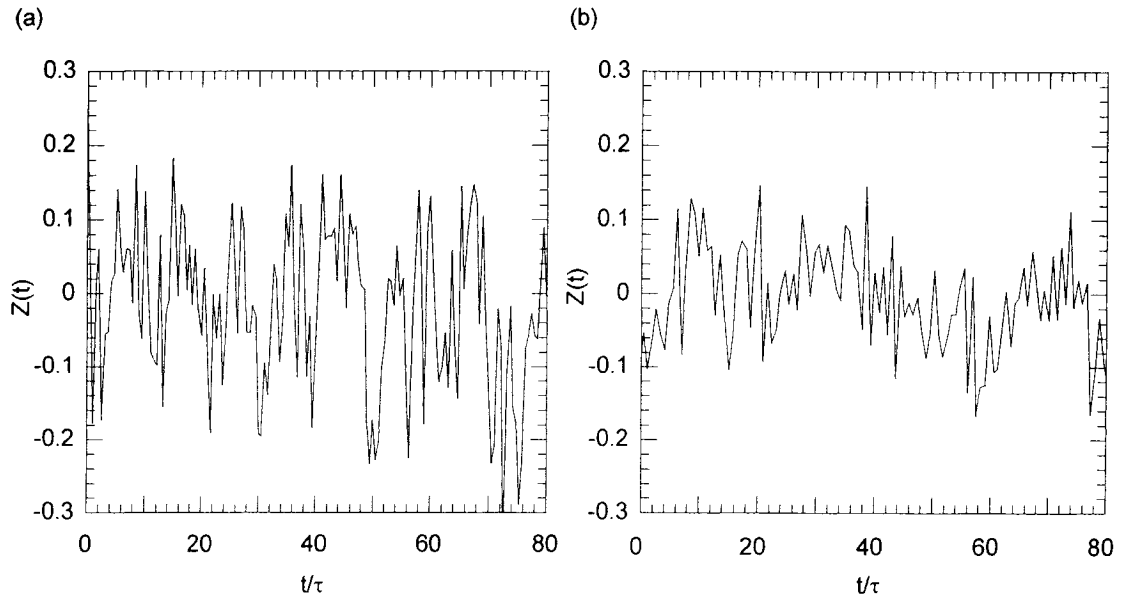
Figure 6.2: Normalized concentration difference time series, r/d = 0.
(a) Re = 900 and (b) Re = 10600.

The time series depicted in Figure 6.2 also provide insight into the physical scales at which differential diffusion effects are manifested. In each of these plots, time is normalized by the Kolmogorov timescale (at its respective Reynolds number). At both the low and high Reynolds numbers, Z is often non-zero for time periods greater than the Kolmogorov timescale. This indicates that differential diffusion effects are present at scales larger than the Kolmogorov scale, even when the Reynolds number is above that of the mixing transition.

Instances of Z remaining non-zero, for times greater than the Kolmogorov scale, is consistent with the findings of Saylor and Sreenivasan (1998). Their experiments were conducted with Schmidt number ratios of approximately 4 and 18. Their tests conducted with a Schmidt number ratio of approximately 4 utilized dyes with Schmidt numbers similar to those of the present work (disodium fluorescein, Sc = 1200, and basic blue 3, Sc = 4400) while their tests performed with a Schmidt number ratio of approximately 18 had one fluorescent dye (fluorescein dextran, Sc = 77000) with a much larger Schmidt number than the fluorescent dyes employed herein and one with a similar Schmidt

93

number (basic blue 3, Sc = 4400). Saylor and Sreenivasan also performed their experiments at a lower Reynolds number of 430, and took their measurements further downstream of the nozzle exit, at x/d = 147. For each Schmidt number ratio, they also found instances when Z was non-zero for times greater than the Kolmogorov timescale. As might be expected, they observed more instances of this phenomenon for the larger Schmidt number ratio.

6.1.2 R.M.S. Fluctuations of the Normalized Concentration Difference

The r.m.s. value of the normalized concentration difference, $Z_{rms} \equiv \langle Z^2 \rangle^{1/2}$, is often used to quantify differential diffusion effects, as it gives an indication of their intensity. By definition, the average value of Z is zero, $\left(\langle Z \rangle = \left\langle \dfrac{C_1}{\langle C_1 \rangle} - \dfrac{C_2}{\langle C_2 \rangle} \right\rangle = \dfrac{\langle C_1 \rangle}{\langle C_1 \rangle} - \dfrac{\langle C_2 \rangle}{\langle C_2 \rangle} = 0 \right)$. However, Z fluctuates around zero, as was observed in Figure 6.2. Therefore, the r.m.s. value of the fluctuations provides an indication of the magnitude of its fluctuations.

The normalized concentration difference, and thus Z_{rms}, has contributions from a range of scales (from the integral scale down to the Batchelor scale). However, since the Batchelor scale was not resolved in these experiments, Z_{rms} was only calculated up to the Kolmogorov scale by integrating the spectrum of the normalized concentration difference, $E_Z(\kappa_l \eta)$ (where κ_l is the longitudinal wavenumber), from $\kappa_l \eta = 0$ to $\kappa_l \eta = 1$. This provided a consistent measurement of Z_{rms}, and thus enabled a comparison of the values of Z_{rms} for the different experimental conditions. Given that the measurements are only up to the Kolmogorov scale, the values of Z_{rms} in this study will be underestimated.

A typical spectrum of Z is plotted in Figure 6.3.
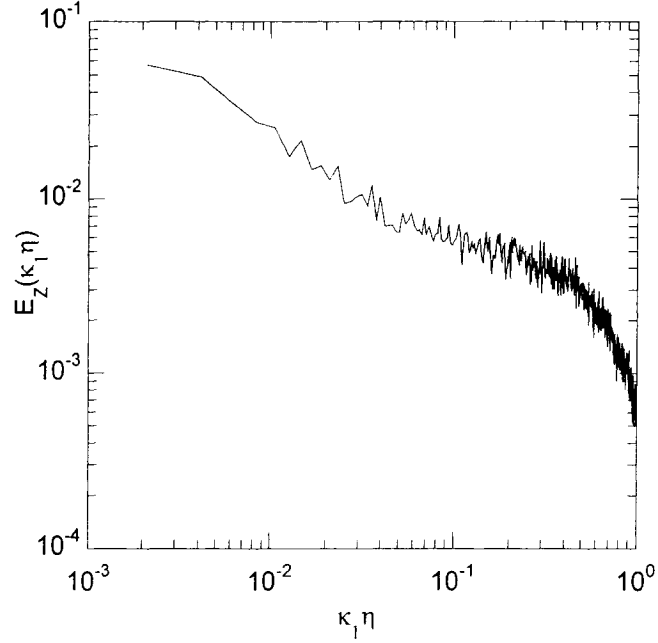
Figure 6.3: Normalized concentration difference spectrum, $E_Z(\kappa_1\eta)$, at r/d = 0 and Re = 10600.

Integration of this spectrum over all wavenumbers will yield a quantitative value for Z_{rms}:

$$Z_{rms} = \langle Z^2 \rangle^{1/2} = \left(\int_0^\infty E_Z(\kappa_1)d\kappa_1 \right)^{1/2}. \tag{6.1}$$

However, due to the limitations of the present apparatus, $E_Z(\kappa_1)$ was only determined up to the Kolmogorov microscale. Therefore, the surrogate of Z_{rms} measured herein is:

$$Z_{rms,meas} = \langle Z^2 \rangle^{1/2}_{meas} = \left(\int_0^{2\pi/\eta} E_Z(\kappa_1)d\kappa_1 \right)^{1/2}. \tag{6.2}$$

All the presented values of $Z_{rms,meas}$ in the rest of this thesis were calculated according to the above definition. For simplicity, this notation will be dropped and Z_{rms} will be substituted.

The Reynolds number dependence of Z_{rms}, on the jet centreline, is depicted in Figure 6.4. Each Z_{rms} value in this figure was determined by averaging multiple Z_{rms} values, from separate experiments at each Reynolds number. The corresponding error

bar at each location is ± 1 standard deviations of these Z_{rms} values (and centred on the average Z_{rms}). From this plot, it is evident that Z_{rms} decreases with increasing Reynolds number. Nevertheless, even at the highest Reynolds number studied (Re = 10600) differential diffusion effects are still significant, as Z_{rms} = 0.064.
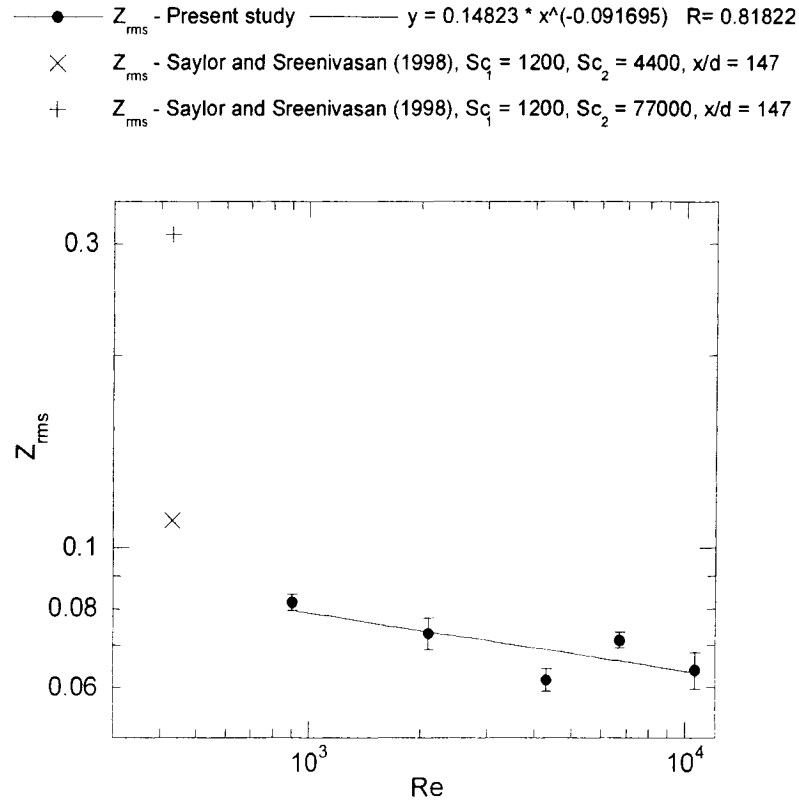
Figure 6.4: Reynolds number dependence of Z_{rms} from the present study and Saylor and Sreenivasan (1998), r/d = 0.

The results from the present study in Figure 6.4 are consistent with the smaller Z_{rms} value obtained by Saylor and Sreenivasan (1998) for $Sc_2/Sc_1 \approx 4$. First, recall that their jet Reynolds number was 430 and their measurements were taken further downstream of the jet exit, at x/d = 147, than the present study (x/d = 50). At this lower Reynolds number they found Z_{rms} = 0.11 when using a jet with similar Schmidt number dyes (Sc_1 = 1200 and Sc_2 = 4400) to those employed herein. This result is not inconsistent with an extrapolation of the present results to lower Reynolds numbers. However, Saylor and Sreenivasan's estimate of Z_{rms} is different than that of the present work, as they resolved all scales down to the Batchelor scale (and consequently measured a true Z_{rms}). There are therefore two different parameters, resolution and measurement

96

location, between this study and Saylor and Sreenivasan (1998). Z_{rms} can be expected to decrease with downstream position. Smith *et al.* (1995a) observed this phenomenon in their turbulent jet of H_2/CO_2 for x/d varying from 15 to 60 and Reynolds numbers ranging from 1000 to 64000. On the other hand, there are unresolved contributions to Z_{rms} at scales smaller than the Kolmogorov scale in the present study. These two factors may offset each other and lead to the agreement between Z_{rms} from Saylor and Sreenivasan (1998) and the extrapolation of the results presented herein. Saylor and Sreenivasan also performed other experiments under the same conditions, except replacing their Sc = 1200 dye with fluorescein dextran (Sc = 77000). Under these conditions, they observed an increase in differential diffusion effects, and found Z_{rms} = 0.305. This higher value of Z_{rms} is expected given the larger difference in Schmidt numbers (see section 3.1).

The best fit line in Figure 6.4 is a power law indicating that Z_{rms} scales as $Z_{rms} \propto Re^{-0.09}$. This value is closer to the $Z_{rms} \propto Re^{-0.15}$ prediction of Fox (1999) than both the $Z_{rms} \propto Re^{-0.25}$ prediction of Kerstein *et al.* (1995) and the $Z_{rms} \propto Re^{-1.0}$ prediction of Bilger and Dibble (1982). However, recall that the predictions of Kerstein *et al.* (1995) and Bilger and Dibble (1982) apply to the true Z_{rms}, calculated over all scales, while in this work, Z_{rms} was only calculated up to the Kolmogorov scale. Nonetheless, the contributions to Z_{rms} at scales smaller than the Kolmogorov scale should remain constant as the Reynolds number increases since the ratio of the Batchelor scale to the Kolmogorov scale only depends on Schmidt number.

Smith *et al.* (1995a) also found differential diffusion effects to decrease with increasing Reynolds number in their non-reacting turbulent jets. While they found z_{rms} to decrease, they were unable to determine a scaling for this decrease. Spatial resolution may have factored into their lack of an observed scaling of z_{rms}. They presented z_{rms} values calculated by assuming that they had resolved all scales, down to the Batchelor scale. However, it is not certain that they were able to resolve the Batchelor scale at each Reynolds number and downstream location, as they discussed. They used the following relation, given by Dowling (1988), to determine the Batchelor scale in their jet:

$$\eta_B = 0.38 C_{B1}(x - x_0) Re^{-3/4} Sc^{-1/2}. \tag{6.3}$$

The true value of $C_{B/}$ (a constant) is unclear. Four different studies (Dowling 1988, Dowling and Dimotakis 1990, Dowling 1991, and Buch 1991) have found three different values for $C_{B/}$. Smith *et al.* (1995a) estimated that they resolved the Batchelor scale in each instance, except at one downstream position for Re = 64000, by assuming that $C_{B/}$ = 12.5, as determined by Dowling (1988) and Dowling and Dimotakis (1990). As Smith *et al.* (1995a) noted, if they had used Dowling's (1991) value of 2.5, then they would have only resolved the Batchelor scale at lower Reynolds numbers. Therefore, it is possible that Smith *et al.* (1995a) did not resolve the smallest scales in each instance and may have underestimated z_{rms}. If this was the case, it may explain why they were unable to develop a scaling relation for z_{rms} with Reynolds number, as their measured values would have been calculated and compared over different ranges of scales.

At each Reynolds number, measurements were collected at radial positions which began at the centreline and extended to the edge of the jet. Figure 6.5 displays the radial dependence of Z_{rms} at a Reynolds number of 10600. The error bars in this figure were calculated using the same method as those depicted in Figure 6.4. As can be seen in the plot, Z_{rms} increases with increasing radial position from the centre of the jet.
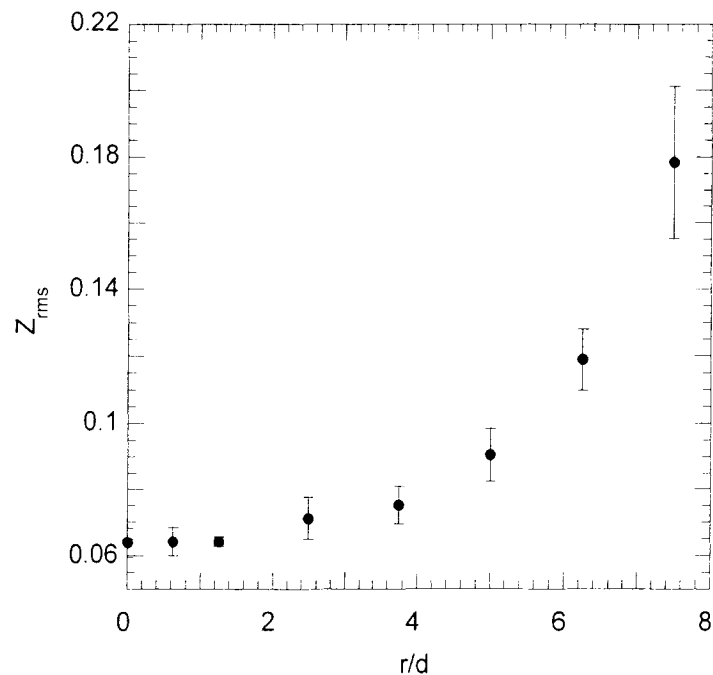

Figure 6.5: Radial variation of Z_{rms}, Re = 10600.

Increases in differential diffusion with radial position have also been observed by other researchers. Bilger and Dibble (1982) first predicted an off-axis peak of Z_{rms} in a turbulent jet of hydrogen/propane issuing into a co-flowing stream of air. In their simulations, their jet had an exit velocity of 40 m/s, while the co-flowing stream of air had a velocity of 10.7 m/s. Under these conditions, they obtained an off-axis peak of Z_{rms} at three axial locations downstream of the jet exit (x/d = 10, 20, and 30). They also observed a decrease in Z_{rms} with downstream position, as they obtained an off-axis peak of approximately 0.004 at x/d = 10, which decreased to about 0.002 at x/d = 30. This peak seemed to shift slightly with downstream position, as it occurred at r/d just below 2 at x/d = 10 and r/d just above 2 at x/d = 30.

Kerstein (1990) obtained radial profiles of Z_{rms}, in his simulations of a turbulent jet of H_2 and propane, which were qualitatively similar to Bilger and Dibble (1982). Kerstein's (1990) profiles were at two Reynolds numbers (Re = 5000 and 20000) and four axial locations (from x/d = 5 to 20). At each Reynolds number, Z_{rms} displayed an off-axis peak that was greatest closest to the jet exit. For instance, the peak of Z_{rms} was over 0.05 at x/d = 5 and approximately 0.025 at x/d = 20 for the jet at Re = 5000. The same trend was observed at Re = 20000. The magnitude of Z_{rms} also decreased with downstream distance at this Reynolds number, as the off-axis peak was just under 0.05 at x/d = 5, and under 0.025 at x/d = 20. Kerstein also observed a shift in the peak with downstream position. At both Reynolds numbers, the peak occurred at r/d ~ 1 at x/d = 5 and at r/d slightly below 3 at x/d = 20.

An off-axis peak of Z_{rms} (observed by Bilger and Dibble (1982) and Kerstein (1990)) was not observed in the present work. As radial position increases, Z_{rms} must eventually reach a local maximum and decrease to zero in the ambient fluid outside of the jet. Therefore, if the experiments herein were conducted at greater radial positions, then this trend in Z_{rms} would most likely have been observed. Measurements were not made at radial locations greater than r/d = 7.5 due to the intermittent nature of the jet near its edges. Useful results could not be obtained past this location as it would have been necessary to take longer data sets. If longer data sets were acquired, dyed fluid would have been re-entrained into the jet and impacted the results. It is worth noting, however, that Bilger and Dibble (1982) and Kerstein (1990) observed a shift in their off-axis peak

of Z_{rms} to greater radial positions with increased downstream distance. Since the present results were obtained further downstream than the aforementioned simulations, the peak of Z_{rms} herein should occur further from the centreline than in the previous studies.

Smith *et al.* (1995a) also noticed an increase in differential diffusion effects with radial position, however they did not an observe off-axis peak, in their turbulent jet experiments. They conducted their tests in a jet of H_2/CO_2 issuing into air. At jet Reynolds numbers of 2000 and 8000, they presented histograms of differences in mixture fractions which were symmetric along the centreline and asymmetric away from the axis. These histograms will be discussed in more detail in section 6.1.4. However, they did attribute the off-axis asymmetries to increases in differential diffusion effects.

An increase in differential diffusion effects with increased radial position from the jet centreline was observed at each Reynolds number studied, not only at Re = 10600 (see Figure 6.6). In this figure, radial profiles of Z_{rms} are presented for Re = 900, 2100, 4300, 6700 and 10600. At each Reynolds number, Z_{rms} increased with increasing distance from the centre of the jet cross-section. These results were also plotted normalizing each Z_{rms} value by its respective centreline value (not shown). The data collapsed well up to approximately r/d = 3; however, beyond this position, there were noticeable differences in normalized values.
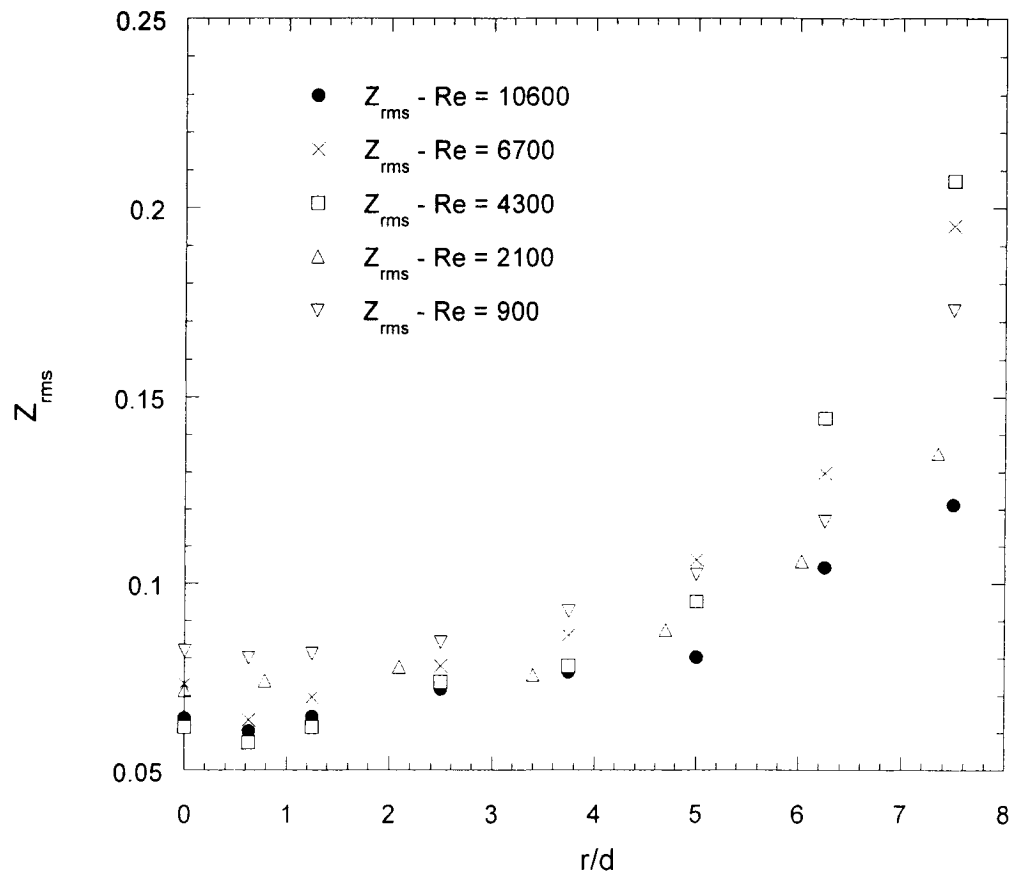
Figure 6.6: Radial variation of Z_{rms} at all five Reynolds numbers studied.

The data in Figure 6.6 is re-plotted in Figure 6.7 to show the Reynolds number dependence of Z_{rms} with radial position. Note that at each successive radial position the Z_{rms} data is shifted up by 0.02 units from the previous radial position. At each radial location, Z_{rms} is weakly decaying with Reynolds number. However, a trend in the power law was not observed with increased radial position.
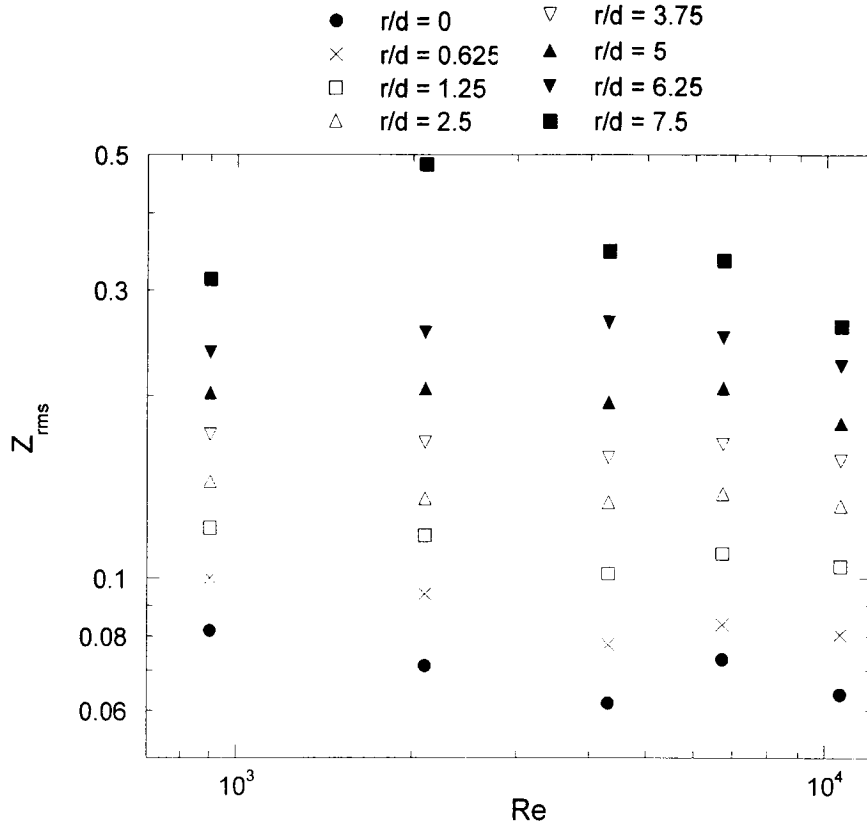
Figure 6.7: Reynolds number variation of Z_{rms} at each radial position. Each radial position after $r/d = 0$ is shifted up 0.02 units from the previous position.

6.1.3 Normalized Concentration Difference Spectra

As alluded to in the previous section, the spectrum of the normalized concentration difference, or difference spectrum, provides insight into differential diffusion. The difference spectrum not only gives an indication of the intensity of differential diffusion effects, as shown in section 6.1.2, but it can also be used to determine the scales at which differential diffusion occurs. Therefore, spectra of the normalized concentration difference were studied for each experiment conducted in this work.

For the previously discussed reasons, the spectrum of the normalized concentration difference was only calculated up to $\kappa_1\eta = 1$, thus only quantifying differential diffusion effects at scales equal to or larger than the Kolmogorov scale.

Measured $E_Z(\kappa_1\eta)$ at two different radial positions for Re = 10600 are plotted in Figure 6.8. As expected, and consistent with the Z_{rms} values presented in section 6.1.2,

the spectrum at r/d = 6.25 lies above the spectrum measured at the centreline. Similar results can be seen at Re = 900 in Figure 6.9. Again the off-axis difference spectrum falls above the spectrum measured at the centreline. Differential diffusion effects are present at scales larger than the Kolmogorov scale in all instances, as is evident from $E_Z(\kappa_1\eta)$.

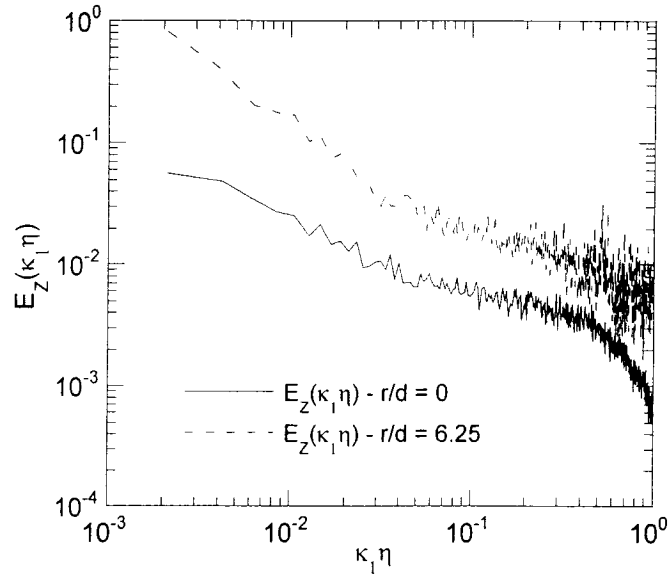

Figure 6.8: Normalized concentration difference spectra, $E_Z(\kappa_1\eta)$.
Re = 10600, r/d = 0 and 6.25.
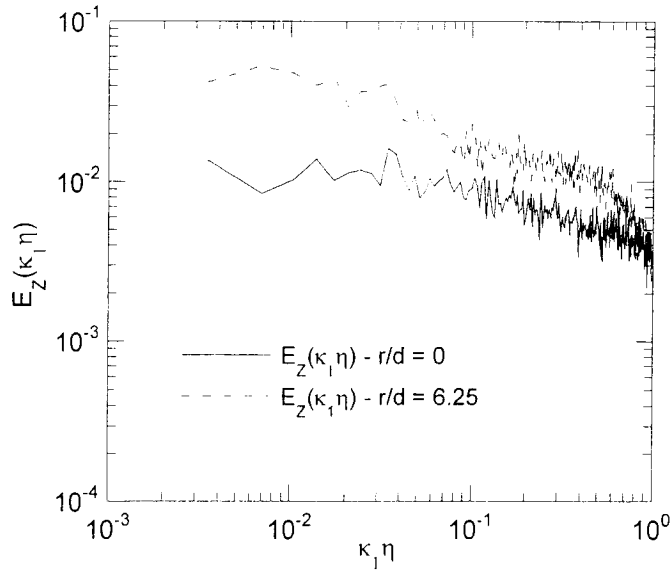
Figure 6.9: Normalized concentration difference spectra, $E_Z(\kappa_1\eta)$.
Re = 900, r/d = 0 and 6.25.

Figure 6.10 replots the centreline spectra at Re = 900 and 10600 from Figures 6.8 and 6.9, respectively. This plot shows that the difference spectrum for the lower Reynolds numbers lies above that for the higher Reynolds numbers. Again, this is expected given the results from section 6.1.2 showing Z_{rms} to be greater for lower Reynolds numbers. To the author's knowledge, these are the first measurements of $E_Z(\kappa_1\eta)$. Therefore, there are no other experimentally measured spectra to compare with. However, these spectra will be compared with ones calculated numerically in section 7.2, where their shape will be discussed in detail.
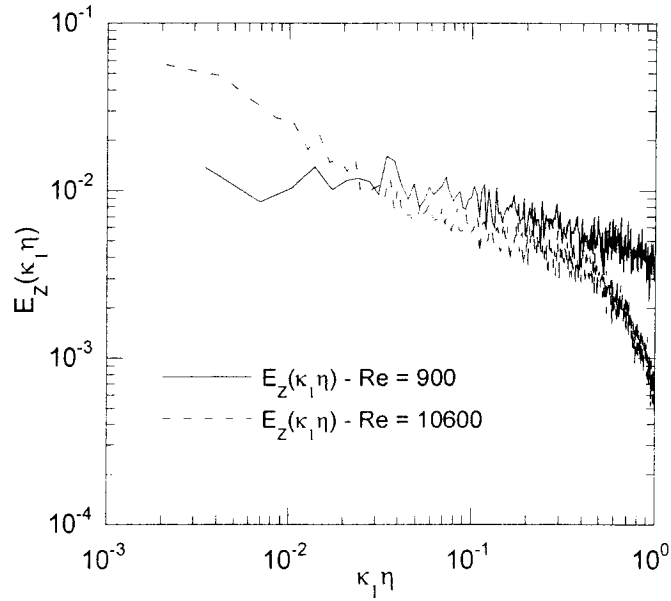
Figure 6.10: Reynolds number comparison of centreline normalized concentration difference spectra, $E_Z(\kappa_1\eta)$. Re = 900 and 10600.

6.1.4 Normalized Concentration Difference PDFs

The PDF of Z can also be used to study differential diffusion effects. To this end, PDFs of Z at various radial positions, for each Reynolds number, were calculated. They will aid in quantifying variations in differential diffusion effects with both Reynolds number and radial position in the jet.

The skewness $\left(S_Z \equiv \dfrac{\langle Z^3 \rangle}{\langle Z^2 \rangle^{3/2}} \right)$ and kurtosis $\left(K_Z \equiv \dfrac{\langle Z^4 \rangle}{\langle Z^2 \rangle^2} \right)$ of each PDF was also calculated. The skewness quantifies the asymmetry of a PDF. Therefore, a positive

104

skewness indicates positive fluctuations of Z are more likely than negative ones. The kurtosis quantifies the importance of the tails of the PDF. Hence, a high kurtosis results from frequent occurrences of large fluctuations (of Z).

PDFs of Z, along with their skewnesses and kurtoses, are shown for two radial positions, at Re = 10600, in Figure 6.11. Figure 6.11(a) is measured at the centreline while Figure 6.11(b) is at a radial position near the edge of the jet (r/d = 6.25). The solid curve in this figure (as with all other solid curves in this section) is a standardized normal Gaussian distribution, $f(V_i) = \dfrac{1}{\sqrt{2\pi}} \exp\left(-\dfrac{V_i^2}{2}\right)$. As can be seen in the figure, the PDF at the centreline is effectively Gaussian ($S_Z \approx 0$, $K_Z \approx 3$), while the off-axis PDF has a slight positive skewness ($S_Z = 0.20$) and is super-Gaussian ($K_Z = 7.65 > 3$).

(a)   (b)
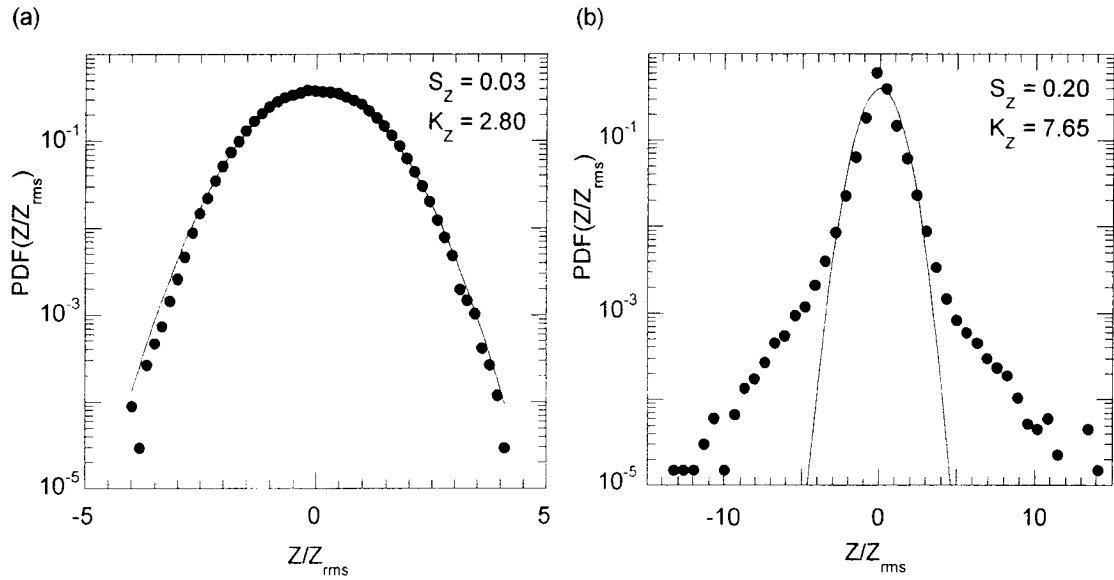
Figure 6.11: Normalized concentration difference PDFs at Re = 10600.
(a) r/d = 0 and (b) r/d = 6.25.

Figure 6.12 shows a radial profile of both S_Z and K_Z for the turbulent jet at Re = 10600. Both S_Z and K_Z increase as the jet is traversed from the centreline to its edges.
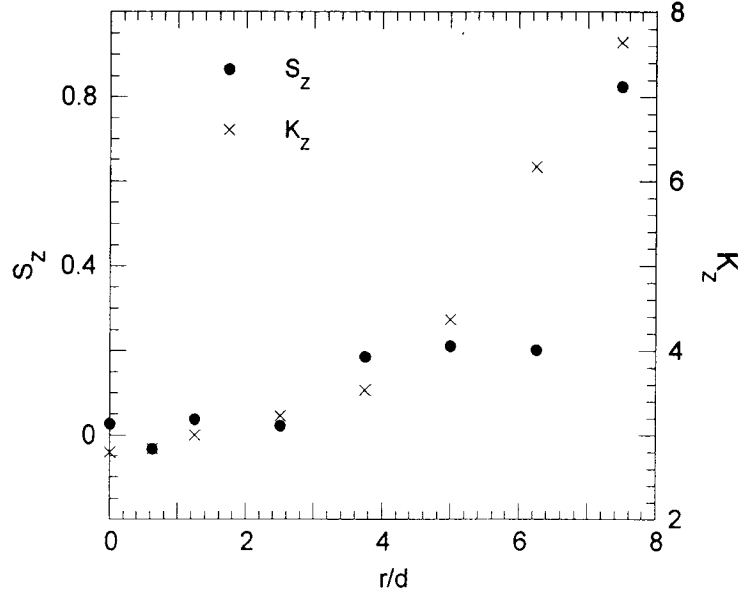
Figure 6.12: Radial profile of the skewness and kurtosis of the normalized concentration difference, Re = 10600.

The trend of increasing S_Z and K_Z with increased radial position was seen at all the Reynolds numbers studied in this work. Figures 6.13 to 6.16 plot the PDFs of Z (at the centreline and a location near the edge of the jet), for Re = 6700, 4300, 2100, and 900. The radial increase in S_Z and K_Z, similar to the results at Re = 10600, can be seen in each figure as the PDF at the off-axis position is super-Gaussian and positively skewed in all cases.

The following hypothesis, first put forth by Kerstein (1990), may explain the positive skewness of Z increasing with radial position. The more diffusive scalar, disodium fluorescein (C_1), will diffuse more rapidly (from a parcel of dyed jet fluid into an adjacent parcel of fluid) than the less diffusive scalar, sulforhodamine 101 (C_2). This result is most pronounced at interfaces between dyed jet fluid and ambient fluid. At these interfaces, the faster diffusion of disodium fluorescein into the ambient fluid leads

to positive values of Z, $\left(Z \equiv \dfrac{C_1}{\langle C_1 \rangle} - \dfrac{C_2}{\langle C_2 \rangle} \right)$. This effect becomes more and more

pronounced as the edge of the jet is approached and "clean" ambient fluid is observed more frequently. These instances of a positive Z lead to PDFs with a positive skewness, as observed. This phenomenon will be discussed further in section 7.1.

106
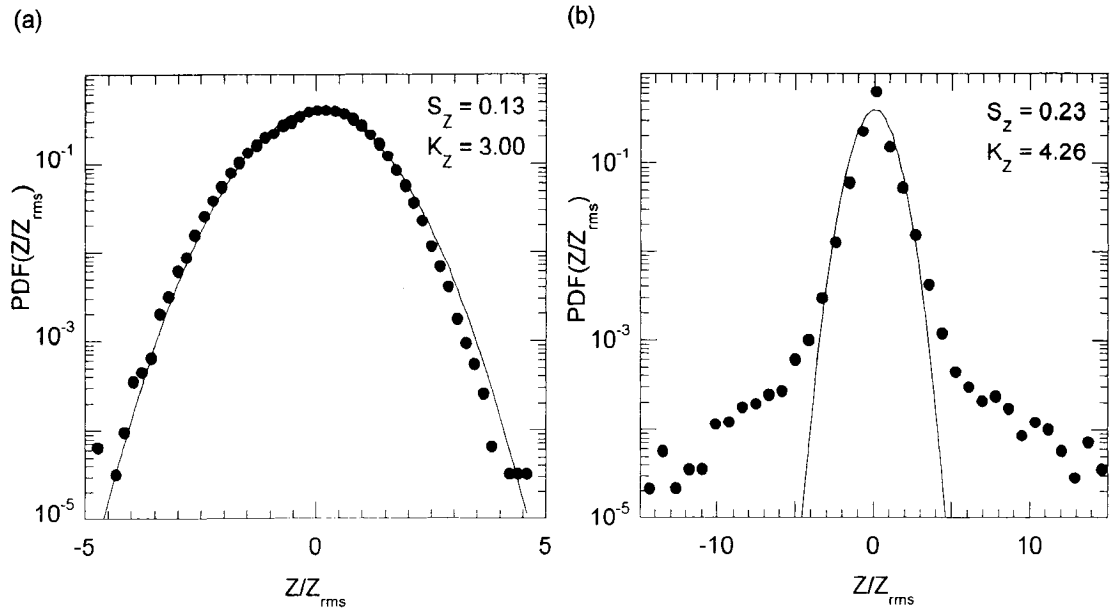
Figure 6.13: Normalized concentration difference PDFs, Re = 6700.
(a) r/d = 0 and (b) r/d = 6.25.
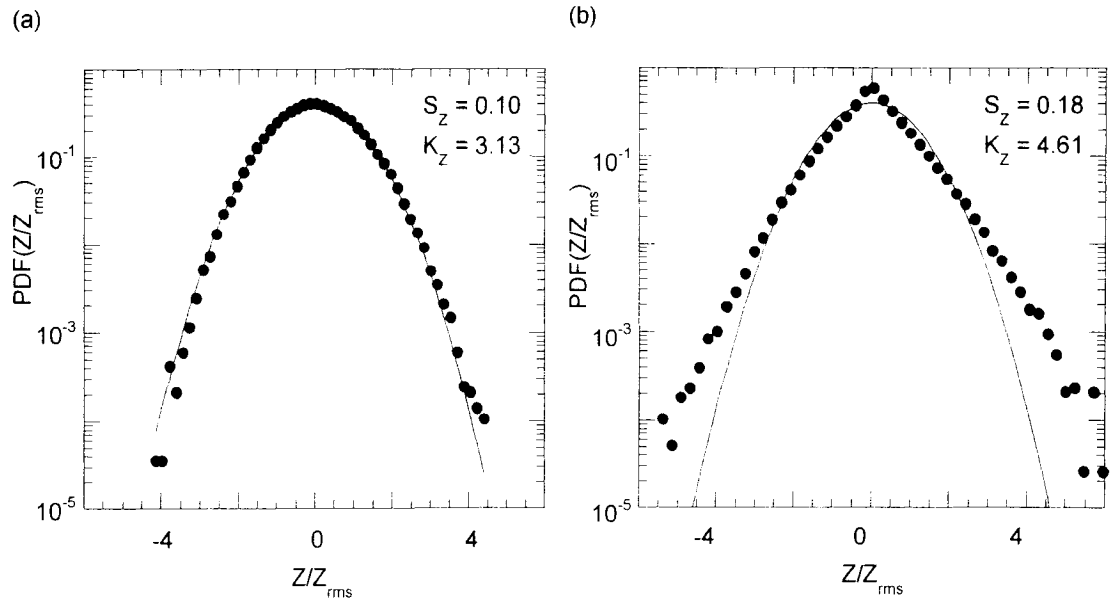
Figure 6.14: Normalized concentration difference PDFs, Re = 4300.
(a) r/d = 0 and (b) r/d = 6.05.
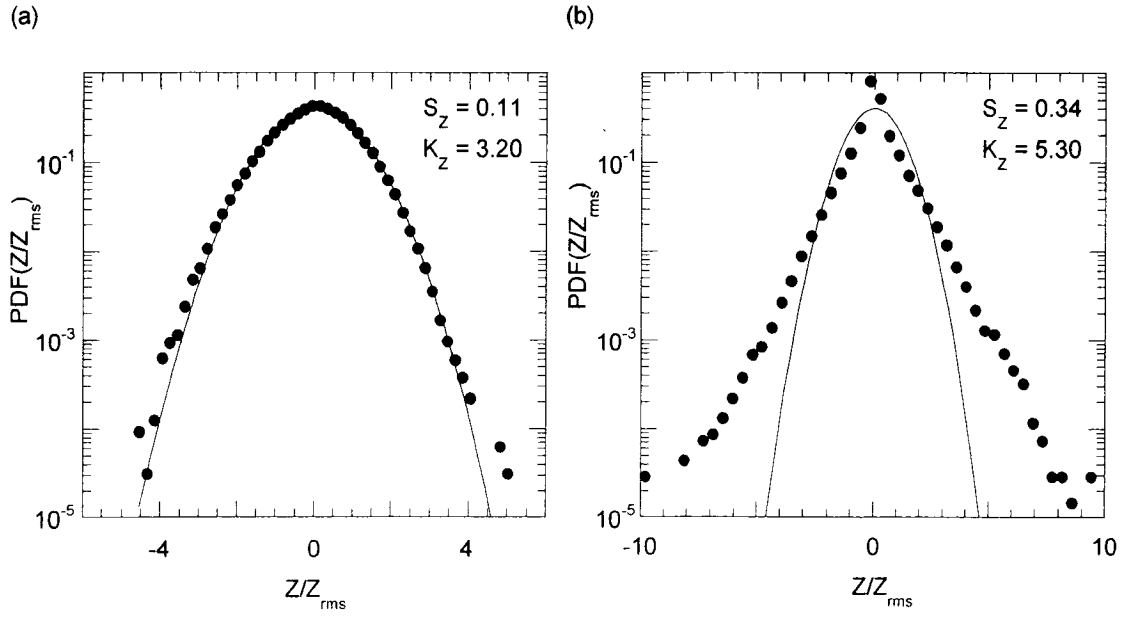
Figure 6.15: Normalized concentration difference PDFs, Re = 2100.
(a) r/d = 0 and (b) r/d = 6.05.
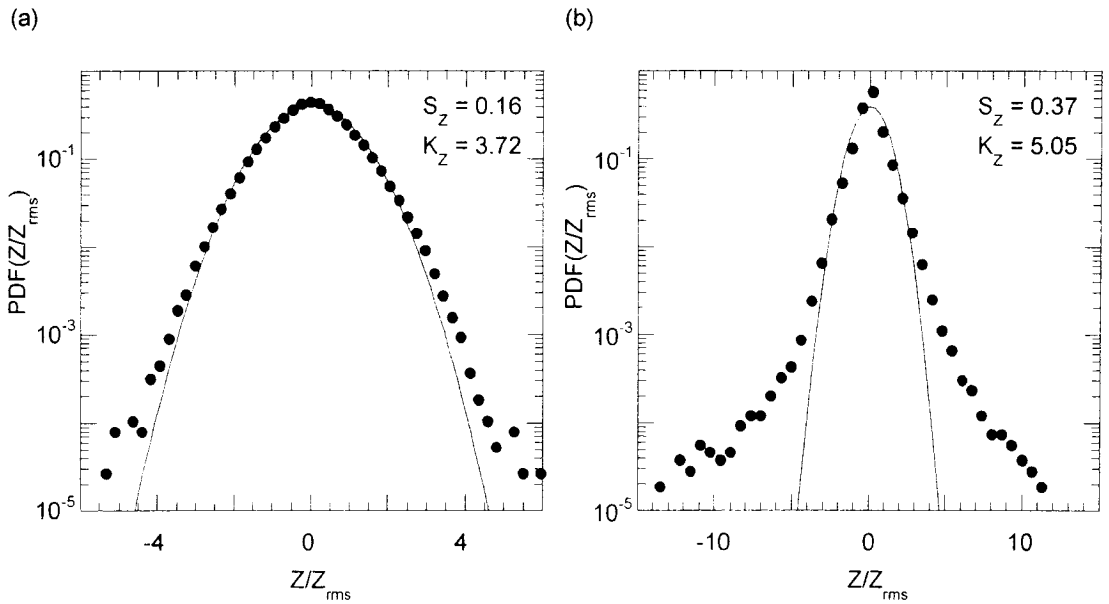
Figure 6.16: Normalized concentration difference PDFs, Re = 900.
(a) r/d = 0 and (b) r/d = 6.25.

As can be seen in the figures, the centreline PDFs are becoming increasingly positively skewed and super-Gaussian as the Reynolds number decreases. K_Z increased from 2.80 at Re = 10600 to 3.72 at Re = 900. This increase in kurtosis indicates more instances of large fluctuations of Z. Meanwhile, S_Z increased from 0.03 for Re = 10600

to 0.16 for Re = 900, an indication of more positive fluctuations in Z as the Reynolds number decreases. This decrease in S_Z with increasing Reynolds number can be attributed to the amount of entrained ambient fluid that reaches the jet centreline. As the Reynolds number increases, the rate of entrainment of ambient fluid decreases. This phenomenon will be discussed in detail in section 7.1; however, it ultimately leads to a more symmetric distribution of Z at higher Reynolds numbers.

When studying differential diffusion, relatively few studies have calculated PDFs of Z. Kerstein (1990) computed PDFs of differences in mixture fractions in his simulations of a jet of H_2 and propane. He presented PDFs at various downstream locations for the jet at Reynolds numbers of 5000 and 20000. At each Reynolds number and downstream location, a PDF was displayed at the centreline and at an off-axis position. At all locations, regardless of Reynolds number or position, Kerstein observed asymmetries in his PDFs. He also noticed that the asymmetries were more pronounced at the off-axis locations. Kerstein (1990) also presented PDFs from the turbulent jet experiments of Kerstein *et al.* (1989). Their measurements were in a turbulent jet consisting of hydrogen and Freon at a Reynolds number of 20000. These measurements were obtained at a downstream distance of 10 diameters from the jet exit. PDFs were presented at three locations: at the centreline and two off-axis positions. Each of them was asymmetric, with an increase in the asymmetry with increased radial distance from the centreline.

Smith *et al.* (1995a) obtained histograms of differences in mixture fractions in their turbulent jet of H_2/CO_2 at Reynolds numbers of 2000 and 8000. At Re = 2000, they presented histograms at the centreline and an off-axis position at two downstream locations, x/d = 15 and 30. At both axial positions, the histograms were symmetric at the centreline and asymmetric at the off-axis location. A similar trend was observed at their higher Reynolds number (Re = 8000). In this instance, they presented histograms at only one axial location, x/d = 15. These histograms were at two radial locations, one just off the centreline and one well off the centreline. Their histogram just off the centreline was symmetric while well off the centreline they obtained an asymmetric histogram. They also observed a difference in their histograms with Reynolds number, as they were less skewed at the higher Reynolds number. However, as they noted, this effect may not have

been physical, but instead due to a decrease in spatial resolution at the higher Reynolds number.

Saylor and Sreenivasan (1998) calculated PDFs of Z at the centreline of their turbulent jet. They obtained PDFs for their Schmidt number ratios of approximately 4 and 18, at a jet Reynolds number of 430. For each Schmidt number ratio, their PDFs appear to be super-Gaussian, though their kurtoses were not computed. Furthermore, their PDFs did not appear to be fully converged, presumably due to a relatively short data set, as the authors noted. However, the data set is long enough to see a difference between the shapes of the two PDFs, as the PDFs for the higher Schmidt number ratio are much wider than the PDFs at the lower Schmidt number ratio.

More recently, Brownell and Su (2004) obtained PDFs of differences in mole fractions in a jet of helium and propane. They showed PDFs calculated along the centreline at four axial positions, spanning from the laminar region near the jet exit and extending into the turbulent region further downstream. They also presented PDFs at various radial positions in the jet, varying from the centreline to the jet edges. In the laminar region, at 7 diameters downstream of the jet exit, they obtained PDFs which were symmetric at the centreline and asymmetric at the off-axis position, indicating a greater occurrence of negative mole fraction differences as compared to positive differences. This trend was also observed further downstream where the jet began to transition to a turbulent flow, 9 diameters downstream from the jet exit. However, in this instance, the off-axis PDFs were less skewed than those in the laminar region. Finally, at 12 diameters downstream, the PDFs were symmetric, regardless if they were obtained at the centreline or at an off-axis location. This result indicated that differential diffusion effects did not vary with radial position in the fully turbulent region of the jet.

Differential diffusion effects can be further understood by studying joint PDFs (JPDFs). Figures 6.17 and 6.18 show contour plots of JPDFs of disodium fluorescein and sulforhodamine 101 at Reynolds numbers of 10600 and 900, respectively. Each figure displays contour plots of the JPDFs at two radial locations, $r/d = 0$ and 6.25. In the absence of differential diffusion, these JPDFs would just be a straight line, which crosses the origin, with a positive slope at a $45°$ angle (which could be considered an "equal-mixing line"). Hence, it is clear that differential diffusion effects are present at both of

these Reynolds numbers and radial positions, as there are contributions to the contour plots at locations off of the equal-mixing line. The different nature of the flow, at the two locations, is also evident from the location of the peaks of the contour lines. The peak of the contour lines in Figure 6.17(a), at r/d = 0, occurs at the average concentration of each scalar (i.e., at $\frac{c_1}{c_{1,rms}} = \frac{c_2}{c_{2,rms}} = 0$). However, in Figure 6.17(b), at r/d = 6.25, the peak of the contour lines is at scalar concentrations below their respective average concentration (i.e., at $\frac{c_1}{c_{1,rms}} < 0$ and $\frac{c_2}{c_{2,rms}} < 0$). This difference can be explained by the intermittency of the flow near the edges of the jet, resulting in frequent occurrences of ambient fluid (containing neither scalar) reaching these locations. In these intermittent regions it is common to observe instances where the scalar concentration is less than the mean concentration. On the other hand, at this Reynolds number (Re = 10600), entrained ambient fluid rarely reaches the centreline (as compared to near the jet edges), and the scalar concentrations are most often at or near their mean value. The same trend occurs at the off-axis location at the lower Reynolds number, Figure 6.18(b). However, the centreline peak of the contour lines, Figure 6.18(a), appears to be (slightly) shifting towards a location of negative scalar fluctuations. This shift is an indication of a change in the flow at the lower Reynolds number, as there are more instances of entrained ambient fluid reaching the centreline.
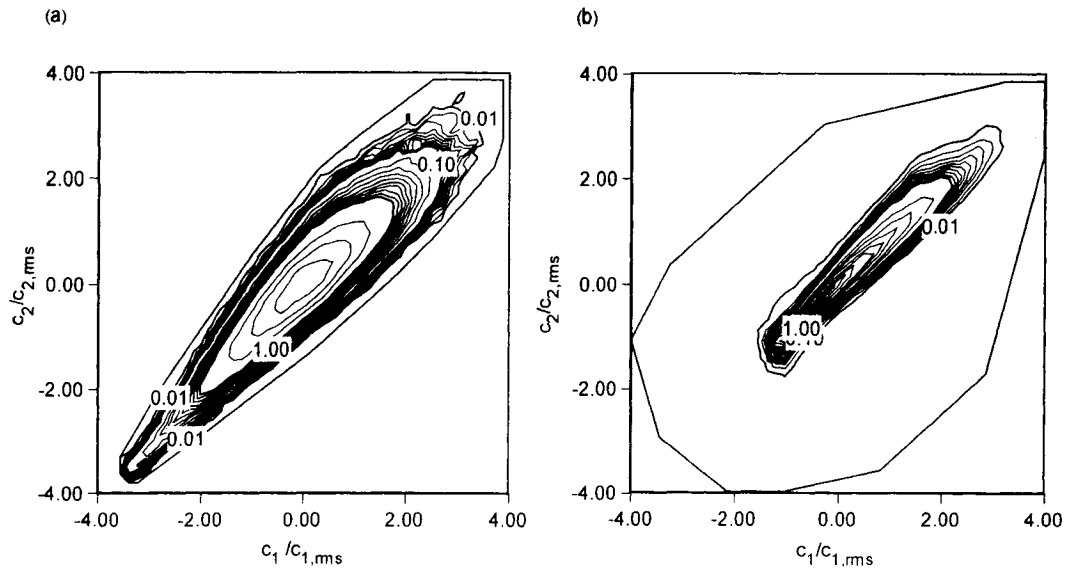
Figure 6.17: Contour plots of the joint PDF of disodium fluorescein, C_1, and sulforhodamine 101, C_2, at Re = 10600. (a) r/d = 0 and (b) r/d = 6.25.
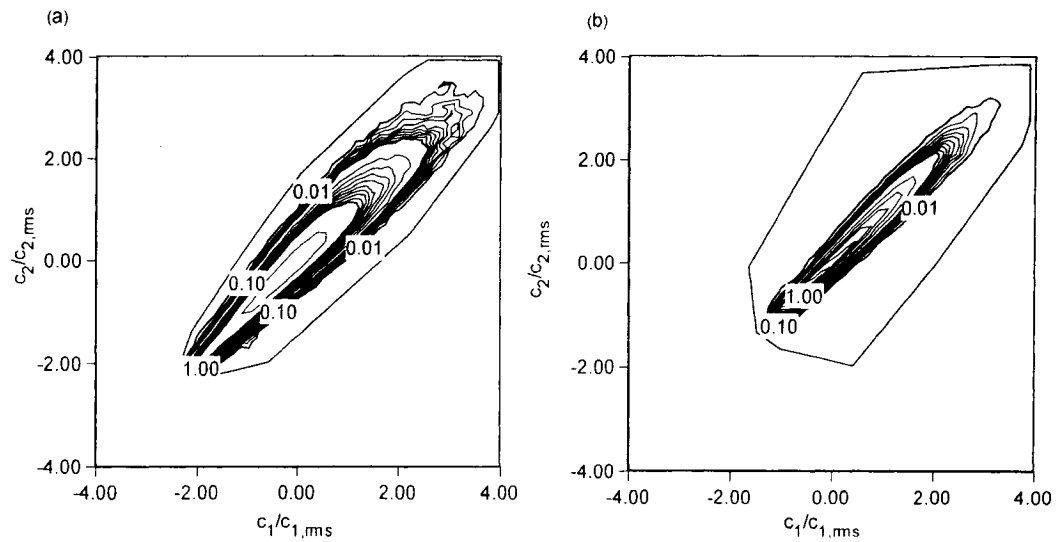
Figure 6.18: Contour plots of the joint PDFs of disodium fluorescein, C_1, and sulforhodamine 101, C_2, at Re = 900. (a) r/d = 0 and (b) r/d = 6.25.

6.1.5 Conditional Expectations

To obtain more insight into the observed differential diffusion effects, conditional expectations were also calculated. Conditional expectations of Z on an individual scalar concentration, $\langle Z \mid C \rangle$, were calculated for both scalars employed herein. These conditional expectations provide an indication of the conditions under which differential

diffusion effects are most prominent. Any instance in which these conditional expectations are non-zero implies that differential diffusion effects are present.

First, conditional expectations of Z on an individual scalar concentration were calculated at the jet centreline, for each Reynolds number. Plots of these conditional expectations are shown in Figure 6.19. Figure 6.19(a) plots $\langle Z \mid C_1 \rangle$ at each Reynolds number at the centreline, while Figure 6.19(b) corresponds to $\langle Z \mid C_2 \rangle$.
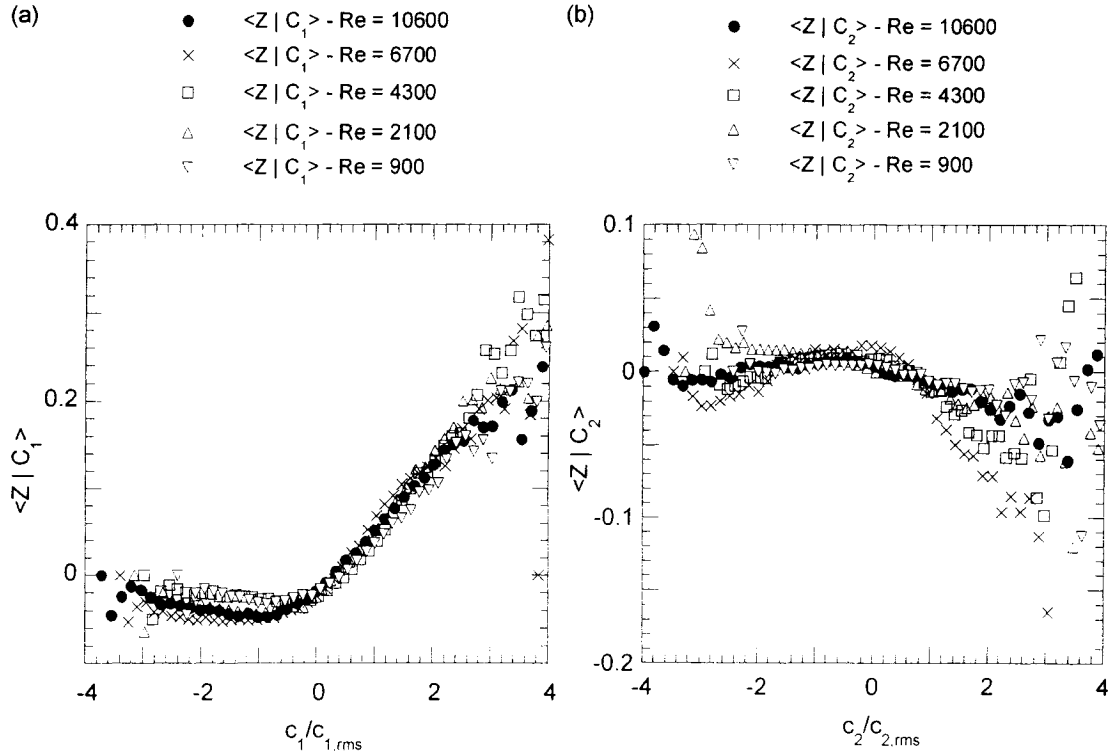
Figure 6.19: Centreline conditional expectations. (a) Z on C_1 (disodium fluorescein, $Sc_1 = 2000$) and (b) Z on C_2 (sulforhodamine 101, $Sc_2 = 5000$).

From Figure 6.19(a), it appears that differential diffusion effects are strongest when there are large positive fluctuations of the more diffusive scalar, disodium fluorescein. In these instances, Z is positive and increases as the positive fluctuations of C_1 increase. A large positive fluctuation in disodium fluorescein, C_1, should result in a positive Z $\left(Z = \dfrac{C_1}{\langle C_1 \rangle} - \dfrac{C_2}{\langle C_2 \rangle} \right)$. Conversely, it appears that Z may tend to negative values when there are large positive fluctuations in sulforhodamine 101, C_2, although this effect is not as pronounced. Regardless, it seems that at the centreline, the concentration of the

113

more diffusive scalar will better predict the possibility of the presence of differential diffusion effects than the concentration of the less diffusive scalar.

Conditional expectations were also calculated for off-centreline locations. Plots of $\langle Z \mid C_1 \rangle$ and $\langle Z \mid C_2 \rangle$ at an off-axis location, $r/d = 6.25$, for each Reynolds number are shown in Figure 6.20. The plots in Figure 6.20(a) correspond to $\langle Z \mid C_1 \rangle$ and the plots in Figure 6.20(b) correspond to $\langle Z \mid C_2 \rangle$. The behaviour of $\langle Z \mid C_1 \rangle$ at this off-axis location appears similar to that along the centreline – differential diffusion effects are most prominent (with positive Z) when there are large positive fluctuations of the more diffusive scalar. From this figure, it also seems that the most prominent off-axis differential diffusion effects occur when there are large negative fluctuations of the less diffusive scalar, sulforhodamine 101. The physical mechanism responsible for these results will be discussed in section 7.1.
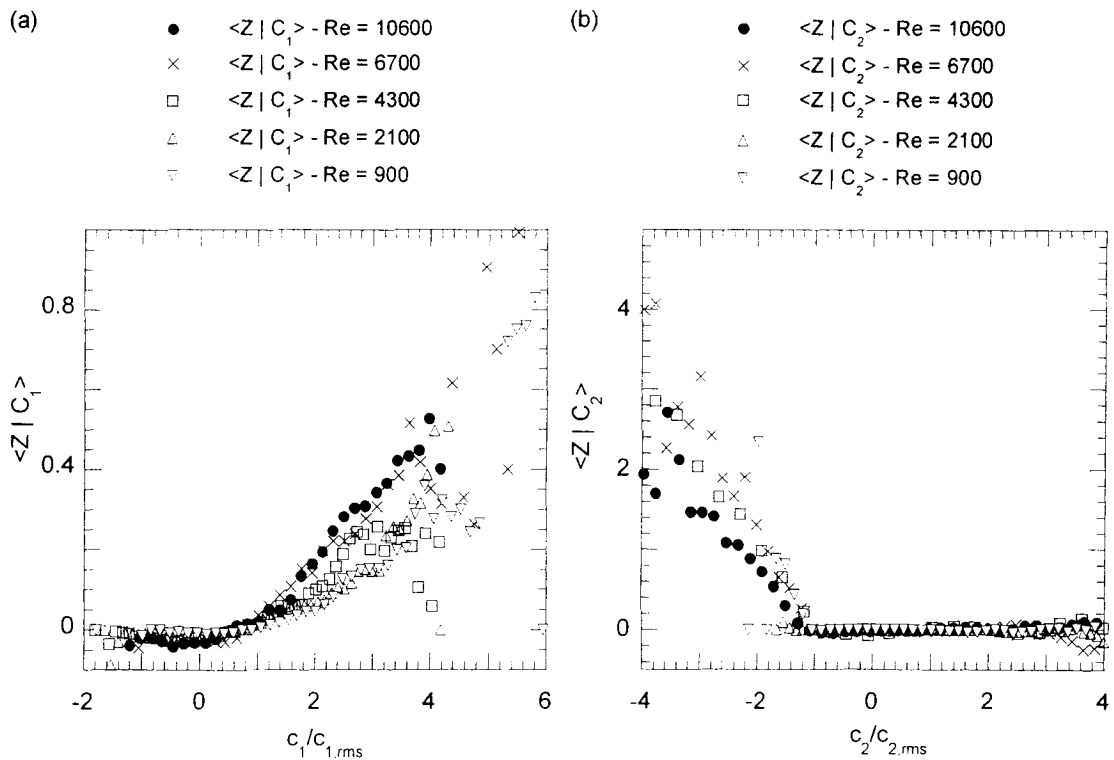
Figure 6.20: Conditional expectations at $r/d = 6.25$. (a) Z on C_1 (disodium fluorescein, $Sc_1 = 2000$) and (b) Z on C_2 (sulforhodamine 101, $Sc_2 = 5000$).

Centreline conditional expectations of an individual normalized scalar concentration on $Z, \langle C / \langle C \rangle \mid Z \rangle$, at each Reynolds number are shown in Figure 6.21. Figure 6.21(a) displays $\langle C_1 / \langle C_1 \rangle \mid Z \rangle$, while Figure 6.21(b) corresponds to $\langle C_2 / \langle C_2 \rangle \mid Z \rangle$.

(a)
- ● $<C_1/<C_1> \mid Z>$ - Re = 10600
- × $<C_1/<C_1> \mid Z>$ - Re = 6700
- □ $<C_1/<C_1> \mid Z>$ - Re = 4300
- △ $<C_1/<C_1> \mid Z>$ - Re = 2100
- ▽ $<C_1/<C_1> \mid Z>$ - Re = 900

(b)
- ● $<C_2/<C_2> \mid Z>$ - Re = 10600
- × $<C_2/<C_2> \mid Z>$ - Re = 6700
- □ $<C_2/<C_2> \mid Z>$ - Re = 4300
- △ $<C_2/<C_2> \mid Z>$ - Re = 2100
- ▽ $<C_2/<C_2> \mid Z>$ - Re = 900

Figure 6.21: Conditional expectations at r/d = 0. (a) $C_1 / \langle C_1 \rangle$ on Z and (b) $C_2 / \langle C_2 \rangle$ on Z.

In general, it appears that large concentration fluctuations are correlated with strong differential diffusion effects. In particular, large positive normalized concentration differences are related to large positive fluctuations of disodium fluorescein, C_1. Similarly, strong negative normalized concentration differences are associated with large positive fluctuations of sulforhodamine 101, C_2. Also, as the Reynolds number increases, the magnitude of the scalar concentration fluctuations, for a given Z, is decreasing.

Finally, the corresponding off-axis conditional expectations to Figure 6.21 are shown in Figure 6.22. Figure 6.22(a) plots $\langle C_1 / \langle C_1 \rangle \mid Z \rangle$ while Figure 6.22(b) corresponds to $\langle C_2 / \langle C_2 \rangle \mid Z \rangle$, both at r/d = 6.25. The trends in this figure are the same as

115

those in Figure 6.21. The main difference is in the magnitudes of the normalized scalar concentrations and of Z. In Figure 6.22, there seem to be larger values of Z, which are related to larger scalar concentration fluctuations.

(a)

● $<C_1/<C_1> \mid Z> - Re = 10600$
× $<C_1/<C_1> \mid Z> - Re = 6700$
□ $<C_1/<C_1> \mid Z> - Re = 4300$
△ $<C_1/<C_1> \mid Z> - Re = 2100$
▽ $<C_1/<C_1> \mid Z> - Re = 900$

(b)

● $<C_2/<C_2> \mid Z> - Re = 10600$
× $<C_2/<C_2> \mid Z> - Re = 6700$
□ $<C_2/<C_2> \mid Z> - Re = 4300$
△ $<C_2/<C_2> \mid Z> - Re = 2100$
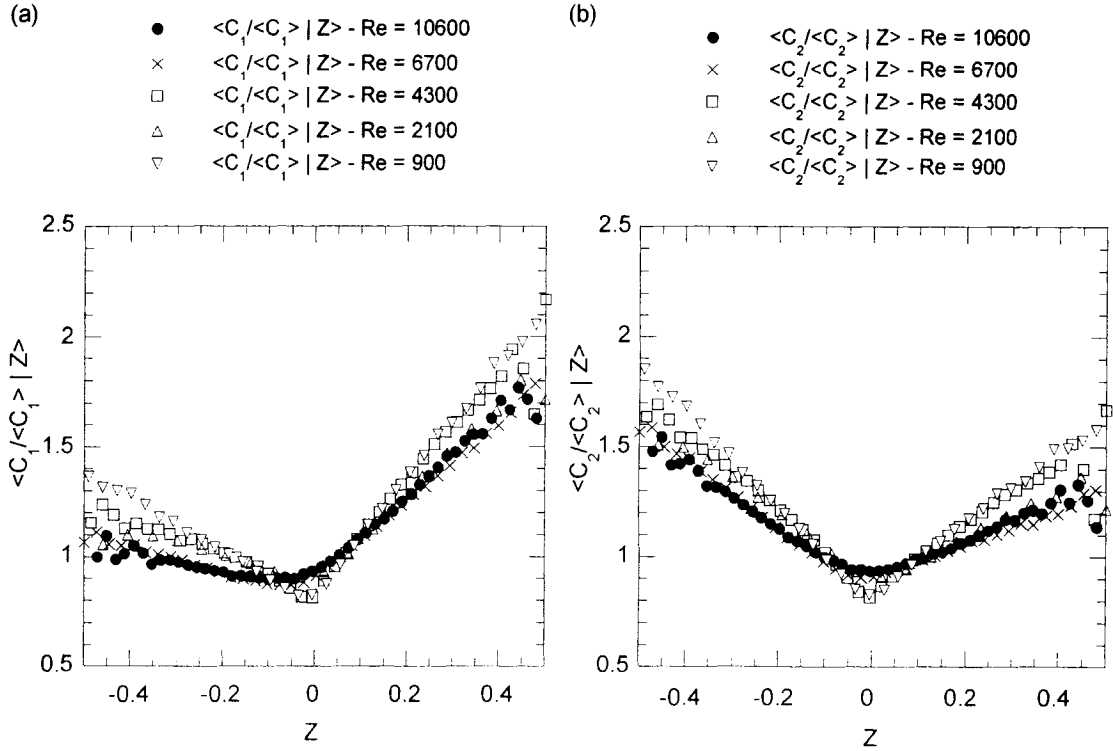▽ $<C_2/<C_2> \mid Z> - Re = 900$
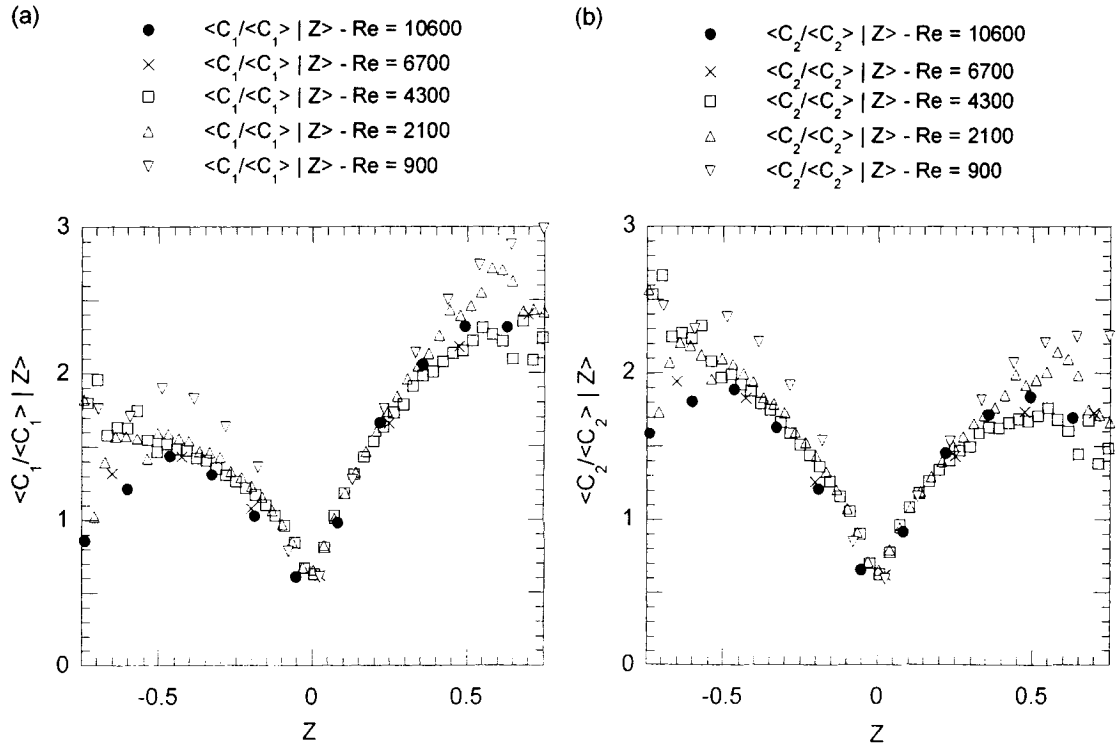
Figure 6.22: Conditional expectations at r/d = 6.25. (a) $C_1/\langle C_1 \rangle$ on Z and (b) $C_2/\langle C_2 \rangle$ on Z.

6.2 Turbulent Background

Experiments were also conducted with the jet issuing into an approximately homogeneous, isotropic turbulent background with zero-mean flow. In the presence of the background turbulence, results were obtained at one Reynolds number (Re = 10600). Experiments were also attempted at a lower Reynolds number (Re = 6700), in which the r.m.s. axial velocity at the measurement location in the turbulent jet was similar to the r.m.s. velocity fluctuations in the turbulent background. As expected, the structure of the jet broke down at this lower Reynolds number. Therefore, useful results could not be obtained, and there will only be a brief discussion of these experiments. At the higher

116

Reynolds number, the results will be compared to the quiescent results to isolate the effects of the turbulent background.

A radial profile of concentration measurements was made in a cross-section of the jet at x/d = 50 and with Re = 10600, similar to that obtained at each Reynolds number in the quiescent background. From these results, the spectrum of the normalized concentration difference, $E_Z(\kappa_1\eta)$, was determined at each radial position. Two of these spectra, at r/d = 0 and 6.25, are displayed in Figure 6.23. The spectrum at the off-centreline location lies above that at r/d = 0, a clear indication of an increase in off-centreline differential diffusion effects. The shape of $E_Z(\kappa_1\eta)$ in this figure, to be discussed further in section 7.2, is similar to those in the quiescent background (see Figures 6.3, 6.8, 6.9, and 6.10) . The spectrum peaking at the low wavenumber end and then decreasing with increasing wavenumber was also observed at all other radial positions, (results not depicted).
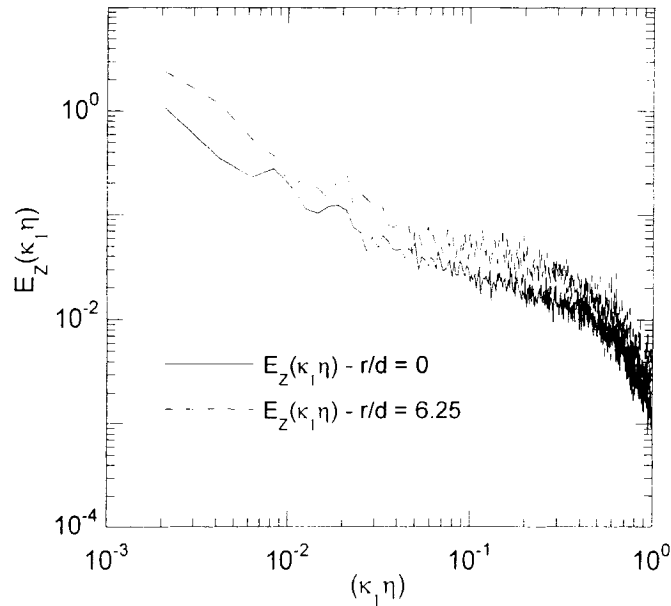
Figure 6.23: Spectra of the normalized concentration difference, $E_Z(\kappa_1\eta)$, in background turbulence, Re = 10600. r/d = 0 and 6.25.

The r.m.s. value of the normalized concentration difference, Z_{rms}, was determined at each radial position. Analogous to the quiescent background, Z_{rms} was calculated by

integrating the measured $E_Z(\kappa_1\eta)$ up to $\kappa_1\eta = 1$. Thus, the presented Z_{rms} in this section are, again, a surrogate of the true value of Z_{rms}. A radial profile of Z_{rms} in the turbulent background along with the corresponding Z_{rms} values (at Re = 10600) in the quiescent background, are displayed in Figure 6.24. Clearly, Z_{rms} increases in the presence of the background turbulence, regardless of radial position. In particular, at the centreline, Z_{rms} doubles from 0.064 in the quiescent background to 0.127 in the turbulent background. It is also worth noting that the centreline value of Z_{rms} obtained in the turbulent background is similar to the values obtained near the jet edges in the quiescent background, where $Z_{rms} = 0.119$ at r/d = 6.25.
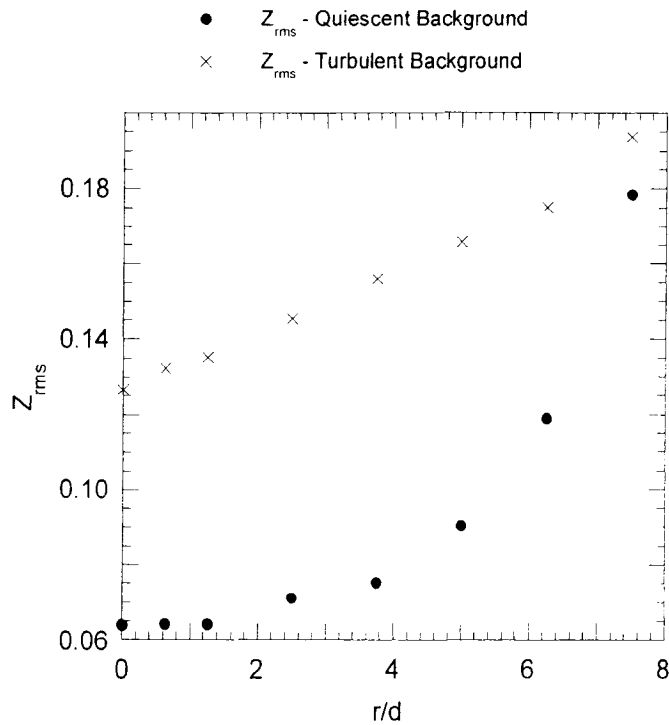
Figure 6.24: Radial profile of Z_{rms} in quiescent and turbulent backgrounds, Re = 10600.

PDFs of Z, along with their respective skewnesses and kurtoses, were also obtained for the background turbulence experiments at Re = 10600. Figure 6.25(a) displays the centreline PDF while Figure 6.25(b) corresponds to the PDF at r/d = 6.25. As in section 6.1.4, the solid curve in these PDFs is a standardized normal Gaussian distribution ($S_Z = 0$, $K_Z = 3$). At each location, the PDF is positively skewed ($S_Z = 0.16$ and 1.24 at r/d = 0 and 6.25, respectively) and super-Gaussian ($K_Z = 6.27$ and 23.94 at

r/d = 0 and 6.25, respectively). It is informative to compare these PDFs to those from the quiescent background, at Re = 10600. Figure 6.11(b), at r/d = 6.25 in the quiescent background, is similar to the PDFs in Figure 6.25. S_Z and K_Z at the centreline in the background turbulence have values which closely match the corresponding values at a radial position of r/d = 6.25 in the quiescent background. These results, coupled with the similar values of Z_{rms} at the centreline in the turbulent background to that near the jet edges in the quiescent background, can be attributed to similar flow conditions in the two regions. This will be discussed in more detail, along with the physical mechanism driving differential diffusion, in section 7.1.

(a)   (b)
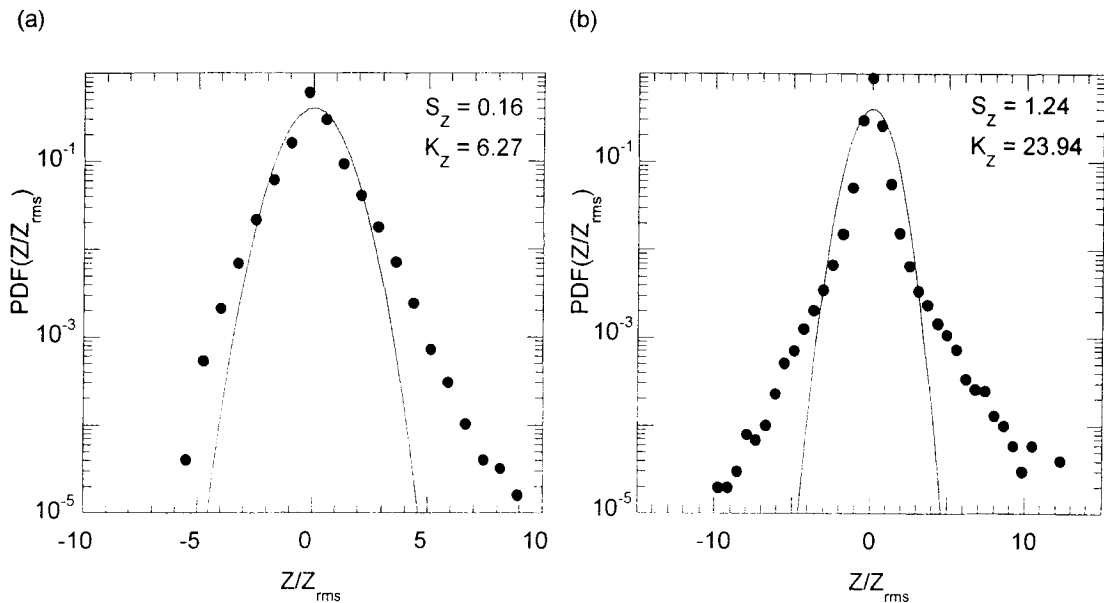
Figure 6.25: Normalized concentration difference PDFs, (a) r/d = 0 and (b) r/d = 6.25. Re = 10600 in background turbulence.

S_Z and K_Z were seen to increase with increased radial position from the jet centreline, as displayed in Figure 6.26. Again, this trend is similar to that observed in the quiescent background (see Figure 6.12). Radial profiles of S_Z and K_Z were only displayed at Re = 10600 in the quiescent background. However, the increase of these quantities with radial position was also observed at the other Reynolds numbers studied, as is evident from the PDFs of Z displayed in Figures 6.13-6.16. These trends will be interpreted in more detail in section 7.1.
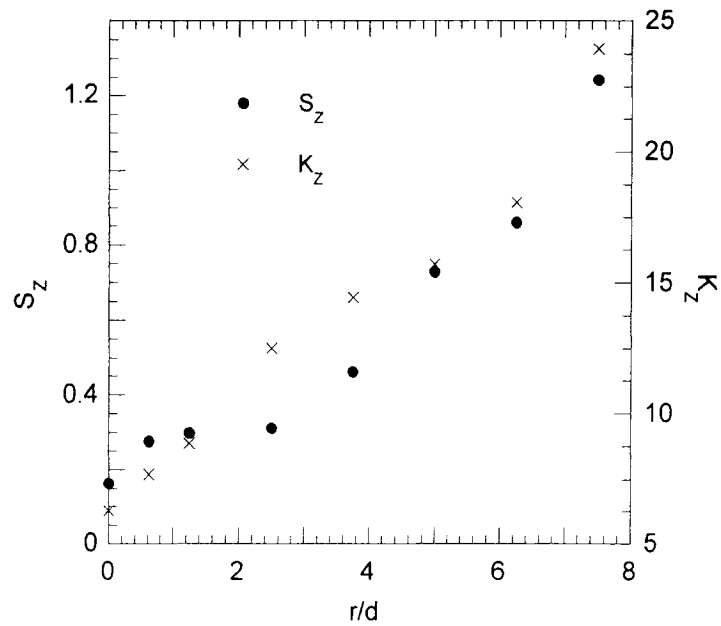
Figure 6.26: Radial profile of skewness and kurtosis of Z in background turbulence, Re = 10600.

JPDFs were also calculated for the experiments with the jet issuing into the turbulent background. Figure 6.27 displays a contour plot of the JPDF of disodium fluorescein and sulforhodamine 101 at the centreline. Since the JPDF does not lie on a straight line that crosses through the origin and has a positive slope with a 45° angle, differential diffusion effects, as already shown, are clearly present. Comparison of this figure with the off-axis JPDF of disodium fluorescein and sulforhodamine 101 in the quiescent background, Figure 6.17(b), is appropriate. These two plots are similar (each with the peak of the contour lines occurring for scalar concentrations less than their respective mean), an indication of the similar structure of the flow (i.e., both displaying an intermittent nature) at the centreline in the turbulent background to locations near the edges of the jet in the quiescent background.

120
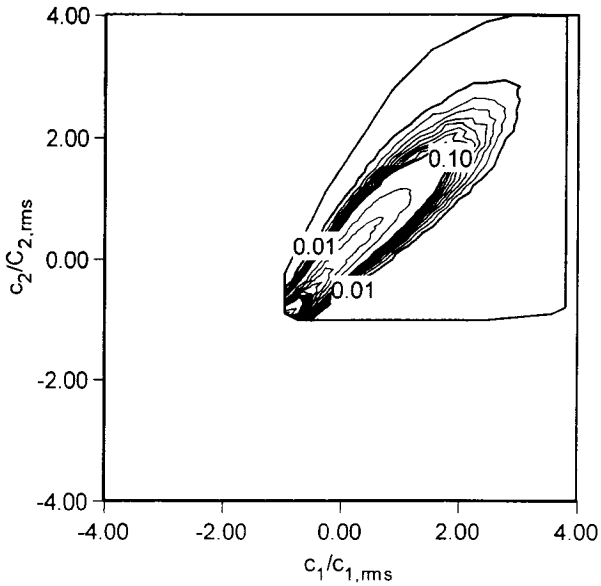
Figure 6.27: Contour plot of the joint PDF of disodium fluorescein and sulforhodamine 101 at the centreline in the turbulent background, Re = 10600.

Centreline conditional expectations of Z on individual scalar concentrations, $\langle Z \mid C \rangle$, are displayed in Figure 6.28. The trend observed in Figure 6.28(a), $\langle Z \mid C_1 \rangle$, is similar to that seen at the centreline, Figure 6.19(a), and near the jet edges, Figure 6.20(a), in the quiescent background. However, Figure 6.28(b), $\langle Z \mid C_2 \rangle$, is only similar to the off-axis $\langle Z \mid C_2 \rangle$ in the quiescent background, Figure 6.20(b). This is another indication of the similar physical mechanism, due to a similar structure of the flow, behind increased differential diffusion in these two regions.

121
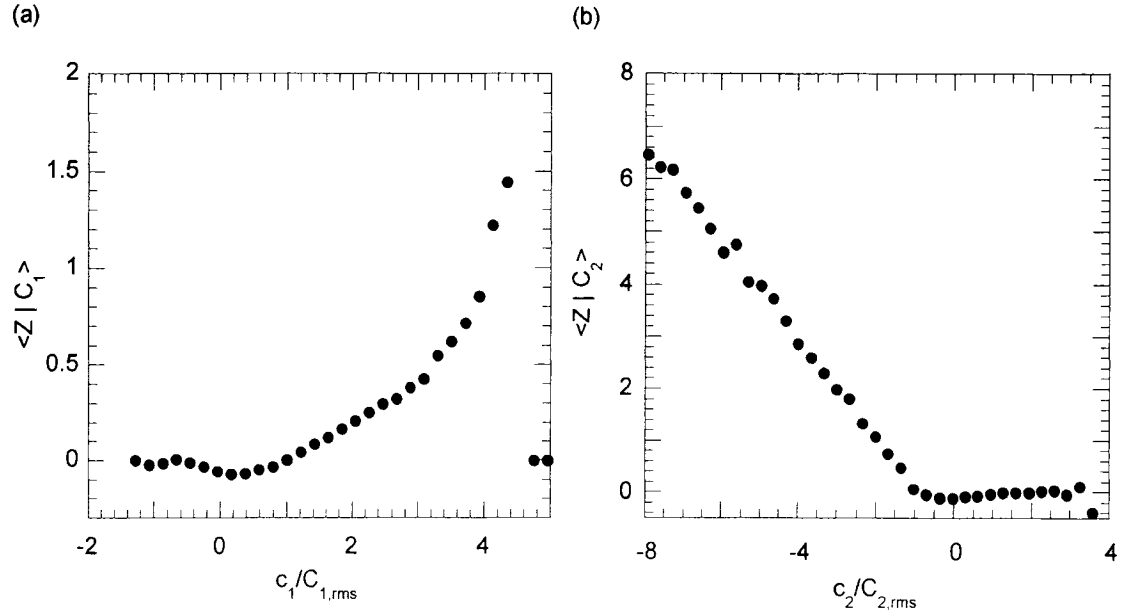
Figure 6.28: Centreline conditional expectations in the turbulent background,
$Re = 10600$. (a) $\langle Z \mid C_1 \rangle$ and (b) $\langle Z \mid C_2 \rangle$.

As previously mentioned, experiments were also attempted, at $Re = 6700$, with the turbulent jet issuing into the quasi-isotropic turbulent background. Sensible results, however, could not be obtained due to the breakdown of the structure of the jet upstream of the measurement location. This phenomenon was expected at this Reynolds number because the magnitude of the r.m.s. velocity fluctuations in the turbulent jet are similar to those in the turbulent background. Guo *et al.* (1999) observed a breakdown of the jet structure to occur when the r.m.s velocity of the background turbulence was 0.125 of the jet centreline velocity. The background turbulence in the experiments of Guo *et al.* was created by an oscillating grid and was similar to this study. Therefore, a similar breakdown in the structure of the jet could be expected. The ratio of the r.m.s velocity of the background turbulence to the mean jet centreline axial velocity, at $Re = 6700$, was calculated to be 0.2 at the measurement location. At this Reynolds number, the r.m.s velocity of the background turbulence was calculated to be 0.125 of the jet centreline velocity at $x/d = 31.7$ (calculations performed with the equations presented in section 5.1 and data in section 5.2), well upstream the measurement location. Hence, the resulting breakdown was expected.

Chapter 7

Discussion

In this chapter, two main topics will be discussed. Firstly, the results of the previous chapter strongly support an increase in differential diffusion as the entrainment of ambient fluid increases. The results pertaining to this effect will be discussed in detail, along with some proposed physical mechanisms behind this increase in differential diffusion. Secondly, there will be a comprehensive discussion on the form of the spectrum of the normalized concentration difference. Previously calculated difference spectra (by means of numerical simulations) will be presented and discussed along with the normalized concentration difference spectra measured herein.

7.1 Increases in Differential Diffusion Due to Ambient Fluid Entrainment

Differential diffusion was seen to increase i) as the Reynolds number decreased, ii) away from the jet axis, and iii) in the presence of quasi-isotropic background turbulence. In each instance, this phenomenon can be related to an increase in the entrainment of ambient fluid, which leads to more cases of interfaces between parcels of jet fluid (containing both scalars) and parcels of ambient fluid (containing neither).

The rate of entrainment of ambient fluid into a turbulent jet decreases with increasing Reynolds number, which also leads to fewer instances of ambient fluid

123

reaching the jet centreline as the turbulence becomes fully-developed (Dimotakis 2000). This phenomenon can clearly be seen in Figure 7.1, which depicts photographs of the downstream evolution of a passive scalar in turbulent jets (at Re ~ 2500 and 10^4) taken by Dimotakis *et al.* (1983), published in Dimotakis (2000). The increase in differential diffusion along the jet centreline, reported in the previous chapter, is due to this effect. Differential diffusion effects, being purely molecular in origin, increase as the difference in molecular diffusion increases. This occurs when the concentration gradients are the largest, i.e., at an interface between a parcel of jet fluid containing both scalars and a parcel of clean, ambient fluid containing neither. At these interfaces, disodium fluorescein will diffuse into the parcel of ambient fluid more rapidly than sulforhodamine 101. This difference in diffusion results in a positive fluctuation of disodium fluorescein in the ambient fluid (and, as the results show, a negative fluctuation of sulforhodamine 101 in the parcel that originally contained only ambient fluid). Consequently, there is a

large positive fluctuation in $Z, \left(Z = \dfrac{C_1}{\langle C_1 \rangle} - \dfrac{C_2}{\langle C_2 \rangle} \right)$, around the interface of jet and ambient
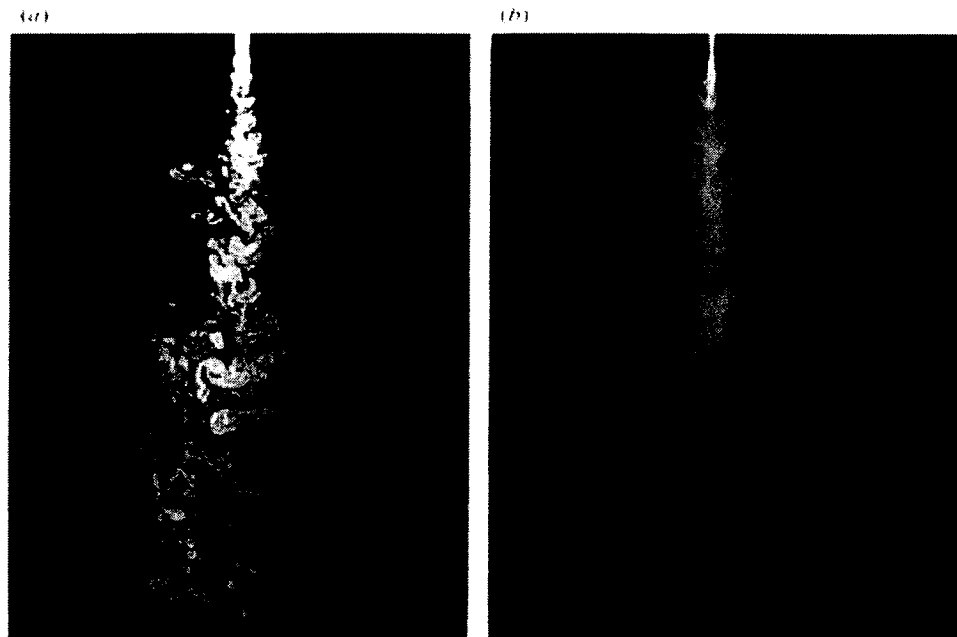
fluids.

Figure 7.1: Comparison of jet entrainment in jets at (a) Re ~ 2500 and (b) Re ~ 10^4. From the data of Dimotakis *et al.* (1983), published in Dimotakis (2000).

Regardless of Reynolds number, the amount of ambient fluid that reaches a given position increases (leading to an increase of interfaces of dyed jet fluid and ambient fluid) with radial position in a turbulent jet. Similar to the trend with decreasing Reynolds number, the increase in differential diffusion effects with radial position can be attributed to this phenomenon. This increase in differential diffusion effects with radial position was first attributed to ambient fluid entrainment by Kerstein (1990). He also argued that the more diffusive scalar would diffuse more rapidly from a parcel of dyed jet fluid into an entrained parcel of ambient fluid containing neither scalar. Smith (1995a) also attributed his observed increase in differential diffusion effects with radial position to an increase in interfaces of dyed fluid with ambient fluid near the edges of the jet.

Increased entrainment of ambient fluid can also be attributed to the increases in S_Z and K_Z (see Figures 6.11 and 6.13 – 6.16). These parameters were shown to increase as the Reynolds number decreased and as the radial position from the jet centreline increased. As mentioned, there was a positive Z at interfaces of dyed jet fluid and ambient fluid. Hence, the observed increases in the skewness and kurtosis of this parameter. It is also worth noting that the increases of both S_Z and K_Z were greater with radial position than with decreasing Reynolds number. This is logical, as the increase in entrained ambient fluid reaching increased radial locations in the jet is much greater than the increase seen at the centreline with decreasing Reynolds number.

The conditional expectations presented in Chapter 6 also support differential diffusion effects increasing due to more interfaces of dyed jet fluid and entrained ambient fluid. Along the centreline, Z is greatest when there are large positive fluctuations of the more diffusive scalar, disodium fluorescein (C_1) (Figure 6.19(a)). However, at this position there is no strong dependence of the magnitude of Z on the concentration of the less diffusive scalar, sulforhodamine 101 (C_2) (Figure 6.19(b)). On the other hand, the conditional expectations near the edge of the jet show that the magnitude of Z is clearly dependent on the concentration of sulforhodamine 101, as well as disodium fluorescein. As seen in Figure 6.20(b), Z can be expected to be positive when there is a large negative fluctuation in the concentration of sulforhodamine 101. The flow is intermittent near the

125

edges of the jet (as compared to the centreline). This results in a large positive fluctuation of disodium fluorescein (which is magnified as compared to similar occurrences at the centreline, since the mean concentration of disodium fluorescein is low in these intermittent regions). On the other hand, the results show that the slower diffusion of sulforhodamine 101 leads to a negative fluctuation of this quantity in the intermittent region.

An increase in differential diffusion effects was also observed when the jet issued into a background consisting of approximately isotropic turbulence with zero-mean flow. Analogous to the increase in differential diffusion effects as the Reynolds number decreased and radial position increased, differential diffusion effects also increased in the presence of background turbulence as there were increased occurrences of interfaces of parcels of ambient fluid and parcels of jet fluid containing both scalars.

Increased entrainment of ambient fluid into a turbulent jet that issues into a turbulent background was expected, as this phenomenon has been observed previously (e.g. Guo *et al.* 1999). Therefore, there were increased occurrences of ambient fluid reaching each radial position in the turbulent background as compared to the quiescent background. Hence, as seen in Figure 6.24, at Re = 10600, the values of Z_{rms} in the turbulent background were greater than in the quiescent background.

The effect of the background turbulence can also be seen by comparing the centreline PDF of Z in background turbulence, Figure 6.25(a), to the off-axis PDF of Z in the quiescent background at Re = 10600, Figure 6.11(b). In each of these instances, the PDFs are alike and the respective S_Z and K_Z have comparable values, both positively skewed and super-Gaussian. The physical explanation for the positive skewness and super-Gaussian nature in the turbulent background is the same as discussed above for the quiescent background. The similarity of the PDFs is an indication of the similar properties of the flow at these two locations.

126

7.2 Discussion of the Normalized Concentration Difference Spectrum

The form of the difference spectrum is of particular interest and is still an unresolved question. In this section, difference spectra calculated from previous numerical studies will be discussed first. Then, $E_Z(\kappa_1\eta)$ presented in the previous chapter will be reviewed and compared to those from the numerical simulations.

Difference spectra were first calculated in the DNSs of Yeung and Pope (1993). These simulations were of stationary homogeneous, isotropic turbulence at a Taylor scale Reynolds number of 38. Each simulation was conducted with two scalars of differing Schmidt numbers, Sc = 0.25, 0.5, or 1, and spanned up to 65 eddy turnover times. The authors imposed conditions such that the initial scalar field was self-similar and they also applied a large-scale forcing to the velocity field. It is worth noting that these conditions resulted in decaying scalar fields. Figure 7.2 displays the time evolution of their difference spectra from a simulation performed with scalars of Schmidt number 0.25 and 1.0. The change in these difference spectra – from one initially increasing with a peak at the high wavenumber end of the spectrum to one peaking at low wavenumbers, then decreasing with wavenumber, after 8 eddy turnover times – is noteworthy. In this figure, the increasing spectrum at early times has an approximate inertial range scaling of κ^3, where κ is the wavenumber, while the decreasing spectra at later times have an inertial range scaling of about κ^{-2}. A possible explanation for this behaviour may be explained in the following quote by Yeung and Pope (1993), "[A]fter the transient period the difference spectrum subsequently becomes dominated by the large scales... It is clear that incoherency develops first at the small scales, but then spreads to the large scales... [D]iffusivity difference has only an indirect effect, and ... (in)coherency propagation across the spectrum is an important mechanism."
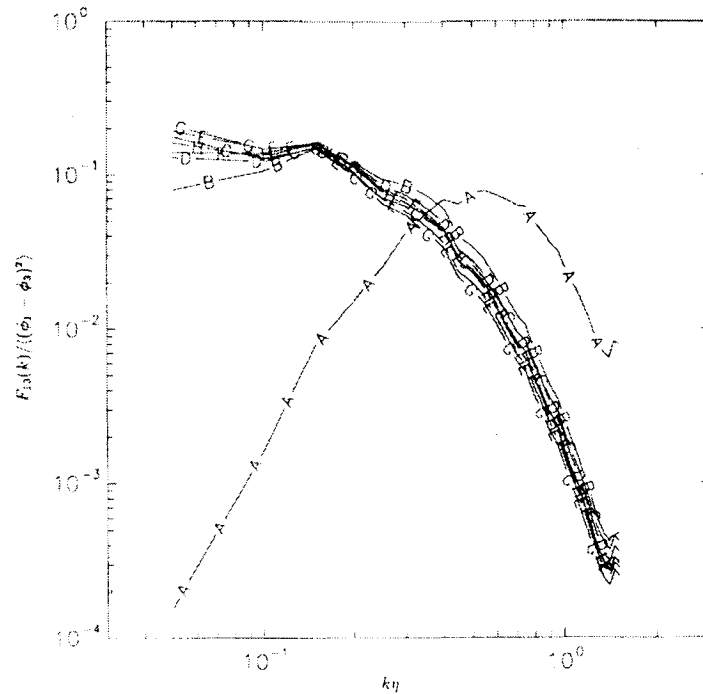
FIG. 7. Spectrum of the difference between the Sc 0.25 and 1.0 scalars (normalized by the variance of the difference), versus Kolmogorov-scaled wave number at different times. In normalized time t^*, the data from lines A to H are for $t^* = 0.0819$–57.33 in increments of 8.19. (Note that at $t^* = 0$ the scalars are identical.)

Figure 7.2: Difference spectra from Yeung and Pope (1993).

Kerstein et al. (1995) calculated difference spectra in their numerical study in which they applied a linear-eddy model to simulate scalar mixing. Their simulations were conducted in a turbulent field that was stationary and homogeneous, with a Reynolds number ranging from 100 to 8000. These tests spanned up to 20 eddy turnover times and were performed with two scalars of Schmidt numbers ranging from 0.01 to 1. A mean scalar gradient was imposed on the flow, as a means of production, to maintain the scalar fluxes. Figure 7.3 shows their calculated difference spectra, from simulations performed at three Reynolds numbers (Re = 5000, 6000, and 8000). Clearly, these spectra are increasing with wavenumber, with an approximate inertial range scaling of $\kappa^{1/2}$, until reaching a peak at the high wavenumber end of the spectrum.
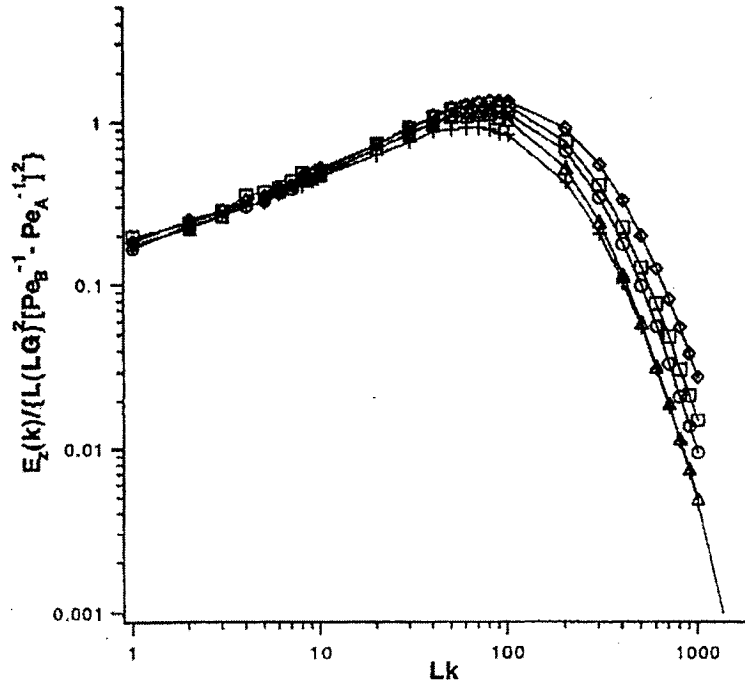
FIG. 2. Scaled spectra $E_z(k)/[L(LG)^2|Pe_A^{-1}-Pe_B^{-1}|^2]$ vs Lk, where $E_z(k)$ is the power spectrum of the scalar difference z obtained from numerical simulations, L is the turbulence integral scale, and G is the imposed scalar gradient. Spectra are shown for cases $(Re, Sc_A, Sc_B) = (5000,1.0,0.1)$ ($\square$), $(5000,0.5,0.1)$ ($\triangle$), $(6000,1.0,0.1)$ ($\lozenge$), $(6000,0.5,0.1)$ ($\bigcirc$), $(8000,0.3,0.06)$ ($+$).

Figure 7.3: Difference spectra calculated in the work of Kerstein *et al.* (1995).

A second DNS in which the difference spectrum has been calculated was performed by Nilsen and Kosály (1997). Their velocity field consisted of decaying homogeneous, isotropic turbulence and the scalar fields were initially identically distributed. The simulations were performed at Taylor-scale Reynolds numbers ranging from 19 to 87 and with scalars of Schmidt numbers 0.5 and 1. An example of Nilsen and Kosály's difference spectrum is depicted in Figure 7.4. It should be noted that in this figure, the scalar is denoted by Z and the difference in the scalars is denoted by α. This difference spectrum has the same form, increasing with wavenumber with an approximate $\kappa^{5/2}$ scaling in the inertial range, as the difference spectrum at early times of Yeung and Pope (1993) (another study conducted in homogeneous, isotropic turbulence). However, since this work was conducted in decaying turbulence, Nilsen and Kosály's (1997) simulations were only able to span up to 3.5 eddy turnover times and they were, therefore, unable to obtain difference spectra for large eddy turnover times. If they had

been able to span a greater period of time, Nilsen and Kosály most likely would have obtained difference spectra, similar to those calculated by Yeung and Pope, at later times. The following quote from Nilsen and Kosály (1997) serves as a basis for comparing their work to that of Yeung and Pope (1993), "Although both our simulations and the investigation by Yeung and Pope (1993) refer to spatially homogeneous cases, ... there are differences in the physical conditions of the two studies. As mentioned earlier, the simulations of Yeung and Pope refer to stationary turbulence, whereas our DNS pertain to decaying turbulence. Furthermore, the initial scalar fields considered in the two studies were different... Note also that in Yeung and Pope mixing is followed for as long as 60 large-eddy turnover times and the shift appears after eight time units. Because our numerical simulations refer to decaying turbulence, there is a limit to how long the flow remains turbulent."
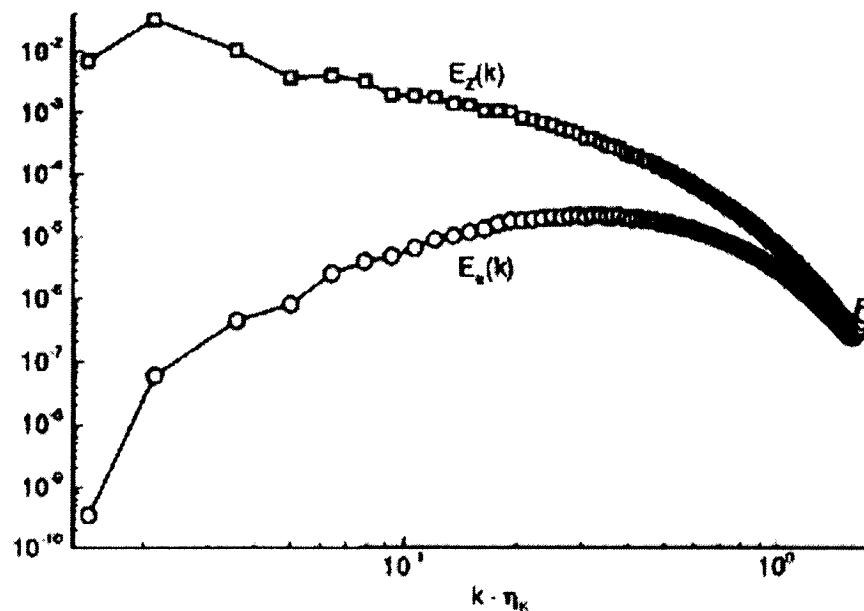
FIG. 6. Plot of $E_a(k)$ and $E_Z(k)$ vs $k \cdot \eta_K$ at $r(u \cdot l)_0 = 1.0$ for the R4 velocity field.

Figure 7.4: Difference, $E_a(k)$, and scalar, $E_Z(k)$, spectra from Nilsen and Kosály (1997).

Yeung (1998) calculated the difference spectrum again when he extended the earlier study of Yeung and Pope (1993). This work was conducted in stationary

130

homogeneous, isotropic turbulence with Taylor-scale Reynolds numbers ranging from 38 to 230 and scalar Schmidt numbers of 0.125 and 1. Similar to Yeung and Pope's (1993) study, Yeung (1998) imposed a large-scale forcing of the velocity field. However, unlike Yeung and Pope, he also imposed a mean scalar gradient and the simulations only spanned 7.5 eddy turnover times. His difference spectra increased with wavenumber, peaking at a high wavenumber near the end of the spectrum, as depicted in Figure 7.5. These spectra scale as approximately $\kappa^{4/3}$ in the inertial range, not as pronounced as the approximate κ^3 scaling in the spectrum at early times of Yeung and Pope (1993).
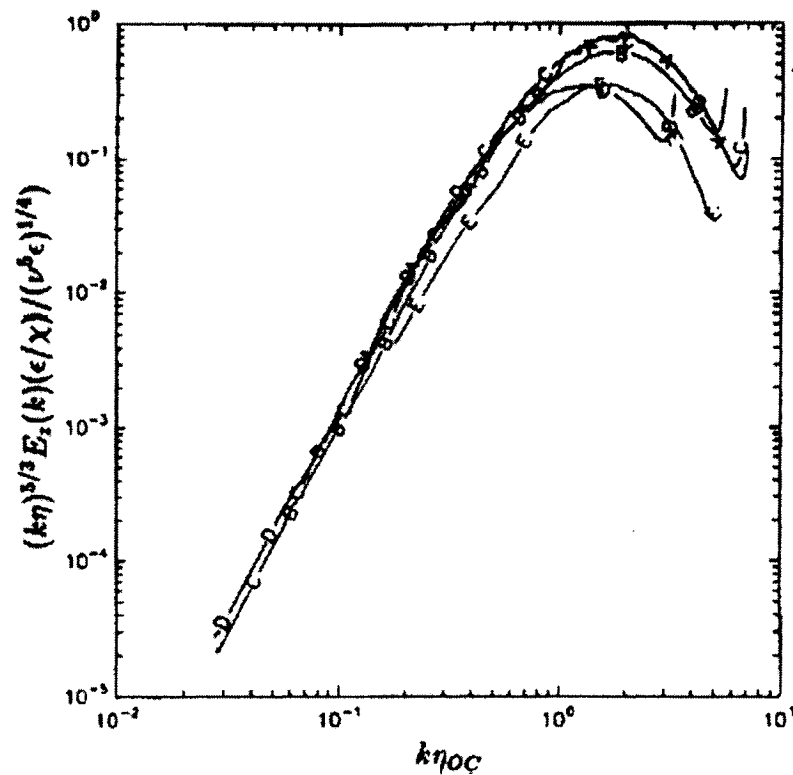
FIG. 3. Difference spectrum in Obukhov–Corrsin scaling based on the parameters (χ, D) of the more diffusive scalar. Labels on the curves are the same as in Fig. 2.

Figure 7.5: Difference spectra from Yeung (1998).

Difference spectra were also calculated by Yeung et al. (2000) in their DNSs studying differential diffusion. Similar to Yeung (1998), these simulations were conducted in stationary homogeneous, isotropic turbulence with a large-scale forcing of the velocity field and an imposed uniform mean scalar gradient. However, since the

Schmidt number range was increased to include values up to 4, the Taylor-scale Reynolds number was only 38. Again, in this instance, the difference spectra were observed to increase with wavenumber, reaching a peak at the high wavenumber end of the spectrum, as seen in Figure 7.6. These difference spectra scaled approximately as κ, similar to the scaling in that of Yeung (1998). Yeung *et al.* also observed a small reverse transfer in the scalar field, which they attributed to the presence of a scalar with a larger Schmidt number, and which could have a significant impact at much higher Schmidt numbers (such as in the present study). This is explained by Yeung *et al.* (2000) as follows: "The main observation is that, especially for high Sc, the transfer is positive at low wave numbers when both p and q are in the highest two octaves. This indicates reverse transfer from the small scales to large scales in the scalar field. This effect appears to be weak and has no appreciable effect on the coherency at low wavenumber in this work. Yet since the magnitude of the reverse transfer increases strongly with Schmidt number the data suggest that this may become important at Sc>>1."
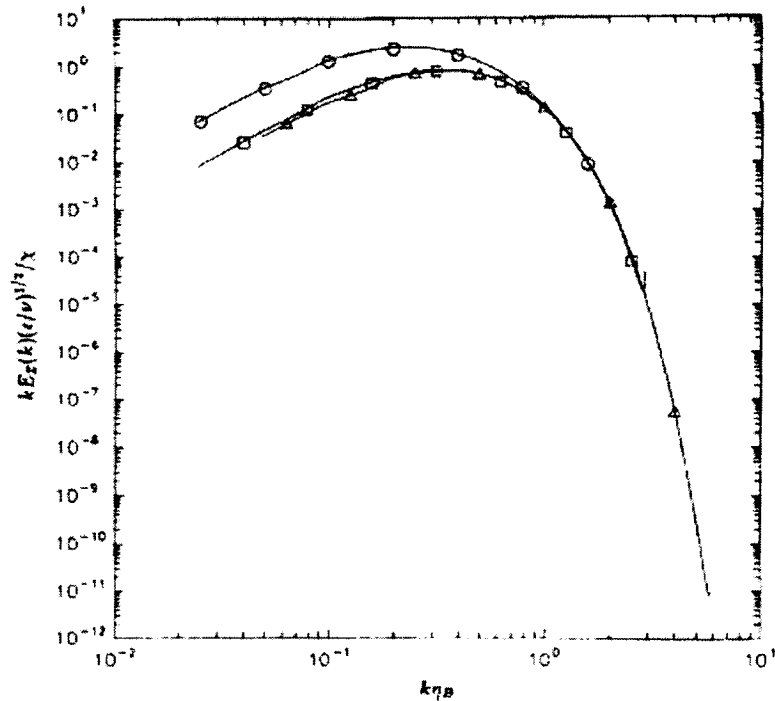
FIG. 3. Scaling of the difference spectrum $E_z(k)$ in Batchelor variables based on parameters of the less diffusive scalar. Symbols are the same as in Fig. 2.

Figure 7.6: Difference spectra from Yeung *et al.* (2000).

Finally, Ulitsky *et al.* (2002) published the most recent numerical study presenting difference spectra. They applied EDQNM theory to simulate the mixing of two scalars in stationary, isotropic turbulence. The results were obtained from simulations spanning up to 30 eddy turnover times. This was another numerical study that had large-scale forcing of the velocity field as well as an imposed mean scalar gradient. In the difference spectra displayed in Figure 7.7, the simulations were performed at four Taylor-scale Reynolds numbers (Re_λ = 131, 162, 231, and 327) and with two sets of Schmidt numbers (Sc = 1/16 and 1, and Sc = 1/4 and 1). Although the presented spectra are compensated, they nevertheless correspond to a spectrum that is increasing with wavenumber, and scale approximately as $\kappa^{1/3}$, until reaching a peak at the high wavenumber end of the spectrum.
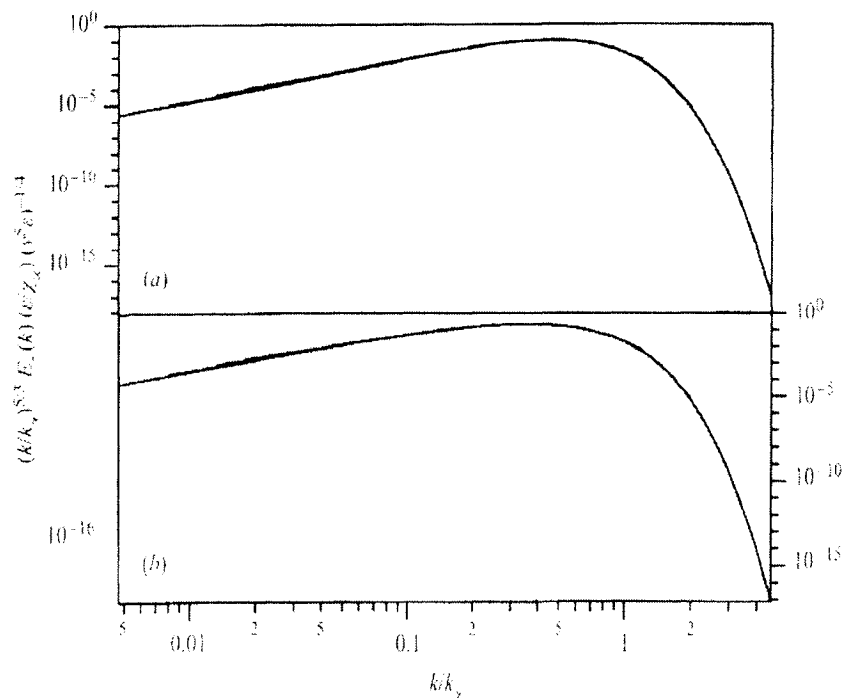
FIGURE 20. Compensated spectrum for $z = \phi_\gamma - \phi_\beta$ plotted against k/k_γ for (a) case (i) and (b) case (ii) at the Reynolds numbers given in the caption of figure 18. Notice that the curves corresponding to the different Reynolds numbers collapse onto a single curve in this coordinate.

Figure 7.7: Difference spectra calculated by Ulitsky *et al.* (2002).

133

Turning to the measured $E_Z(\kappa_1\eta)$ presented in Chapter 6, it is worth remarking that they are, apparently, the only experimental estimates of $E_Z(\kappa_1\eta)$. Therefore, a discussion of their behaviour, and comparison to those from the above studies, is warranted.

The form of $E_Z(\kappa_1\eta)$ measured in the present work is similar in all instances, as was seen in Figures 6.3, 6.8, 6.9, 6.10 and 6.23. This similar form is relatively independent of Reynolds number, radial position, or the ambient conditions into which the jet issued (quiescent or turbulent). In each instance, the spectrum has a peak at the low wavenumber end and then continually decreases with wavenumber. In the low wavenumber range, the shape is similar to that of the continuously decreasing difference spectra, calculated at greater than 8 eddy-turnover times, by Yeung and Pope (1993), and displayed in Figure 7.2. At higher wavenumbers, the spectra are also decreasing, similar to those at later times in the Yeung and Pope (1993) simulations. However, the rate of change (decrease) of the spectra with wavenumber decreases in the high-wavenumber region.

The most likely explanation for the shape of the measured difference spectra in this work relates to the nature of the flow. Specifically, in such a turbulent jet, there is both production and decay of the scalar fluctuations, although the decay dominates. There was production in all the studies that obtained a difference spectrum with a peak in the high wavenumber end of the spectrum (except for Nilsen and Kosály (1997)) as a uniform mean scalar gradient was imposed on the flow. Both Yeung and Pope (1993) and Nilsen and Kosály (1997) performed their simulations without an imposed mean scalar gradient and, thus, their flows had decaying scalar fields. Since Nilsen and Kosály (1997) also had decaying velocity fields, they were only able to extend their simulations for 3.5 eddy turnover times. Thus, as they explained, if they had been able to extend their simulations for a longer time period then they most likely would have obtained a difference spectrum that was decreasing with wavenumber after a peak at the low wavenumber end, similar to the results of Yeung and Pope (1993). Therefore, the form of the measured $E_Z(\kappa_1\eta)$ in the present study appears to be dominated by the decay of the flow.

The differing forms of the numerically calculated difference spectra appear to be rooted in whether or not there is production (provided by imposing a mean scalar gradient on the flow). Yeung (1996) performed a DNS to study the spectral mechanisms of differential diffusion. He did this by comparing results from a flow that was subject to a mean scalar gradient to a flow without a mean scalar gradient. The results of his work support the idea that the presence of an imposed mean scalar gradient, and thus production, can dictate the shape of the difference spectrum. Yeung's results for simulations without a mean scalar gradient indicate that there is a reverse cascade, with incoherency propagating from the small to the large scales. At early times, the scalars were correlated over all scales; however, due to the incoherency propagation, the scalars eventually became decorrelated over all scales. This result provides an explanation for the different form of the difference spectra at various times presented in Yeung and Pope (1993). Furthermore, the results of Yeung's (1996) simulations for flows with a mean scalar gradient showed that the largest scales were well correlated at all times and that the incoherency from the high wavenumber end of the spectrum did not reach the low wavenumber end. This is an indication that the difference spectrum should be increasing from the low wavenumber end with a peak at the high wavenumber end for these flow conditions. Conversely, in a flow without production, the difference spectrum should decrease with wavenumber.

The high scalar Schmidt numbers in this study may also have contributed to the peak in the difference spectra occurring at low wavenumbers. As Yeung *et al.* (2000) observed, incoherency increasingly propagates from the small scales to the large scales as the Schmidt number is increased. They only noticed small incoherency propagation; however, they were only able to employ Schmidt numbers up to 4 and found a strong dependence on Schmidt number. Since the present study was conducted with Schmidt numbers on the order of 10^3, the large scalar Schmidt numbers could have been the driving force of incoherency propagation from the small scales to the large scales. Therefore, this could result in $E_Z(\kappa_1 \eta)$ having a peak at low wavenumbers and then decreasing with wavenumber, as observed.

It should be noted that aliasing of the spectra, as explained by Tennekes and Lumley (1972), is another factor that cannot be overlooked. In this experimental

investigation, all of the spectra are one-dimensional and, therefore, there may be aliasing at lower wavenumbers. This could lead to high spectra in this region, as at a given wavenumber, there may be measured contributions from higher wavenumbers. It would be of benefit to calculate the one-dimensional difference spectrum from a (three-dimensional) DNS to observe any potential differences.

The measured $E_Z(\kappa_1\eta)$ obtained in the present study support the above discussion on the shape of the spectrum being dependent on the nature of the flow. Decay is more dominant in a turbulent jet than production. Therefore, the measured spectra continuously decrease over all wavenumbers in this flow. There have only been two previous numerical studies that calculated difference spectra in a predominantly decaying flow (Yeung and Pope 1993 and Nilsen and Kosály 1997). Yeung and Pope (1993) observed the expected decreasing spectra (at greater than 8 eddy turnover times). Nilsen and Kosály (1997) would probably have obtained similar results had they been able to extend their simulations for a longer period of time. As mentioned, there is some production in a turbulent jet. To this end, there may be contributions to the difference spectra which can be attributed herein to production. This seems to be the case at high wavenumbers, as the measured spectra appear to decrease less rapidly. This is consistent with the high wavenumber end of the numerically calculated difference spectra in flows with production from an imposed mean scalar gradient (i.e., Kerstein 1995, Yeung 1998, Yeung *et al.* 2000 and Ulitsky *et al.* 2002). Thus, the measured $E_Z(\kappa_1\eta)$ obtained herein are dominated by the decay of the flow with potential smaller contributions at high wavenumbers due to production.

Chapter 8

Conclusions

8.1 Thesis Review

This thesis served to investigate and quantify differential diffusion of passive scalars in a turbulent jet over a range of Reynolds numbers. This was accomplished by studying a turbulent water jet issuing into either a quiescent or turbulent background. This section will summarize each chapter and highlight some of the pertinent results.

- Chapter 1 served to introduce the topic of differential diffusion and present the objectives of this study along with the organization of this thesis. Differential diffusion was defined and the motivating factors leading to its study were discussed. Next, the objectives of this thesis were outlined. These included two main objectives, which were to systematically study the Reynolds number dependence of differential diffusion while simultaneously determining its radial distribution in a cross-section of an axisymmetric jet. The secondary objectives included determining differential diffusion effects in a flow containing scalars with large Schmidt numbers, determining the scales at which differential diffusion is present, and how background turbulence affects differential diffusion. The final section of this chapter served to outline the remainder of this thesis.

137

- A comprehensive literature review was presented in the second chapter. This began with a review of turbulent jets. The governing equations for axisymmetric turbulent jets were presented, followed by an overview of the scaling properties of the jet width, mean axial velocity, mean axial scalar concentration, r.m.s. axial velocity fluctuations, and r.m.s. axial scalar fluctuations. The development of axisymmetric turbulent jets with different initial conditions was then discussed. The turbulent jet section concluded with a discussion on the effects of background turbulence on the evolution of a turbulent jet. This was followed by a review of the measurement technique, LIF. The applicability of LIF was discussed along with some of the physical phenomena (such as photobleaching) that must be accounted for when employing LIF to measure scalar concentrations. The final section of this chapter reviewed earlier studies of differential diffusion, broken into two subsections. The first examined the numerical simulations, which included DNSs and modeling studies. This was followed by a discussion of experimental work, including gas-phase studies, in reacting and non-reacting flows, and liquid-phase studies.

- Chapter 3 provided some theoretical considerations. Firstly, a normalized concentration difference equation (to quantify differential diffusion effects) was developed. This equation was derived from the advection-diffusion equation that governs non-reacting passive scalars. The normalized concentration difference, Z, was also defined. The next section provided a description of fluorescence theory. This included an overview of the phenomenon of fluorescence along with equations to quantify the fluorescence emission of scalars. In particular, a linear relationship relating emitted fluorescence intensity to scalar concentration, for dilute scalar concentrations, was presented.

- The fourth chapter detailed the experimental apparatus, outlined how the detected signals were related to species concentration, and described some steps undertaken to verify the negligibility of several potential sources of error. The experimental setup was divided into subsections. The first discussed the ambient conditions and overviewed the random jet array used to create the background turbulence. Next, the jet apparatus was presented, which included a detailed

138

description of the equipment used in controlling the jet. This was followed by a review of the optical components used to focus both the laser beam and the emitted fluorescence signal onto the photodetectors (two PMTs). This subsection concluded with an overview of the data acquisition equipment and the techniques employed in processing the signal. The next section of this chapter reviewed the relation between fluorescent signals and species concentrations. This included subsections on the calibration procedure and the application of an optimal Wiener filter. Finally, sources of error, including photobleaching and thermal blooming, laser attenuation, trapping, buoyancy and inertial effects as well as PMT drift were examined.

- The experimental conditions and validation of the flow were presented in Chapter 5. The first section overviewed the theoretical and empirical formulae applied to determine the mean jet centreline axial velocity and length, time, and velocity scales at the measurement location. Next, the calculated length and time scales in the jet were presented for all the Reynolds numbers studied. These were followed by the presentation of the measured velocity statistics in the approximately homogeneous, isotropic turbulent background with zero-mean flow. Next, the independence of the individual species concentration measurements was verified. This included a comparison of scalar spectra and PDFs from single and two-dye experiments. In the final section, individual mean and r.m.s. scalar concentration profiles were compared to those obtained in previous studies.

- Results elucidating differential diffusion in a turbulent jet of high Schmidt number scalars were presented in Chapter 6. The results from the experiments conducted with the turbulent jet issuing into a quiescent background were presented first. Statistics of Z indicated that differential diffusion decreases with increasing Reynolds number ($Z_{rms} \propto Re^{-0.09}$), although differential diffusion effects were still present at the highest Reynolds number studied, as $Z_{rms} = 0.064$ at Re = 10600. Measurements at different radial positions also showed that differential diffusion effects increased away from the centreline. This was evident as Z_{rms} increased with increasing radial position. Spectra of Z, which

139

were used for the calculation of Z_{rms}, were also presented. Furthermore, they also proved that differential diffusion effects were present at scales greater than the Kolmogorov scale at all Reynolds numbers and radial locations studied. PDFs of Z illustrated a change in shape, as they showed an increase in both S_Z and K_Z, as the Reynolds number decreased or with increasing radial position from the centreline. Conditional expectations provided evidence to support the hypothesis (and discussion in section 7.1) that differential diffusion effects are directly dependent on the entrainment of ambient fluid. An increase of differential diffusion effects was also observed in the presence of background turbulence by comparing the values of Z_{rms} to those obtained in the quiescent background. Z_{rms} increased at each radial position in the turbulent background, indicating differential diffusion had also increased. Again, differential diffusion effects were present at scales greater than the Kolmogorov scale. PDFs of Z also illustrated an increase in S_Z and K_Z in the turbulent background. Finally, conditional expectations in the turbulent background indicated that the flow at the centreline in the turbulent background was similar to that at the jet edges in the quiescent background.

- Chapter 7 served as a discussion of i) the influence of the entrainment of ambient fluid on differential diffusion and, ii) the form of $E_Z(\kappa_1\eta)$. The results from the previous chapter strongly supported the hypothesis, first proposed by Kerstein (1990), that differential diffusion increases at interfaces of parcels of jet fluid (containing concentrations of both fluorescent dyes) and parcels of ambient fluid (containing concentrations of neither dye). At these interfaces, the more diffusive scalar will diffuse more rapidly into the ambient fluid. This will result in a large positive Z in the parcel of ambient fluid, and thus an increase in differential diffusion effects with decreasing Reynolds number, increased radial position from the centreline, or in the presence of background turbulence. As this was the first work to measure $E_Z(\kappa_1\eta)$, its form was discussed and compared to previous numerical estimates of the difference spectrum. The form of the difference spectrum is still an open subject. In a flow with turbulent production, such as an imposed mean scalar gradient, the difference spectrum peaks at high

wavenumbers (e.g. Kerstein *et al.* 1995, Yeung 1998, Yeung *et al.* 2000, and Ulitsky *et al.* 2002). However, in a decaying flow, the spectrum appears to peak at low wavenumbers (e.g. Yeung and Pope 1993). The turbulent jet flow herein exhibited both decay and production, albeit with the former dominating. Hence, the measured $E_Z(\kappa_1\eta)$ is consistent with that of a decaying flow (i.e., decreasing over all wavenumbers), although the decreasing slope at high wavenumbers may be attributable to the presence of turbulent production.

8.2 Contributions of the Present Study

This thesis provides the first systematic study of the Reynolds number dependence of differential diffusion. Determining Z_{rms} by integrating $E_Z(\kappa_1\eta)$ up to the Kolmogorov scale provided a consistent and rational method to compare these values at different Reynolds numbers. With this procedure, Z_{rms} was found to scale as $Z_{rms} \propto Re^{-0.09}$. Previous experimental studies, mainly in gas-phase flows, were unable to determine a scaling law for Z_{rms} as the majority have been conducted at only one or two Reynolds numbers (i.e., Long *et al.* 1993 and Bergmann *et al.* 1998).

To date, the only differential diffusion study conducted with scalars having Schmidt numbers of the order 10^3 was performed at a low Reynolds number. Saylor and Sreenivasan (1998) conducted their work with fluorescent dyes mixed in water, resulting in Schmidt numbers ranging from 1200 to 77000. However, these experiments were only conducted at a Reynolds number of 430. Other experimental studies have been conducted at higher Reynolds numbers in gas-phase flows, which typically have Schmidt numbers of order 1. The highest Schmidt number attained in a numerical study was 4 (Yeung *et al.* 2000). Thus, the present work provides the first measurements of differential diffusion at both moderate Reynolds numbers and high Schmidt numbers. The present results can be compared with other studies, conducted at lower Schmidt numbers, to determine the effects of Schmidt number on differential diffusion.

Heretofore, difference spectra had only been estimated by means of numerical simulations. This is the first experimental measurement of this quantity. It enables an improved estimate of the scales at which differential diffusion is present. Previous experimental studies have only been able to make a qualitative assessment of the scales

at which differential diffusion occurred (such as Saylor and Sreenivasan (1998) observing instances of Z remaining non-zero for times greater than the Kolmogorov timescale). This study was able to use $E_Z(\kappa_1\eta)$ to quantify contributions to Z_{rms} at scales greater than the Kolmogorov scale.

Furthermore, practical flows typically do not enter into a stagnant field, but rather into a flow that is often turbulent. Hence, experiments were conducted to measure differential diffusion in a turbulent jet issuing into a turbulent background. These were the first such experiments and were able to show that the presence of background turbulence serves to increase differential diffusion.

Each observed instance of increasing differential diffusion effects provides the strongest evidence to date to support the hypothesis that differential diffusion increases with the number of interfaces between the jet fluid and ambient fluids. This hypothesis was first put forth by Kerstein (1990) and later by Smith *et al.* (1995a). In these studies, an increase in differential diffusion due to this effect was observed in only one instance, i.e., as the radial position was increased. This phenomenon was also observed in this work. However, an increase in differential diffusion effects due to an increase in the occurrence of interfaces between jet and ambient fluid was also observed i) as the Reynolds number decreased and, ii) in the presence of background turbulence. Hence, two new instances of increased differential diffusion at interfaces between jet and ambient fluid were observed.

8.3 Recommendations for Future Work

- The main focus of this work was to systematically study the Reynolds number dependence of differential diffusion while simultaneously determining the effect of radial position. In accomplishing this, only two scalar Schmidt numbers were considered. It is evident from the normalized concentration difference equation developed in section 3.1 that differential diffusion is dependent on both the Reynolds number of the flow and the Schmidt numbers of the scalars. Therefore, studying different Schmidt numbers will serve to further this work. In particular, it would seem logical to determine any scaling of differential diffusion effects with Schmidt number.

142

- This work could also be further advanced by performing experiments at different downstream positions. All measurements presented in this thesis were obtained at a single downstream location in the self-similar region of the jet, x/d = 50. A systematic study of the downstream variation, from near the jet exit in the near-field region and extending to positions far downstream in the self-similar region, of differential diffusion could lead to further insight. Downstream variation of differential diffusion has been studied numerically (i.e., Bilger and Dibble 1982 and Kerstein 1990) and experimentally in gas-phase flows (i.e., Smith *et al.* 1995a). However, to date, there has not been a study examining this effect in liquid-phase flows, with Schmidt numbers of order 10^3.

- It would also be beneficial to further the background turbulence measurements. Only one case of background turbulence was studied. Varying the intensity of the background turbulence may also help to further understand the effects of background turbulence on differential diffusion.

- Finally, the author recommends performing these experiments with improved spatial resolution. At each Reynolds number studied, the resolution was between the Kolmogorov and Batchelor scales. Though this clearly showed that differential diffusion was present at scales greater than the Kolmogorov scale (even at the highest Reynolds number studied), there were certainly contributions to $E_Z(\kappa_I\eta)$ at scales that were not resolved. Therefore, a more definitive determination of this spectrum could be obtained by resolving all scales, from the integral scale down to the smallest dissipative scale of the scalars. This being said, achieving high spatial resolution at high Reynolds numbers would most likely necessitate an especially large experimental facility.

In conclusion, the intent of the present work was to build on previous studies of differential diffusion and further our understanding of the subject. There nevertheless remains additional work to be performed to enable a fuller comprehension of differential diffusion. The results of this work will hopefully provide motivation for such further investigations.

References

Aguirre, R.C. and Catrakis, H.J.   2005   Scalar-threshold dependence and internal dynamics in turbulent jets. *Phys. Fluids* **17**, Art. No. 038103.

Anfossi, D., Ferrero, E., Brusasca, G., Marzorati, A. and Tinarelli, G.   1993   A simple way of computing buoyant plume rise in Lagrangian stochastic dispersion models. *Atmos. Environ.* **27A**, 1443-1451.

Batchelor, G.K., 1953   The *Theory of Homogeneous Turbulence*, Cambridge University Press.

Batchelor, G.K.   1959   Small-scale variation of convected quantities like temperature in turbulent fluid. Part 1.   General discussion and the case of small conductivity.   *J. Fluid Mech.* **5**, 113-133.

Becker, H.A., Hottel, H.C. and Williams, G.C.   1967   The nozzle-fluid concentration field of the round, turbulent, free jet.   *J. Fluid Mech.* **30**, 285-303.

Benson, D.M., Bryan, J., Plant, A.L., Gotto, A.M. and Smith, L.C.   1985   Digital Imaging Fluorescence Microscopy : Spatial Heterogeneity of Photobleaching Rate Constants in Individual Cells.   *J. Cell Biol.* **100**, 1309-1323.

Bergmann, V., Meier, W., Wolff, D. and Stricker, W.   1998   Application of spontaneous Raman and Rayleigh scattering and 2D LIF for the characterization of a turbulent $CH_4/H_2/N_2$ jet diffusion flame.   *Appl. Phys. B* **66**, 489-502.

144

Bilger, R.W. 1977 Reaction Rates in Diffusion Flames. *Comb. and Flame* **30**, 277-284.

Bilger, R.W. 1981 Molecular Transport Effects in Turbulence Diffusion Flames at Moderate Reynolds Number. *AIAA J.* **20**, 962-970.

Bilger, R.W. and Dibble, R.W. 1982 Differential Molecular Diffusion Effects in Turbulent Mixing. *Combust. Sci. Tech.* **28**, 161-172.

Birch, A.D., Brown, D.R., Dodson, M.G. and Thomas, J.R. 1978 The turbulent concentration field of a methane jet. *J. Fluid Mech.* **88**, 431-449.

Boersma, B.J., Brethouwer, G. and Nieuwstadt, F.T.M. 1998 A numerical investigation on the effect of the inflow conditions on the self-similar region of a round jet. *Phys. Fluids* **10**, 899-909.

Breidenthal, R. 1981 Structure in turbulent mixing layers and wakes using a chemical reaction. *J. Fluid Mech.* **109**, 1-24.

Brownell, C.J. and Su, L.K. 2004 Planar measurement of differential diffusion in turbulent jets. *AIAA Paper 2004-2335*, 34th AIAA Fluid Dynamics Conference.

Buch, K.A. 1991 Fine scale structure of conserved scalar mixing in turbulent shear flows: Sc >> 1 and Sc $\approx$ 1. Ph.D. Thesis. California Institute of Technology.

Camussi, R., Guj, G. and Stell A. 2002 Experimental study of a jet in a crossflow at very low Reynods number. *J. Fluid Mech.* **454**, 113-144.

Cetegen, B.M. and Mohamad, N. 1993 Experiments on liquid mixing and reaction in a vortex. *J. Fluid Mech.* **249**, 391-414.

Chen, C.J. and Rodi, W. 1980 *Vertical Turbulent Buoyant Jets: A Review of the Experimental Data.* Pergamon Press.

Chen, J.Y. and Chang, W.C. 1998 Modeling Differential Diffusion Effects in Turbulent Nonreacting/Reacting Jets with Stochastic Mixing Models. *Combust. Sci. Tech.* **133**, 343-375.

Ching, C.Y., Fernando, H.J.S. and Robles, A. 1995 Breakdown of line plumes in turbulent environments. *J. of Geophysical Research* **100**, 4707-4713.

Coppeta, J. and Rogers, C. 1998 Dual emission laser induced fluorescence for direct planar scalar behaviour measurements. *Exp. Fluids* **25**, 1-15.

Crimaldi, J.P. 1997 The effect of photobleaching and velocity fluctuations on single-point LIF measurements. *Exp. Fluids* **23**, 325-330.

Crimaldi, J.P. and Koseff, J.R. 2001 High-resolution measurements of the spatial and temporal scalar structure. *Exp. Fluids* **31**, 90-102.

Deusch, S., Merava, H., Dracos, T. and Rys, P. 2000 Measurement of velocity and velocity derivatives based on pattern tracking in 3D LIF images. *Exp. Fluids* **29**, 388-401.

Deusch, S. and Dracos, T. 2001 Time resolved 3D passive scalar concentration-field imaging by laser induced fluorescence (LIF) in moving liquids. *Meas. Sci. Technol.* **12**, 188-200.

Dewey, C.F. 1976 Qualitative and quantitative flow field visualization utilizing laser-induced fluorescence. *AGARD Conf. Proc.* 193.

Dibble, R.W. and Long, M.B. 2005 Investigation of differential diffusion in turbulent jet flows using planar laser Rayleigh scattering. *Comb. and Flame* **143**, 644-649.

Dimotakis, P.E., Miake-Lye, R.C. and Papantoniou, D.A. 1983 Structure and dynamics of round turbulent jets. *Phys. Fluids* **26**, 3185-3192.

Dimotakis, P.E. 2000 The mixing transition in turbulent flows. *J. Fluid Mech.* **409**, 69-98.

Dowling, D.R. 1988 Mixing in gas phase turbulent jets. Ph.D. Thesis, California Institute of Technology.

Dowling, D.R., Lang, D.B. and Dimotakis, P.E. 1989 An improved laser-Rayleigh scattering photodection system. *Exp. Fluids* **7**, 435-440.

Dowling, D.R. and Dimotakis, P.E. 1990 Similarity of the concentration field of gas-phase turbulent jets. *J. Fluid Mech.* **218**, 109-141.

Dowling, D.R. 1991 The estimated scalar dissipation rate in gas-phase turbulent jets. *Phys. Fluids A* **3**, 2229-2246

Drake, M.C., Pitz, R.W. and Lapp, M. 1986 Laser Measurements on Nonpremixed H2-Air Flames for Assessment of Turbulent Combustion Models. *AIAA Journal* **24** No. 6, 905-917.

Dyer, M.J. and Crosley, D.R. 1982 Two-dimensional imaging of OH laser-induced fluorescence in a flame. *Optics Letters* **7**, 382-384.

Ferdman, E., Ötügen, M.V. and Kim, S. 2000 Effect of Initial Velocity Profile on the Development of Round Jets. *J. Propulsion Power* **16**, 676-686.

147

Fernando, H.J.S. and De Silva, I.P.D. 1993a Oscillating grids as a source of nearly isotropic turbulence. *Phys. Fluids A* **6**, 2455-2464.

Fernando, H.J.S. and De Silva, I.P.D. 1993b Note on secondary flows in oscillating-grid, mixing-box experiments. *Phys. Fluids A* **5**, 1849-1851.

Fischer, H.B., List, E.J., Koh, R.C.Y., Imberger, J. and Brooks, N.H. 1979 *Mixing in inland and coastal waters*, Academic Press.

Fox, R.O. 1999 The Lagrangian spectral relaxation model for differential diffusion in homogeneous turbulence. *Phys. Fluids* **11** No. 6, 1550-1571.

Friehe, C.A., Van Atta, C.W. and Gibson, C.H. 1971 Jet turbulence: dissipation rate measurements and correlations. *AGARD Turbulent Shear Flows*, **CP-93**, 18-1 to 18-7.

Gargett, A.E., Merryfield, W.J. and Holloway, G. 2003 Direct numerical simulation of differential scalar diffusion in three-dimensional stratified turbulence. *J. Phys. Oceanogr.* **33**, 1758-1782.

Gaskin, S.J., McKernan, M. and Xue, F. 2004 The effect of background turbulence on jet entrainment: an experimental study of a plane jet in a shallow coflow. *J. of Hydraulic Research* **42**, 531-540.

Gordon, M., Cater, J.E. and Soria, J. 2004 Investigation of the mean passive scalar field in zero-net-mass-flux jets in cross-flow using planar-laser-induced fluorescence. *Phys. Fluids* **16**, 794-808.

Guilbault, G.G. 1973 *Practical fluorescence: Theory, methods, and techniques*, Marcel Dekker, INC.

Guillard, F., Fritzon, R., Revstedt, J., Trägårdh, C., Aldén, M. and Fuchs, L. 1998 Mixing in a confined turbulent impinging jet using planar laser-induced fluorescence. *Exp. Fluids* **25**, 143-150.

Guo, Y., Davies, P.A., Fernando, H.J.S. and Ching, C.Y. 1999 Influence of background turbulence on the evolution of turbulent jets. *Conference proceedings of the 28th IAHR congress.*

Hamamatsu Photonics 2006 *Photomultiplier Tubes*, Online Catalog.

Hinze, J.O. 1975 *Turbulence*, McGraw-Hill.

Hopfinger, E.J. and Toly, J.A. 1976 Spatially decaying turbulence and its relation to mixing across density interfaces. *J. Fluid Mech.* **78**, 155-175.

Houcine, I., Vivier, H., Plasari, E., David, R. and Villermaux, J. 1996 Planar laser induced fluorescence technique for measurements of concentration fields in continuous stirred tank reactors. *Exp. Fluids* **22**, 95-102.

Hunt, J.C.R. 1994 Atmospheric Jets and Plumes. *NATO ASI Series E* **255**, 309-344.

Hussein, H.J., Capp, S.P. and George, W.K. 1994 Velocity measurements in a high-Reynolds-number, momentum-conserving, axisymmetric, turbulent jet. *J. Fluid Mech.* **258**, 31-75.

Jackson, P.R. and Rehmann, C.R. 2003 Laboratory Measurements of Differential Diffusion in a Diffusively Stable, Turbulent Flow. *J. Phys. Oceanogr.* **33**, 1592-1603.

Jackson, P.R., Rehmann, C.R., Sáenz, J.A. and Hanazaki, H. 2005 Rapid distortion theory for differential diffusion. *Geophys. Res. Lett.* **32**.

Jenkins, F.A. and White, H.E. 1957 *Fundamentals of Optics*, McGraw Hill.

Kerstein, A.R., Dibble, R.W., Long, M.B., Yip, B. and Lyons, K. 1989 Measurement and computation of differential molecular diffusion in a turbulent jet. In *Proc. 7th Symp. on Turb.Shear Flows*, paper 14-2.

Kerstein, A.R. 1990 Linear-eddy modelling of turbulent transport. Part 3. Mixing and differential molecular diffusion in round jets. *J. Fluid Mech.* **216**, 411-435.

Kerstein, A.R., Cremer, M.A. and McMurtry, P.A. 1995 Scaling properties of differential molecular diffusion effects in turbulence. *Phys. Fluids* **7** No. 8, 1999-2007.

Kolmogorov, A. N., 1941 *Dokl. Akad. Nauk SSSR*, **30**, p. 301. Kolmogorov, A. N., 1941 *Dokl. Akad. Nauk SSSR*, **32**, p. 16.

Koochesfahani, M. 1984 Experiments on turbulent mixing and chemical reactions in a liquid mixing layer. PhD Thesis, California Institute of Technology.

Koochesfahani, M.M. and Dimotakis, P.E. 1985 Laser-Induced Fluorescence Measurements of Mixed Fluid Concentration in a Liquid Plane Shear Layer. *AIAA J.* **23**, No. 11, 1700-1707.

Kronenburg, A. and Bilger, R.W. 1997 Modelling of differential diffusion effects in nonpremixed nonreacting turbulent flow. *Phys. Fluids* **9** No. 5, 1435-1447.

Kronenburg, A. and Bilger, R.W. 2001b Modelling Differential Diffusion in Nonpremixed Reacting Turbulent Flow: Application to Turbulent Jet Flames. *Combust. Sci. Tech.* **166**, 175-194.

Kronenburg, A. and Bilger R.W. 2001a Modelling Differential Diffusion in Nonpremixed Reacting Turbulent Flow: Model Development. *Comb. Sci. Tech.* **166**, 198-227.

Kychakoff, G., Howe, R.D., Hanson, R.D. and McDaniel, J.C. 1982 Quantitative visualization of combustion species in a plane. *Applied Optics* **21**, 3225-3227.

Landau, L.D. and Lifshitz, E.M. 1959 *Fluid Mechanics*, Pergamon Press.

Lockwood, F.C. and Moneib, H.A. 1980 Fluctuating temperature measurements in a heated round free jet. *Combust. Sci. Tech.* **22**, 63-81.

Long, M.B., Starner, S.H. and Bilger, R.W. 1993 Differential Diffusion in Jets using Joint PLIF and Lorenz-Mie Imaging. *Comb. Sci. Tech.* **92**, 209-224.

Masri, A.R., Dibble, R.W. and Barlow, R.S. 1992 Chemical Kinetic Effects in Nonpremixed Flames of H_2/CO_2 Fuel. *Comb. and Flame* **91**, 285-309.

Meier, W., Prucker, S., Cao, M.H. and Stricker, W. 1996 Characterization of Turbulent H2/N2/Air Jet Diffusion Flames by Singel-Pulse Spontaneous Raman Scattering. *Comb. Sci. Tech.* **118**, 293-312.

Miller, P.L. 1991 Mixing in high Schmidt number turbulent jets. PhD Thesis, California Institute of Technology.

Miller, P.L. and Dimotakis, P.E. 1991 Reynolds number dependence of scalar fluctuations in a high Schmidt number turbulent jet. *Phys. Fluids A* **3**, 1156-1163.

Mohamed, M.S. and Larue, J.C. 1990 The decay power law in grid-generated turbulence. *J. Fluid Mech.* **219**, 195-214.

Monin, A.S. and Yaglom, A.M.   1971   *Statistical Fluid Mechanics, Mechanics of Turbulence*, vol. 1, MIT Press.

Nilsen, V. and Kosály, G.   1997   Differentially diffusing scalars in turbulence.   *Phys. Fluids* **9**, 3386-3397.

Nilsen, V. and Kosály, G.   1999   Differential Diffusion in Turbulent Reacting Flows. *Comb. and Flame* **117**, 493-513.

Owen, F.K.   1976   Simultaneous laser measurements of instantaneous velocity and concentration in turbulent mixing. *AGARD Conf. Proc.* 193.

Panchapakesan, N.R. and Lumley, J.L.   1993a   Turbulence measurements in axisymmetric jets of air and helium. Part 1. Air jet. *J. Fluid Mech.* **246**, 197-223.

Panchapakesan, N. R. and Lumley, J.L.   1993b   Turbulence measurements in axisymmetric jets of air and helium. Part 2. Helium jet. *J. Fluid Mech.* **246**, 225-247.

Papanicolaou, P.N. and List, E.J.   1987   Statistical and spectral properties of tracer concentration in round buoyant jets. *J. Heat Mass Transfer* **30**, 2059-2071.

Papanicolaou, P.N. and List, E.J.   1988   Investigations of round vertical turbulent buoyant jets. *J. Fluid Mech.* **195**, 341-391.

Pitsch, H. and Peters, N.   1998   A Consistent Flamelet Formulation for Non-Premixed Combustion Considering Differential Diffusion Effects. *Comb. and Flame* **114**, 26-40.

Pitsch, H.   2000   Unsteady Flamelet Modeling of Differential Diffusion in Turbulent Jet Diffusion Flames. *Comb. and Flame* **123**, 358-374.

Pope, S.B., 2000 *Turbulent Flow*, Cambridge Univ. Press.

Press, W.H., Teukolsky, S.A., Vetterling, W.T. and Flannery, B.P. 1992 *Numerical Recipes in Fortran 77 Second Edition*, Cambridge Univ. Press.

Rajaratnam, N. 1976 *Turbulent Jets*, Elsevier Scientific Pub. Co.

Ready, J.F. 1978 *Industrial Applications of Lasers*, Academic Press.

Rodi, W. 1975 A new method of analyzing hot-wire signals in highly turbulent flow and its evaluation in a round jet. *DISA Information* **17**.

Rodi, W. 1982 *Turbulent buoyant jets and plumes*, Pergamon Press.

Rossi, B. 1957 *Optics*, Addison-Wesley.

Sahar, E. and Treves, D. 1977 Bleaching and Diffusion of Laser Dyes in Solution Under High Power UV Irradiation. *Optics Communications* **21**, 20-24.

Saylor, J.R. 1993 Differential diffusion in turbulent and oscillatory, non-turbulent, water flows. PhD thesis, Yale University.

Saylor, J.R. 1995 Photobleaching of disodium fluorescein in water. *Exp. Fluids* **18**, 445-447.

Saylor, J.R. and Sreenivasan, K.R. 1998 Differential diffusion in low Reynolds number water jets. *Phys. Fluids* **10** No. 5, 1135-1146.

Shan, J.W., Long, D.B. and Dimotakis, P.E. 2004 Scalar concentration measurements in liquid-phase flows. *Exp. Fluids* **36**, 268-273.

Smith, L.L., Dibble, R.W., Talbot, L., Barlow, R.S. and Carter, C.D. 1995a Laser Raman scattering measurements of differential molecular diffusion in nonreacting turbulent jets of H_2/CO_2 mixing with air. *Phys. Fluids* **7** No. 6, 1455-1466.

Smith, L.L., Dibble, R.W., Talbot, L., Barlow, R.S. and Carter, C.D. 1995b Laser Raman Scattering Measurements of Differential Molecular Diffusion in Turbulent Nonpremixed Jet Flames of H_2/CO_2 Fuel. *Comb. and Flame* **100**, 153-160.

Su, L.K. and Clemens, N.T. 2003 The structure of fine-scale scalar mixing in gas-phase planar turbulent jets. *J. Fluid Mech.* **488**, 1-29.

Tennekes, H. and Lumley, J.L., 1972 *A First Course in Turbulence*, MIT Press.

Thompson, S. and Turner, J. 1975 Mixing across an interface due to turbulence generated by an oscillating grid. *J. Fluid Mech.* **67**, 349-368.

Tian, X.D. and Roberts J.W. 2003 A 3D LIF system for turbulent buoyant jet flows. *Exp. Fluids* **35**, 636-647.

Townsend, A.A. 1976 *The Structure of Turbulent Shear Flows*, 2nd edn. Cambridge University Press.

Tsuji, H. and Yamaoka, I. 1971 Structure analysis of counterflow diffusion flames in the forward stagnation region of a porous cylinder. *Thirteenth Symp. (Intl.) on Combustion*, 723.

Ulitsky, M., Vaithianathan, T. and Collins, L.R. 2002 A spectral study of differential diffusion of passive scalars in isotropic turbulence. *J. Fluid Mech.* **460**, 1-38.

Van Vliet, E., Van Bergen, S.M., Derksen, J.J., Portela, L.M. and Van den Akker, H.E.A. 2004 Time-resolved, 3D, laser-induced fluorescence measurements of fine-structure passive scalar mixing in a tubular reactor. *Exp. Fluids* **37**, 1-21.

Variano, E.A., Bodenschatz, E. and Cowen, E.A. 2004 A random synthetic jet array driven turbulence tank. *Exp. Fluids* **37**, 613-615.

Villermaux, E., Innocenti, C. and Duplat, J. 2001 Short circuits in the Corrsin-Obukhov cascade. *Phys. Fluids* **13**, 284-289.

Walker, D.A. 1987 A fluorescence technique for measurement of concentration in mixing liquids. *J. Phys. E: Sci. Instrum.* **20**, 217-224.

Wang, G.R. and Fiedler, H.E. 2000a On high spatial resolution scalar measurement with LIF. Part 1: Photobleaching and thermal blooming. *Exp. Fluids* **29**, 257-264.

Wang, G.R. and Fiedler, H.E. 2000b On high spatial resolution scalar measurement with LIF. Part 2: The noise characteristic. *Exp. Fluids* **29**, 265-274.

Ware, B.R., Cyr, D., Gorti, S. and Lanni, F. 1983 Electrophoretic and Frictional Properties of Particles in Complex Media Measured by Laser Light Scattering and Fluorescence Photobleaching Recovery. In *Measurement of Suspended Particles by Quasi-Elastic Light Scattering*, 255-289.

White, F.M. 2006 *Viscous Fluid Flow*, McGraw Hill.

Wiener, N. 1949 *Extrapolation, Interpolation, and Smoothing of Stationary Time Series*. Technology Press.

Wilson, R.A.M. and Danckwerts, P.V. 1964 Studies in turbulent mixing-II A hot-air jet. *Chem. Eng. Sci.* **19**, 885-895.

Wright, S.J. 1994 The Effect of Ambient Turbulence on Jet Mixing. *NATO ASI Series E* **255**, 13-27.

Wygnanski, I. and Fiedler, H. 1969 Some measurements in the self-preserving jet. *J. Fluid Mech.* **38**, 577-612.

Xu, G. and Antonia, R.A. 2002 Effect of different initial conditions on a turbulent round free jet. *Exp. Fluids* **33**, 677-683.

Yeung, P.K. and Pope, S.B. 1993 Differential diffusion of passive scalars in isotropic turbulence *Phys. Fluids A* **5**, 2467-2478.

Yeung, P.K. 1996 Multi-scalar triadic interactions in differential diffusion with and without mean scalar gradients. *J. Fluid Mech.* **321**, 235-278.

Yeung, P.K. 1998 Correlations and conditional statistics in differential diffusion: Scalars with uniform mean gradients. *Phys. Fluids* **10** No. 10, 2621-2635.

Yeung, P.K., Sykes, M.C. and Vedula, P. 2000 Direct numerical simulation of differential diffusion with Schmidt numbers up to 4.0. *Phys. Fluids* **12** No. 6, 1601-1604.